Optical Materials: X 13 (2022) 100108

Contents lists available at ScienceDirect

Optical Materials: X

journal homepage: www.elsevier.com/locate/omx

Invited review article

XPS/ESCA on glass surfaces: A useful tool for ancient and modern materials

Giovanna Pintori [a,b], Elti Cattaruzza [a,*]

[a] Department of Molecular Sciences and Nanosystems, Ca' Foscari University of Venice, via Torino 155, Venezia-Mestre, 30172, Italy
[b] SG Lab Analytics, Nuova Ompi, Stevanato Group, via Molinella 17, Piombino Dese, 35017, Italy

ARTICLE INFO

MSC:
0000
1111

Keywords:
X-ray photoelectron spectroscopy
XPS
ESCA
Surface analysis
Glass
Corrosion

ABSTRACT

In the field of glass science and technology, as well as for historical glasses, a remarkable importance is devoted to the understanding of the interaction between the glass surfaces and the surrounding environment. Glass fabrication and preservation are very important issues in several research fields, involving both industrial and scientific problems. In general, a multi-technique approach should be used in order to achieve a better understanding of the complex phenomena involving reactions among glass surface atoms and environmental ones. In this frame, one of the most promising investigation technique is the X-ray photoelectron spectroscopy, XPS (also known as electron spectroscopy for chemical analysis, ESCA) mainly because of its ability to give information about the chemical bonds of the investigated atoms. In this paper the first part is devoted to the description of the basics of the technique, while in the second part several applications to the analysis of oxide glass surfaces are reported and discussed. The aim of this paper is to provide valuable help to all those who want to start or deepen the study of glass surfaces by this technique.

1. Introduction

Glass is an extraordinarily unique material. Its peculiarities are known to the common man, who appreciates the light and brightness of glass in everyday objects such as glasses and in the most sought-after objects such as Murano pearls, but also by the scientist who knows and explores its most hidden behaviours, discovering that it flouts the usual rules showed by other common materials, such as metals. Glass is in the transparent cup with which we can drink the divine nectar produced by land, grapes, hands and feet of man, but know it! - that cup is made of a material with diabolical properties. The same glass can make our daily life better, thanks to its functionalities explored for instance in smart windows or in optical fibres. But it remains a mysterious, articulated, multifaceted, elusive material. Its properties are never simply *hic et nunc*, but are strongly interconnected to its history, to the chronology of the thermal processes that led it to its final configuration . . . and it will really be the final and definitive one, for a material that always knows how to prove itself as sacred as hellish? Or is it only our desire as humans to claim it eternal, static, as if it were a cornerstone of our ability to dominate matter? We would like to melt you, glass, make you liquefy under the power of the god Vulcan and his fire: but you rebel, you do not flow, you soften and you cling, you let yourself be moulded only with several efforts, and your future stability is a bet made with times, temperatures and atmospheres, it requires both scientific knowledge and craftsmanship. . . With you there is always an eternal challenge, which is never completely won but which often allows us to touch the essence of Beauty. The poet Wisława Szymborska, Nobel Prize in Literature in 1996, wrote in one of her works that a man "*built itself a glass violin because he wanted to see the music*", thus giving us with this verse an effective idea of your aesthetic and poetic power. Scientists who want to reveal your innermost secrets have developed very sophisticated investigation techniques, with which they probe you and then observe your reactions, what you have to say and to tell. Today a lot is known about your intimate structure, your different compositions, the reasons why you appear colourful or transparent. . . Man continues to investigate the magical dances of your atoms, which, ever since you are in a viscous state, huddle next to each other in curious geometries and arrangements, almost always irregular but in the short-range. The bonds that are formed between the different species of atoms also depend on the atmosphere that is enveloping them and in which you are immersed, so these atoms find themselves almost being strangers, or interacting strongly when the right atmosphere is created — just like humans. And here these atoms, which you have been able to put at ease, decide to give you the power of possibilities: the colour you show to those who admire you.

Beauty, history, technology, innovation: it is exactly for all these reasons that the United Nations have approved 2022 as the International Year of Glass (IYOG 2022): as reported and declared in the YVOG website (https://www.iyog2022.org/), "*the year will celebrate the essential role glass has and will continue to have in Society. It will underline*

* Corresponding author.
E-mail address: cattaruz@unive.it (E. Cattaruzza).

https://doi.org/10.1016/j.omx.2021.100108
Received 21 September 2021; Accepted 29 October 2021
Available online 9 December 2021

the technological, scientific and economic importance of this often unseen transparent and enabling material which underpins so many technologies and which can facilitate the development of more just and sustainable societies to meet the challenges of globalization. It is also an important medium for art and its history is integral with that of humankind".

To put forth something more about diabolic, Wolfgang Pauli, Nobel Prize in Physics in 1945, said that "*surfaces were invented by the devil*". If one thinks about the surface of a solid, the atoms that compose it are the frontier between one world and another, a door to be crossed in order to access new possibilities, the development of physical and chemical rules that are amplified in the ambiguity of the border atoms. Also in the case of the most ubiquitous glass (the soda–lime silicate glass), used in several application such as display materials, pharmaceutical containers, photovoltaics and so on, the use of techniques allowing the investigation of the surface allows us to shed light onto very complex phenomena related to the reactivity between glass and environment atoms, that can lead to alteration of the surface chemistry and structure, the network connectivity, the fraction of bridging and non-bridging oxygens, the corrosion resistance and strength, the leaching of network modifiers, the adsorption, the wettability, the hydrophobicity... Every investigation technique is characterized by its own pair "probe beam–detected beam", as well as by a typical sampling depth defining the thickness of the analysed surface. Among the surface investigation techniques, X-ray photoelectron spectroscopy (XPS), also known as electron spectroscopy for chemical analysis (ESCA), employs a soft X-ray beam to induce emission of electrons from the irradiated surface, with a sampling depth that is usually around 5–10 nm. In addition to the possibility to detect and distinguish different elements (from Li to U), the real peculiarity of XPS is its ability to provide quantitative information on the chemical state of the detected elements, namely on the chemical bonds among them. Alone or in conjunction with other techniques for surface analysis, XPS is actually a very powerful tool to investigate glass surfaces, in spite of the difficulties related to surface charging during X-ray irradiation of insulating materials (recently reduced by technical solutions opening new and interesting perspectives, as explained below).

This paper is grouped into two main parts. The first part is intended to be a practical guide for XPS users: starting from the basic theory and from XPS instrumentation, that are illustrated in Section 2; followed by the particular case of XPS performed on insulating materials (Section 3), and the potentiality of depth profiles strategies (Section 4). Researchers at all levels of experience will find useful information in order to plan, conduct, and report XPS measurements. In the second part, after a brief review of glass compositions and structures, a collection of practical examples is provided, in which the ability of XPS to obtain bulk chemical state information and to give new insights into the structural features within glasses is demonstrated (Section 5). The reader is then introduced to the complex mechanism of glass corrosion in Section 6, and finally a series of significant papers where surface glass degradation processes are investigated by XPS is reported in Section 7.

2. Basics of X-ray photoelectron spectroscopy

X-ray photoelectron spectroscopy (XPS), also called Electron Spectroscopy for Chemical Analysis (ESCA) is a widely used method to identify and quantify the elements present at the surface of solid materials as well as to some extent their chemical bonds. This technique is based on the well-known photoelectric effect [1], explained by A. Einstein in 1905 [2]: its analytical use was firstly proposed by Kai Siegbahn [3], which developed sophisticated instruments to study the energy spectrum of the photoemitted electrons. During XPS measurements, the sample is irradiated with soft X-rays (energies of few keV) and the number of emitted photoelectron as a function of their kinetic energy is determined to provide a spectrum. The energy distribution allows to determine the binding energy distribution, containing information about the chemical element and its oxidation state, potentially allowing to identify and quantify the composition and the chemical state of the sample surface species. The sampling depth is determined by the kinetic energy of the photoemitted electron, ranging from few nm to 10–20 nm, depending on the X-ray source energy. All elements except hydrogen and helium can be directly detected, with sub-monolayer sensitivity [4]. Specific studies have been conducted on gases and liquids, but the significant part of applications are for solid samples, where XPS has been extensively applied to deal with practical issues concerning the surface, namely, corrosion, oxidation, surface segregation, contamination and cleaning, adhesion and bonding, and many other properties. Different kind of samples, such as metals, ceramics, glass, coatings, biomaterials, polymers, and moreover, in multiple forms, as for instance, solid, thin films, and powders can be examined.

2.1. Basic theory

When a solid sample is irradiated by a beam of X-rays of energy $h\nu$, electrons in orbitals with binding energies less than $h\nu$ can be ejected from the atoms. They are subsequently detected in a spectrometer and analysed in terms of their characteristic kinetic energies (KE). From the principle of the conservation of energy and in the monoelectronic approximation, it can be demonstrated that the binding energy (BE) of the emitted electron is related to the difference between the energy $h\nu$ of the incident X-ray radiation and the KE:

$$BE = h\nu - KE - \Phi_{spec}, \tag{1}$$

where the binding energy is referred to the Fermi level (see Fig. 1). The term Φ_{spec} is the work function of the spectrometer in ohmic contact with the solid sample (its values is typically 3–5 eV). For insulating samples the binding energies, in addition, have to be corrected for charging effects.

Mg K_α (1253.6 eV) or Al K_α (1486.6 eV) X-ray anode sources are commonly used for XPS in lab. instruments: the typical spectrum plots the number of emitted electrons as a function of their binding energy. An example of an XPS wide-range scan (survey scan) spectrum is reported in Fig. 2.

2.1.1. Core levels

Large part of the information obtained from XPS measurements relies on the observation of photoelectrons emitted from core levels of the atoms in the sample surface region. The ionizing radiation is able to access at least one core level for all elements, with binding energies falling in the range 10–1400 eV for the most common used X-ray sources. These binding energies are well-known and tabulated [6], with minimal overlaps, ensuring that the XPS spectrum provides a possible indication of all elements present in the sampled region (behind the detection limit, usually around few $^{o}/_{oo}$ at.). Photoelectrons coming from the core levels are indicated by the element and the orbital from which they were ejected. In case of *p*, *d*, and *f* levels, these latter are always splitted by spin–orbit coupling into doublets, due to the so-called *j-j* coupling of the electron orbital angular momentum, indicated by the quantum number l (for instance $l = 1$ for a *p* electron) and the spin angular momentum, indicated by the quantum number s ($s = \pm 1/2$). In the reported example, the *j-j* coupling originates the $2p_{3/2}$ and $2p_{1/2}$ doublet. Often, this energy separation falls below the energy resolution limit of the technique: as an example, in most cases the Si 2p energy splitting is too small to be evidenced, as in Fig. 2. The most intense signal for a given element is normally preferred for surface analysis. The 1s level is employed for the light elements (Li, Be, B, C, N, O, F, Ne, and Na), the 2p electrons for Mg, Al, Si, P, S, Cl, Ar, and the first row transition elements and the 3d and 4f levels for heavy element analysis. In Fig. 2, the Si 2s and Si 2p levels have similar peak heights but the Si 2p level has a narrower linewidth and this line usually is used to extract chemical state information for Si in different compounds.

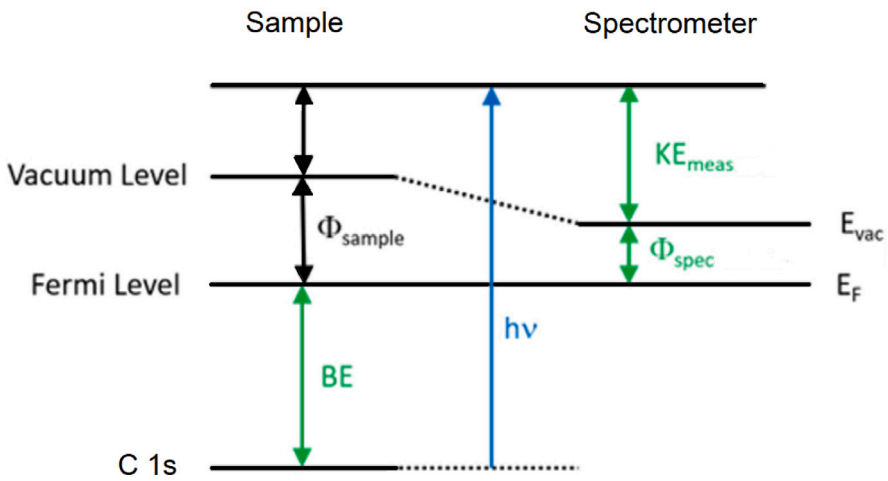

Fig. 1. Energy level diagram illustrates schematically the basic XPS equation, including the X-ray source energy (hν), the binding energy of the electron (BE), the measured kinetic energy of the electron (KE_{meas}), and the work function of the spectrometer (Φ_{spec}) [5].

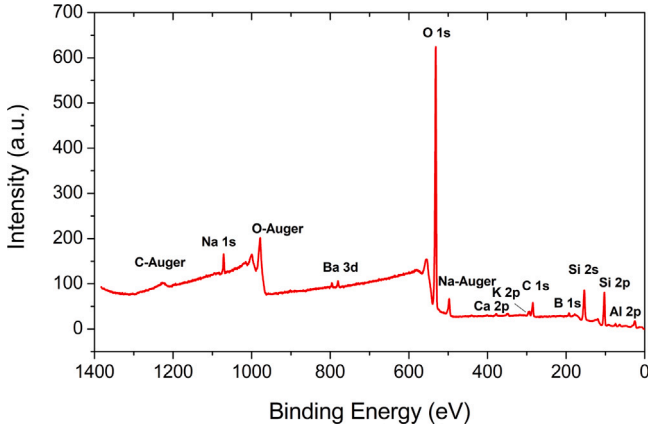

Fig. 2. Survey spectrum for borosilicate glass recorded by using monochromatic Al K_α source. Major spectral lines and Auger lines are labelled.

2.1.2. Auger electrons

When a core electron is ejected in the normal photoemission process, this excited ionized state can relax by filling the created vacancy with an electron coming from a higher electron level. This relaxation process can release energy by two competing processes, radiative or nonradiative: in the first one the energy excess induces the emission of a photon (X-ray fluorescence), in the second the energy excess allows the emission of an additional electron from an outer shell (called Auger electron). In the last case, the Auger electrons are detected as for the photoemitted electrons, originating additional bands in the XPS spectrum. These signals are often used for qualitative analysis. The notation of Auger peaks traditionally is based on the K, L, and M nomenclature for atomic orbitals, indicating the three electronic levels involved in the whole process: the vacancy level; the level from which comes the electron filling the vacancy; the level from which the additional (Auger) electron is emitted. The Auger process involves these three different electronic levels (indicated as A, B, and C) and the kinetic energy of the ejected Auger electron is determined in Eq. (2):

$$KE_{Auger} = BE(A) - BE(B) - BE(C). \quad (2)$$

Since often the kinetic energies of the Auger electrons are in the range investigated by XPS, signals due to Auger transitions are usually encountered in the XPS spectrum. In Fig. 2, the KLL Auger bands of sodium, oxygen and carbon can be clearly observed. In some cases, the position of the Auger line facilitates the identification of the chemical state of the element (see Section 3.3). Since the binding energies of the three electron levels involved in the Auger transition do not depend obviously on the X-ray source energy, this implies that the kinetic energy of the emitted Auger electron is also independent of the X-ray excitation energy. Thus, when different X-ray sources are employed for excitation, the calculated "fictitious" binding energy of the Auger electrons will change. Considering that Auger lines can overlap photoelectron lines, it is convenient to use a different X-ray source in order to separate those overlaps (if a dual anode X-ray source is available).

2.1.3. Valence levels

The electrons of the outer shells are those which are involved in chemical bonding. Since the intensity is generally weak compared to the core levels, this region of the spectrum is not useful for elemental identification. However, in certain circumstances, information about molecular orbitals in compounds can be gained [4]. The valence band can also act as a fingerprint for specific organic structures, but interpretation generally requires comparison to some reference.

2.1.4. Surface sensitivity

The X-rays that irradiate the sample can penetrate quite deeply (usually a few μm) into the sample, inducing electrons emission. However, only photoelectrons originating from the outermost surface layers can reach the solid surface without changing their kinetic energy for inelastic scattering, thus leaving the sample for being detected. This is related to the limited distance that electrons can travel in the solid before losing energy through inelastic collisions (collisions that involve the loss of energy) against other electrons in the material. These scattered photoelectrons contribute to the vertical step in the background signal (see Fig. 2). Only the electrons leaving the surface without any inelastic collisions will contribute to the characteristic photoelectron bands, maintaining the information (the unchanged kinetic energy) that allows identification of the emitting atoms by Eq. (1). As a consequence, the surface sensitivity of XPS is determined by how deep an electron can be generated and still escape without inelastic scattering. Beer's law describes the intensity I of the electrons emitted from a sample along a determined direction without suffering inelastic scattering, where I_0 represents the total intensity of electrons emitted along the same direction at depth d below the sample surface:

$$I = I_0 \exp(-d/\lambda sin\theta). \quad (3)$$

The term λ is the attenuation length of the electron, which depends on the kinetic energy of the electron and on the material through which it is travelling. θ is the angle between the sample plane and the detected electron trajectory. The attenuation length (see Fig. 3) is similar to the

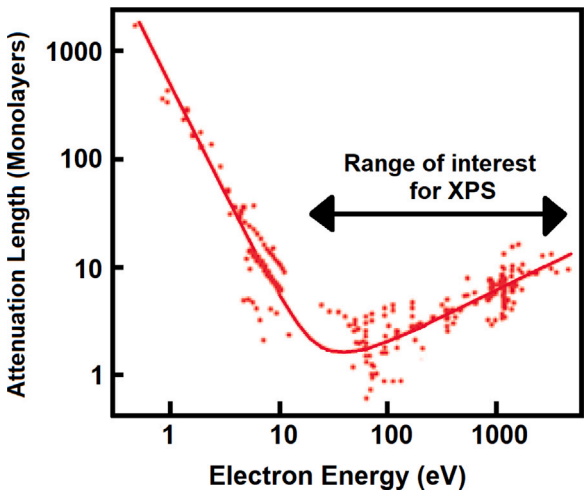

Fig. 3. Electron attenuation length as a function of kinetic energy. Each data point represents a different element or transition [9].

inelastic mean free path (IMFP) [7] of the electrons, that is defined as the average distance an electron with a certain kinetic energy can travel before inelastic scattering. However, the attenuation length also takes into account the effect of elastic scattering, that changes the electron trajectory without changing its kinetic energy. Detailed studies of both attenuation length and IMFP are available in Ref. [8].

From Eq. (3), it can be shown that 95% of the detected signal originates from a depth $d = 3\lambda sin\theta$, thus about 95% of the electrons will escape usually from a depth of 10 nm or less. The information depth, commonly called the sampling depth, is defined as the maximum depth normal to the surface from which useful information is obtained. By observing the variation of the photoelectron intensity with θ, the effective sampling depth of the XPS measurement can be changed. This provides an indication of the relative distribution of different elements in the surface layers. More details are reported in Section 4.1. For electrons typically analysed with XPS (i.e., with KE > 100 eV), the IMFP increases roughly as the square root of the kinetic energy. Higher energy X-ray sources generate electrons with higher kinetic energies (Eq. (1)), and, therefore, able to escape from larger depths. Thus, analysis with different X-ray sources allows the researcher to probe different depths within the sample. As an example, the information depth for Si 2p electrons by using a Cr K_α source is more than two times that for Al K_α source [5].

2.1.5. Chemical environment

The binding energy of a core electronic level is determined by the electrostatic interaction between the electron and the nucleus: for the same core level it depends on the atomic number of the atom involved, because the electrostatic shielding of the nuclear charge from all other electrons in the atom (including valence electrons) influences the effective positive charge experienced by the electron leaving the atom. Removal or addition of electronic charge as a result of variation in the chemical bonds of the emitting atom can alter the shielding: the exact value of the binding energy of a core electron is then affected by the atom's chemical environment, due to differences in chemical or structural configuration. The induced chemical shift, which can reach some eV, can be recognized and used to achieve information on the chemical bonds among the atoms at the sample surface.

2.1.6. Linewidths

The full width at half maximum (FWHM) of an XPS band, that is the observed overall linewidth Γ_{TOT}, can be written to a first approximation:

$$\Gamma_{TOT}^2 = \Gamma_{instr}^2 + \Gamma_{solid}^2 \quad (4)$$

where

$$\Gamma_{instr}^2 = \Gamma_{source}^2 + \Gamma_{electron\ analyser}^2 \quad (5)$$

and

$$\Gamma_{solid}^2 = \Gamma_H^2 + \Gamma_{extra}^2. \quad (6)$$

As shown by Eq. (5), the two contributions to the instrumental width Γ_{instr} come from the source linewidth (Γ_{source}) and the width related to the resolution of the electron analyser ($\Gamma_{electron\ analyser}$). When non-monochromatized Mg K_α and Al K_α radiation are used, linewidths Γ_{source} assume the following values: 0.8 and 1.0 eV, respectively. Conversely, when a monochromatized Al K_α radiation is employed the Γ_{source} is ≤0.4 eV. The electron linewidths ($\Gamma_{electron\ analyser}$) on modern instruments can be as low as 0.1 eV. Thus, from Eq. (5), the Γ_{instr} for a laboratory monochromatized Al K_α source can be as low as ~0.3–0.4 eV, whereas Γ_{instr} for a synchrotron radiation source can be less than 0.1 eV. The Heisenberg lifetime (or natural lifetime) width Γ_H (Eq. (6)) is given by the Heisenberg uncertainty principle, which in units of eV becomes:

$$\Gamma_H = \frac{4.56 \times 10^{-16}}{t_{1/2}}, \quad (7)$$

where $t_{1/2}$ is the half-life of the hole state (the core-ionized atom). Γ_{instr} and Γ_H are not significant contributors, while Γ_{extra} must be the dominant contribution to Γ_{TOT} [10]. For example, in nonconductor solids, there are six additional contributions to Si $2p_{3/2}$ linewidths, that contribute to define Γ_{extra}. These are: (1) differential charge broadening for nonconductors, Γ_{DC}; (2) broadening or asymmetry from surface contributions, Γ_{surf}; (3) chemical shift broadening from inequivalent atoms in the crystal structure, Γ_{CS}; (4) inhomogeneous work functions from band bending variations, Γ_{WF}; (5) final state vibrational contributions, Γ_{FSVB}, which should be temperature independent below room temperature; and (6) phonon broadening, Γ_{PB}, which is temperature dependent [11].

2.1.7. Complex structures

The monoelectronic approximation of the photoionization process is not so good in some particular cases, showing that the photoemission process is actually a multielectron process. When photoionization induces the emission of an electron from an inner shell and this emission is so fast that the outer shell electron cloud have no time to relax, then the interactions between the emitted photoelectron and the electron cloud left behind may reduce the kinetic energy of the photoelectron, thus originating an additional signal centred at higher binding energies with respect to the main line. These signals are called shake-up if they refer to an excitation in the final system, or shake-off if the residual energy induces the loss of one (or more) electrons from some outer shell of the ion. In other words, these satellites bands (shake-off and shake-up) can be seen as the consequence of a sudden change in Coulombic potential as the photoemitted electron crosses the valence band. Typical examples of shake-up structure are clearly visible in the $2p_{3/2}$ spectrum for Cu^{2+} species [12].

Another effect originating a complex structure of the XPS electron band is the multiplet splitting: it takes place when unfilled electron shells contain unpaired electrons. When photoionization creates a core electron vacancy, a coupling between the unpaired electron in the core shell with the unpaired electrons in the outer shell can take place: in this case a certain number of final states are originated, appearing in the photoelectron spectrum as an envelope of several signals, close each other in binding energy. Compounds of transition metals such as Cr, Mn, Fe, Co and Ni usually exhibit significant multiplet spitting, as well as some heavy metals.

An additional effect taking place in particular samples (for instance, pure metallic materials) is the energy loss by absorption due to plasma resonance modes (collective oscillation of the electrons). In these materials, plasmon loss peaks may occur: the photoemitted electrons has a

certain probability to loss a specific amount of energy (called plasmon energy) due to the interaction with other electrons, in particular with the free electron of the conduction band. This energy loss occurs in well-defined amount, arising from group oscillations of the conduction electrons and originating less intense equally-spaced bands on the higher binding energy side of the main peak.

2.2. Quantitative analysis

As analytical technique, a fundamental aspect of XPS is its capability of quantifying the relative elemental concentrations from the recorded spectra. By considering the probabilities of photoelectrons production, transport of the electrons through the material to the surface without energy loss, and subsequent detection in the spectrometer, the photoelectron band intensities can be related to the concentration of the emitting atoms. However, all the involved factors such as the number of detected electrons, the photoelectric cross-section, the X-ray flux, the detector efficiency, the inelastic electron-mean-free-path, the sample analysed area, the analyser transmission efficiency, are difficult to estimate with high precision and accuracy, preventing a reliable evaluation of the unknown density. Usually, an empirical approach is applied, using tabulated atomic sensitivity factors or by comparison with standards of known composition: this allows the determination of an observed elements as an atomic fraction [4,5,13]. The way to determine in XPS the (relative) concentration of the different detected elements is then based on the measured areas under the main core-level bands of all elements present in the sample. For a homogeneous sample containing n elements the atomic fraction x_i of element i is then given by:

$$x_i = \frac{A_i/s_i}{\sum_{j=0}^{n} A_j/s_j}, \tag{8}$$

in which A_i is the area under the corresponding core-level peak, and s_i is the relative sensitivity factor (RSF). The latter is an experimentally-determined value, which is specific for each instrument and for each core-level peak (typically normalized to one specific signal like C 1s or F 1s). Using tabulated sensitivity factors [14], the uncertainty of this approach is of the order of 10% of the determined concentration, and can be improved further by measurement of standards matched to the composition of the unknown. As reported, RSF can be influenced by the instrument-related factors like the transmission function of the spectrometer [15]. As a consequence, the best results are obtained if the RSFs are specifically determined on the same instrument used for quantification and under the same experimental conditions (pass energy, anode power, aperture size, etc.).

In order to ensure that the information is representative and as accurate as possible, different aspects should be considered to obtain reliable, meaningful, and useful information from quantitative XPS. This includes the requirement for a consistent and rigorous method for the separation of inelastic background from electron band. For more details see Refs. [16,17].

2.3. Correction for hydrocarbon contamination covering layer

The exposure of the surface to adventitious entities or contaminants, such as carbon, causes the attenuation of the signals from the other elements present in the sample depending on the electrons inelastic mean free path through the elements under study, thus altering the measured atomic concentrations. As a consequence, the direct calculation of atomic percent compositions through the simple renormalization of the data, without further correction can give rise to misleading results.

Smith [18] proposed a simple method, easy to implement, and that requires no additional data acquisition and only minimal data processing beyond that which would normally be undertaken. The first step is the determination, by standard methods, of the carbon concentration on the surface, this can result in a few tens of atomic percent, depending on the degree of contamination. Hence, under the hypothesis that the carbon contamination is homogeneously covering the sample surface, the latter can be converted directly to an overlayer thickness, d, in nanometres, by the use of a modified form of the Beer–Lambert law:

$$d = -\lambda_{C1s}\, cos\theta\; ln(1 - 0.01x), \tag{9}$$

where λ_{C1s} is the electron attenuation length for carbon 1s photoelectrons, θ is the electron takeoff angle relative to the sample normal, and x is the surface concentration of carbon in atomic percent. The hydrocarbon overlayer causes the preferentially attenuation of the emitted electron with higher binding energy (lower kinetic energy), thus inducing an underestimation of that element. Once evaluated the hydrocarbon contamination thickness, d, using Eq. (9), this may be corrected by estimating a more correct signal intensity without the effect of the hydrocarbon layer as follows:

$$I_{corr} = I_{meas}\; exp\left(\frac{d}{\lambda\; cos\theta}\right), \tag{10}$$

where I_{meas} is taken as the atomic percent composition determined before correction, and λ is the effective electron attenuation length for photoelectrons from the element and line of interest in the hydrocarbon overlayer. The calculation is carried out using Eq. (10) for all elements in the sample, except carbon identified as contaminant. Finally, the resulting values of I_{corr} are then renormalized to 100% to obtain an estimate of the composition without the hydrocarbon contamination. The data correction can be carried under the assumption that the sample has a uniform composition within the XPS sampling depth (except for the presence of the hydrocarbon contamination layer). The author claims an improvement around 30% in the accuracy of the analysis after application of the correction for the hydrocarbon, as described in details in Ref. [18].

An example of quantitative analysis and the way in which the method described above is applied is provided in Table 1, for an investigation of a borosilicate glass: the results of the measurements and data analysis are summarized. The table columns show, from left to right, the atomic species analysed, the elements and lines indicated, the apparent composition as-measured, the apparent composition after normalization to exclude carbon due to the hydrocarbon layer, the apparent thickness of the hydrocarbon layer determined using Eq. (9), and the corrected compositions using the method described above.

Table 1
Borosilicate glass analysis: summary of results before and after correction for the hydrocarbon contamination layer.

Element	Element and line	Atomic %	Normalized atomic %	C thickness (nm)	Corrected atomic %
	C 1s	12.6		0.33	
Na	Na 1s	4.6	5.3		6.1
O	O 1s	59.7	68.3		68.3
Ca	Ca 2p	0.4	0.5		0.4
B	B 1s	3.8	4.3		4.2
Si	Si 2p	16.5	18.9		18.3
Al	Al 2p	2.4	2.7		2.7

2.4. Instrumentation

An XPS instrument, depicted schematically in Fig. 4 (a), contains an X-ray source, an electron energy analyser, sample handling components, extraction lenses, and detector housed in an ultra-high vacuum (UHV) chamber. All the main components are discussed below. Detailed descriptions of instrument components can be found in Ref. [5] and therein.

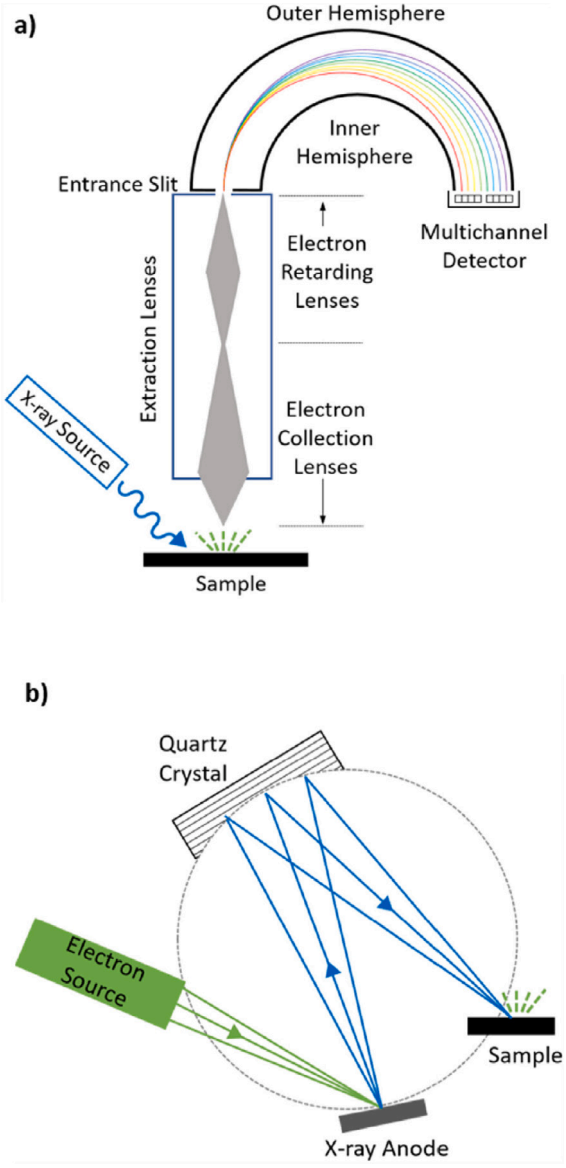

Fig. 4. Schematic diagrams show the major components of an (a) XPS instrument and (b) monochromator [5].

2.4.1. UHV chamber

XPS instruments are housed within ultra-high vacuum environments for two reasons. First, the emitted electrons must not scatter off residual gas molecules while travelling to the analyser, in order to preserve its kinetic energy unchanged, and this requires vacuum levels on the order of 10^{-5}–10^{-6} mbar. Second, XPS is very sensitive to surface contamination: in order to avoid adsorption of gaseous species on the sample surface during measurements, XPS instruments must utilize the UHV environment. Actually, XPS systems have working pressures closer to 10^{-9}–10^{-10} mbar.

2.4.2. X-ray source

Characteristic X-rays are produced by bombarding an anode with high energy electrons (10–15 keV) from a heated filament of tungsten or LaB_6 (lanthanum hexaboride). Several factors determine the choice of the anode material:

(1) Energy: the transitions that can be measured depend on the energy of the source. Moreover, as mentioned before, the energy can determine the sampling depth.

(2) Linewidth: for non-monochromatic sources, the natural linewidth will limit the resolution of the measurement. Conversely, monochromatic sources offer much narrower linewidths, the better way to distinguish small chemical shifts.

(3) Ionization cross section: the probability that an atom will lose an electron due to X-ray irradiation decreases for lower binding energy electrons produced by higher energy sources [5].

Originally, XPS systems were equipped with aluminium or magnesium sources, commonly in the form of a dual anode source that includes both Al and Mg anodes which can be individually selected. Typical operating powers are in the range of 10–500 W. The target is generally cooled by recirculating water on the atmosphere side of the anode [4]. The natural width of the K_α X-ray line is 0.8 eV for magnesium and 1.0 eV for aluminium. The latter can be improved to below 0.3 eV by the use of quartz crystal monochromators, since quartz has the correct d-spacing for diffraction of Al K_α [4]. Repositioning the quartz crystal can also allow monochromatization of Ag L_α X-rays, and dual anode monochromatic Al/Ag sources are now available. Other monochromatic sources, such as chromium, can also be used.

Monochromatic sources have several advantages. The first one is that the monochromator (Fig. 4 (b)) eliminates any excitation by X-ray lines other than the most intense main line. For example, a non-monochromatic Mg X-ray source will irradiate the samples with the most intense Mg $K_{\alpha 1,2}$ line but also with other less intense lines. As a consequence, additional peaks due to excitation with multiple X-ray energies will appear in the XPS spectrum, and they are called satellite peaks. One of the few disadvantages of employing a monochromator is that it reduces X-ray flux, but advancement in electron collection and detector efficiency have made this a minor issue on modern instruments.

Typically, a very thin aluminium window is placed after the source to reduce bremsstrahlung radiation and electrons from the X-ray beam. This is especially important for non-monochromatic sources where the bremsstrahlung radiation is not removed by the monochromator. Since the number of electrons emitted is proportional to the X-ray source intensity, the source is designed to provide a high fluence of X-rays, however, some samples can be damaged by high X-ray intensity [5]. A typical signal that sample damage is occurring includes spectral changes, such as peak broadening over time.

Simple X-ray sources illuminate an area a few millimetres in size. XPS instruments with small-spot X-ray sources are also available, with spatial resolutions of 10–100 μm. In these systems, the exciting electrons are focused onto the anode surface to produce a stationary or scanned X-ray beam. XPS experiments can also be conducted at several synchrotron radiation sources, where spatial resolutions approaching 1 μm have been achieved.

2.4.3. Electron energy analyser, detectors

The electron energy analyser measures the energy spectrum of the electrons emitted from the solid. Two main types of analysers were developed for XPS systems: cylindrical mirror analysers and concentric hemispherical analysers [19]. Over time, the concentric hemispherical analyser (CHA) design proved to have better performance with respect to energy resolution. Electrons will pass from the entrance slit to the exit slit if they have the correct kinetic energy, as determined by the potential difference maintained between the two hemispheres and their radii (typically 100–200 mm). Electrons of other energies will not be successfully focused onto the exit slit, and therefore will not be counted by the detector (see Fig. 4 (a)).

Usually, the potentials on the CHA are set to a constant value to transmit electrons of a single energy, called the pass energy. The pass energy is set to a higher value to maximize throughput for survey scans (e.g., Fig. 2), and to lower values to enhance resolution when detailed scans are acquired (e.g., Fig. 5 and Fig. 6). By scanning an electron lens fitted to the entrance aperture, the energy spectrum of the electrons emitted from the sample is obtained. This arrangement allows

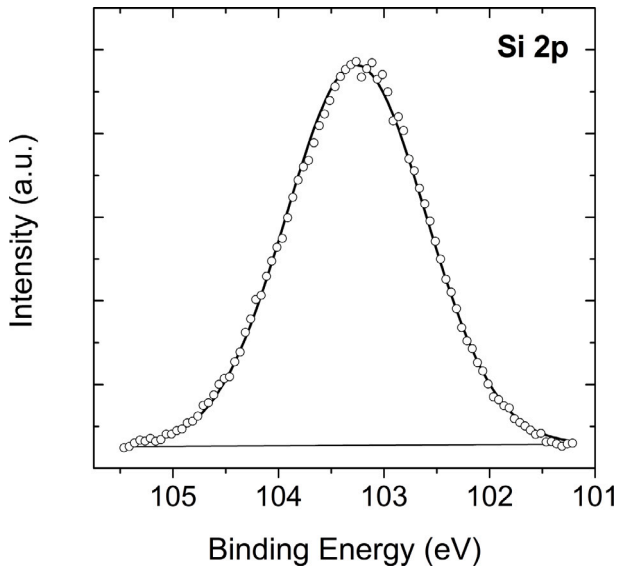

Fig. 5. Si 2p narrow-range spectrum of borosilicate glass. A Shirley background is included (solid curve at base of peak) and the fit is represented by a solid line intersecting the data points.

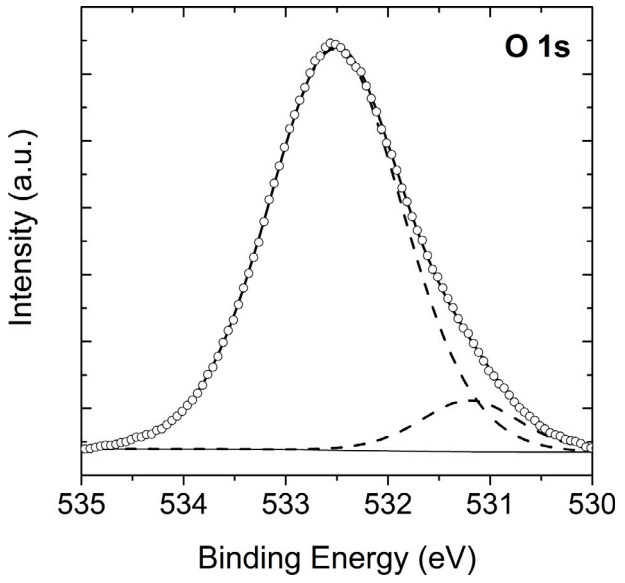

Fig. 6. O 1s narrow-range spectrum of borosilicate glass. Two components have been identified, the bridging oxygen (532.5 eV) and non-bridging oxygen signals (531.1 eV), that are represented by dashed lines. A Shirley background is included (solid curve at base of peak) and the fit is represented by a solid line intersecting the data points.

for a larger operating distance between the sample and the analyser, and a constant energy resolution ($\Delta E/E_{pass}$) is maintained across the spectrum.

Between the sample and the analyser are a set of electron optics called extraction lenses. These lenses define the acceptance angle for gathering electrons emitted from the sample. Although there are experiments for which lower acceptance angles are preferred (e.g., angle-resolved XPS), commonly, a large acceptance angle is used to improve electron collection efficiency. On some systems, extraction lenses can also control the area of the sample from which electrons are collected, thereby enabling small spot analysis [5]. Some XPS instruments define the analysis area using schemes based on the focusing characteristics of the electron lens and energy analyser, and can provide a spatial resolution of ca. 2–10 μm. The transmitted electrons are typically detected by a channeltron electron multiplier at the exit slit, coupled with pulse counting electronics (single electron counting). Higher counting statistics can be sustained by using an array of detectors, with multiple exit slits positioned along the energy dispersion direction, or by the use of position-sensitive detectors. 2D position sensitive detectors provide imaging and higher collection efficiency. More information on detectors can be found in the XPS literature [19].

2.4.4. Accessories

Insulating samples can accumulate a positive charge on the surface during XPS analysis, changing the kinetic energy of the photoelectrons as they leave, thus causing unwanted peak shifts and distortions in peak shapes [20–25]. In extreme cases, especially when monochromatic X-rays are used, a steady-state charging of the surface may never stabilize, precluding the collection of any useful data unless this charge is controlled or compensated. For this reason XPS systems are commonly equipped with an electron flood gun, which generates a flux of low energy (1–10 eV) electrons incident on the surface providing the surface potential stabilization. The electron flood gun is almost always used in the XPS analysis of polymers, glasses, ceramics, and other insulators. Another useful accessory is an ion sputter gun, which provides a beam of energetic (1–5 keV) inert gas ions (e.g., Ar^+ or Xe^+) directed at the analysis area. Bombardment of the surface results in the removal of the surface layers in a controlled manner. In these experiments, XPS data are acquired, the sample is sputtered for a short amount of time, and then XPS data are acquired again. This is a useful approach for thin film analysis and investigation of buried interfaces, performing a "in-depth" analysis of the sample. Both charging compensation methods and ion sputtering are described in more detail in Sections 2 and 4.

3. Insulating samples and surface charging

Surface charging is influenced by several factors: sample properties, spectrometer, sample mounting technique. Typically, for conducting and semiconducting samples an electrical contact is made to the surface of the sample, and the sample holder is grounded. Hence, the electrons lost due to photoemission can be replaced through this connection to ground, however this strategy does not work well for insulating samples.

For insulating materials or materials electrically isolated from the spectrometer, the emission of photo- and Auger-electrons from the sample surface leaves a positively charged surface [21,22]. The surface potential charge will affect the kinetic energy of emitted electrons, thereby shifting the measured energies of the photoelectron peaks to apparently higher binding energy, and often presenting distorted peak shapes. This binding energy shift may reach a nearly steady-state value of between 2 and 5 eV for spectrometers equipped with non-monochromatic X-ray sources, making difficult to determine binding energies with the accuracy needed for elemental identification or chemical state determination [26]. With the early non-monochromatized Mg K_α and Al K_α sources, the positive charge is less prevalent on non-conductors, as the thin aluminium window which separates the source from the sample surface allows for discrete neutralization of insulating surfaces by creating a rich source of secondary electrons in the vicinity of the analysis area [10]. Since the introduction of monochromatized sources in the 1970's, where the X-ray source is far from the sample, the aluminium window is absent, thus the positive charge build-up could not be neutralized by low-energy electrons impinging on the specimen surface from the X-ray source.

Charge build-up during XPS analysis is a well-studied time-dependent three dimensional phenomenon that occurs along the sample surface and into the material [27,28]. The amount of induced positive charge near the surface, its distribution across the specimen surface and its dependence on experimental conditions are determined by many factors, including those associated with the specimen: i.e., composition,

homogeneity, magnitude of surface conductivity, total photoionization cross-section, surface topography, and characteristics of the spectrometer, as spatial distribution of the exciting X-rays, and availability of neutralizing electrons. Charging often affects different parts of the sample differently, in complex or even in relatively simple materials. Causes of this phenomenon, known as differential charging [29–32], include variations in photoelectron yields, film or sample thickness and composition variations, and charge trapping at phase boundaries or interface regions. Some specimens undergo time-dependent changes in the level of charging as a consequence of chemical changes or volatilization induced by photoelectrons and secondary electrons, X-rays or heating. Such specimens may never achieve steady-state potentials.

In general, differential charging occurs as a result of a potential gradient establishing within or across the surface of a sample [21]. The photoelectron spectra collected from areas of differing potential include extremely distorted and broadened peak shapes, thus complicating the identification and the quantification of the chemical state. According to the classification of charging phenomena by Yu and Hantsche [33], *lateral differential charging* can arise through inhomogeneities of the sample composition, resulting in both peak shift and broadening. *Vertical differential charging* has been observed with inhomogeneous layered structure, such as thin insulating films on (semi)conductors in good electrical contact with the spectrometer [33–35], this results from electrons flowing from the ground to the analysed surface and vanishes when the sample is insulated from the spectrometer [33]. This effect can be induced by external fields and internal current.

Tielsch and Fulghum [36] conducted an interesting study on the differential charging in a bulk insulator, i.e., silica glass, using photoelectron imaging and small-area spectra acquired with a monochromatic X-ray source. They demonstrated that the charge shifts and photoelectron peak shapes vary as a function of X-ray flux on the sample, indicating that lateral charging is the dominant mechanism on a bulk insulator. The authors assume that a positive charge density distribution arises on a non-conducting uniform sample upon exposure to X-rays, causing the lateral differential charging. The latter is due to the non-uniformity of the X-ray beam and from the fact that the area viewed by the analyser is larger than the irradiated area. In certain spectrometers, a metal grid placed close to the surface further minimizes the lateral differential charging described above. As a consequence of non-homogeneous surface charging, the resulting photoelectron spectra are shifted to a higher binding energy than expected, and contain a long tail on the low-binding energy side (see for instance Ref. [37]).

If the charging phenomena is caused principally by potential fluctuations across the surface of the sample, the highest binding energy component will come from the centre of the X-ray spot, since the sample charging should be most significant at the point of highest X-ray flux. The tailing structure is then an effect of the decreasing charge gradient as one moves away from the centre of the X-ray spot. Although changes in surface potential during XPS analysis can complicate analysis, in some circumstances, such phenomena can be used to extract important information about samples [29–32,37,38]. Processes that lead to charge build-up and migration can also drive changes in sample composition and structure, known as damage. Overviews of electron damage processes by Pantano et al. [39] and Baer et al. (Ref. [25] and references) also provide some indication of the sensitivity of different materials and different molecular groups to electron damage.

To obtain useful information, a charge neutralizing system that possibly eliminates (or at least makes homogeneous and constant-in-time) the surface potential distribution, and hence the differential charging effect, is required. For this purpose, several techniques have been developed in order to obtain meaningful and reproducible data from insulating samples [21–26]. In addition, several strategies have been provided with the aim of correcting the binding energy shifts that result from surface charging. These corrections are performed after the data acquisition and are discussed in Section 3.1. Despite the detailed methods used to control surface charge may depend on the available instrument as well as the specimen being analysed, there are some common features associated with recognizing the presence of charging and some conventional tests to verify that the charge control systems are working correctly. Unfortunately, although there is an ASTM guide to charge control and charge referencing in XPS [26] and there is an ISO standard [40] for reporting methods of charge control and charge referencing, there is no universally accurate method to adjust or correct binding energies in the presence of surface charging for insulating materials.

3.1. Charge compensation methods

Modern spectrometers, equipped with monochromatized X-ray sources, all employ some form of charge neutralization: either an electron flood gun or a combination of electron and ion beams directed towards the sample being analysed, with the aim to reduce the effects of charging observed in the spectrum. Charge neutralizers are typically located above the sample in the vacuum chamber and they supply a source of low energy electrons (1–5 eV) or ions (<5 eV). In such spectrometers, a magnetic confinement system has been employed, where a "sea" of low energy electrons floats above the entire sample, and these are available to neutralize any positive charge on all parts of the sample, regardless of surface morphology (i.e., surface "highs", "lows" or "slopes"). The magnetic lenses are principally used to enhance the electron collection efficiency, but also play a crucial role once used together with the filament acting as a source of low-energy electrons (electron flood gun). The magnetic field lines of the snorkel lens, indeed, define the path of photoelectrons leaving the sample surface on their way to the analyser entrance slit. Concurrently, they also define the path for electrons originating from the filament and travelling in the reverse direction towards the sample surface in order to compensate for charge loss [22].

The principle of this process is illustrated in Fig. 7 adopted from Ref. [22]. The spiral electron track represents the path of an electron departing and returning to the surface. The electrons generated at the filament drift horizontally into the lens aperture, then they are trapped by the field lines and spiral towards the sample surface in the analysed area. This system guarantees a reduction of the differential charging, leading to much narrower linewidths, and to collection of a much greater amount of chemical state information. However, samples still charge in this instrument, even though uniformly. Furthermore, it is still critical to use a standard, that should be internal to the spectrum, in order to calibrate BE of all spectral peaks.

When highly focused X-rays were first introduced, new challenges with charge neutralization appeared, i.e., to guarantee highly local charge compensation and to avoid lateral inhomogeneity in charging. The solution proposed has been to partner the electron flood gun with a low-energy ion flood gun producing a shower of <5 eV positive ions, thus below the energy required for bond breaking [22,41]. The use of argon as a neutralizing agent has been used previously in both SIMS and AES communities [42,43] and is employed to suppress charges on the sample surface in unilluminated area surrounding the X-ray footprint, aiding the neutralization of the illuminated region with the low energy electrons. The resulting system is schematically shown in Fig. 8. The low-energy ions cover a wide area of the sample while the low-energy flooding electrons are somewhat directed towards the area where the X-rays are incident (1 or 2 V electrons are not easily highly focused). Both ion and electron neutralizers are tuned by optimizing ion and electron beam focus and driving parameters that result in their convergence at the focal point of the X-rays and the analyser [25].

The combination has been demonstrated to offer a high degree of flexibility and accuracy in compensating for surface charge. Obviously, the ability to tune the potential scale offers a way to mitigate static charges accumulated on insulator surfaces or from stray electrons in the chamber, and addresses the lateral inhomogeneity of the surface

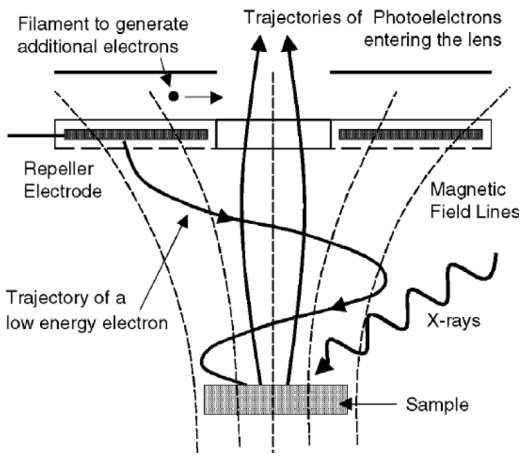

Fig. 7. Trajectories of electrons emerging from a sample immersed in the magnetic field of a snorkel lens. A low-energy electron spirals up the magnetic field line and is reflected from an electrostatic mirror held at a negative potential. The reflected electron returns to the sample surface along the same field line, thus achieving charge compensation. A filament located above the electrostatic mirror provides a small electron current to compensate for photoelectrons entering the lens. These drift across the aperture and, when they intercept the field lines, are attracted down to the surface [22].

potential when using a highly focused X-ray source [22]. In the dual-mode flood source, with reference to Fig. 9 (adopted by Edwards et al. [44]), electrons and argon ions are created in a single source. Electrons generated by thermionic emission (Region 1) are accelerated into a region of argon gas, where they collide with the gas to create argon ions (Region 2). These latter are then accelerated with the electrons towards Region 3, where both beams are then focused onto the sample surface. With this type of combination source, if the flux of electrons is varied, then the flux of ions will also be affected. Moreover, by tuning the various electrical potentials in Regions 1 to 3, it is also possible to vary the relative amounts of electrons and ions in the final combined beam for compensation. There may be multiple sets of parameters that produce excellent data, as better described in Ref. [44]. Edwards et al. developed a set of operating conditions, including reduction of the extractor voltage, that reduced the impact potential of electrons interacting with the ions to establish a condition that was effective at neutralization but minimized damage to highly sensitive samples.

One way to verify that sample charging indeed takes place, and to prevent any misunderstanding with alternative explanations of core-level shifts, is to monitor the binding energy changes as a function of X-ray power. Commonly, the peak height, width, and shape are monitored while adjusting the charge neutralizer parameters to determine the best set of conditions to use. Ideally, the parameters that produce the narrowest peaks are used, and often data are acquired under a number of charge neutralizer conditions to determine the best parameters. The shape of C 1s peak remains a useful indicator of the presence or absence of significant surface charging and the adequacy of charge neutralization on many types of insulating samples. Fig. 10 shows the C 1s peak acquired with different charge neutralizer conditions. After charge neutralizer conditions had been optimized and the effects of charging had been eliminated, a well resolved C 1s line is observed Fig. 10 (a), on the other hand Fig. 10 (b) illustrates how peak broadening and peak shoulders can be observed when samples are not properly neutralized. In the case of Fig. 10 (b), if the users assumed that the sample was not charging, they would likely conclude that there were multiple types of carbon present in the sample. Obviously, care must be taken when interpreting data, especially when charging is suspected, and often data from other elements in the same sample are also consulted to determine if charging has been eliminated. Since it is impossible to achieve 100% charge neutralization with these systems, as the best scenario is obtained, i.e., an equilibrium state is achieved, all spectral peaks are shifted by a constant, stable value and the peak shapes themselves remain unaffected. In that case, one simply needs to correct the binding energy scale by a constant value using an internal reference. As the charging state of a specimen is not known a priori, the phenomenon often leads to problems with correct BE referencing.

3.2. Binding energy reference in XPS

The procedure of charge-compensation is necessary for non-conducting samples, allowing for spectral acquisition, however it does not guarantee that the surface is electrically neutral, i.e., under or over-compensation typically takes place, hence the surface potential remains unknown. It is thus necessary to find a means for estimating the amount by which core-level peaks are shifted from their neutral positions, so that the spectra can be corrected manually after the measurement is completed. Since charging is a complex process influenced by many sample properties, the assumption of a simple BE correction is generally only an approximation. A variety of methods have been used to determine the amount of energy shift (Δ_{corr}) that needs to be applied to correct the BE scale for insulating materials. In general, but certainly not always, the entire spectrum will be uniformly displaced so that Δ_{corr} is a uniform correction to the energy scale across the spectrum. Obviously, the method for energy calibration should always be reported in the experimental section of a paper containing XPS data so that other researchers can make peak position comparisons.

Different approaches have been tried over the years to determine absolute BEs from insulating samples. Several common approaches are listed and briefly described below. Each of them has potential applications but also limitations. The most common method used for BE reference (the adventitious carbon) is more deeply described below.

3.2.1. Adventitious carbon referencing

This method relies on the use of the C 1s spectra of adventitious carbon (AdC) present on essentially all surfaces exposed to the environmental air [26]. Since it is present on all samples, these contamination layers can be used for referencing purposes. It is usually assumed that the C 1s level of this contamination would have a binding energy in the range of 284.6–285.0 eV and that the Δ_{corr} can be determined from the measured peak and applied as a constant shift to all other peaks in the spectrum. This reference energy is based on the assumption that the carbon is in the form of a hydrocarbon or graphite and that other carbon species are either not present or can be distinguished from this peak. Moreover, it is implicitly assumed that the electrical potential in the AdC layer is the same as in the actual specimen it accumulates on, hence the fact that AdC is external to the analysed sample is neglected.

3.2.2. Internal referencing

This method takes advantage from the specimens of such nature that a portion of it has spectral lines of known binding energy that can be used as the charge reference (see Ref. [26] and references). In this case one assumes the invariance of the binding energy of the chosen chemical group in different molecules. If carbon is used, the technique is called internal carbon referencing. In many circumstances, the oxygen 1s photoelectron peak is useful as a reference.

3.2.3. Substrate referencing

For studies involving thin films on conducting substrates, for which the film is thin enough such that peaks from both the film and the substrate can be measured, the observed binding energies of the substrate may provide a suitable reference for thin overlayers [26]. Often, this approach is applied without the application of a charge neutralization method (Ref. [25] and references).

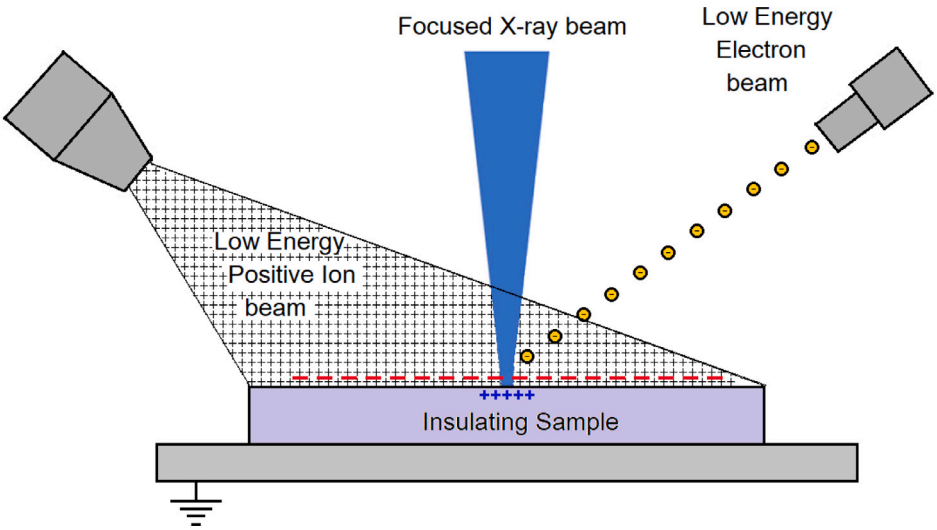

Fig. 8. Charge compensation through the use of simultaneous low-energy ion and low-energy electron bombardment of the sample surface [25].

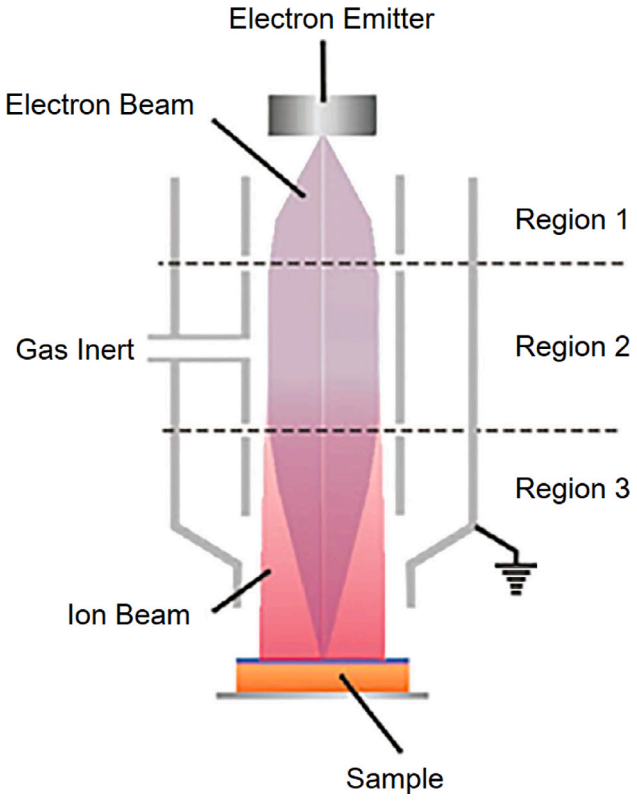

Fig. 9. Schematic showing the combined dual-mode charge compensation flood. *Source:* Adopted by Edwards et al. [44].

3.2.4. Gold deposition

A thin metal layer (0.5 to 0.7 nm) deposited on a sample or metal particles directly or indirectly deposited on a sample has been used to provide a signal with known BE for a charge reference. This layer is also connected to the spectrometer by mechanical contact with the sample holder, providing both an electrical pathway and BE reference, so that both the spectrometer and the layer are at the same electrical potential. Although in some cases the use of Au as a BE reference produced consistent results, it does not necessarily provide an accurate BE Ref. [45]. It has been found that the BE of Au atoms depends on the size of Au clusters formed after deposition [46,47]. Moreover, Au referencing has significant problems that include substrate interactions, and surface coverage effects [40,48,49]. Au referencing can still be effective for some applications (see Ref. [50] and references), however, due to the many limits reported in its application, this method is no longer widely used for XPS measurements. For more details see Ref. [26] and references.

3.2.5. Implantation with inert gases

Another attempt to solve the BE reference problem is based on the use of core-level lines of implanted inert gas atoms [51,52]. With an incident energy in the range 1–5 keV, the implantation depth largely overlaps with the XPS probing depth. In contrast to the technique based on noble metal deposition, there is no risk for attenuation of the specimen signals. However, such implantation may change the chemistry of the specimen and induce binding energy shifts in the sample. It has also been demonstrated that measured binding energies for an implant species can vary in different matrices because of varying relaxation effects [51]. This approach is used, especially, after sputtering during depth profiling, and it will be discussed in more detail in Section 4.2.

3.2.6. Referencing to the C 1s peak of AdC - Fundamental limitations

The use of AdC for BE referencing has been introduced by Siegbahn and co-workers [3] in the early days of X-ray photoelectron. The technique is by far the most common method for calibration of the BE scale. Although the use of AdC for referencing remains important and useful for a variety of purposes, referencing spectra using AdC has intrinsic fundamental limitations for use as an absolute BE for both conducting and insulating materials.

A significant disadvantage of this method lies in the uncertainty of the true nature of the carbon and the appropriate reference values [26,40]. The ISO 19318:2004 and ASTM E1523-15 guides recommend setting the C–C/C–H component of the measured C 1s spectrum of AdC at 284.6 to 285.0 eV and applying a corresponding shift to all other spectra. In addition, it is recommended that the reference binding energy should be determined on the user's own spectrometer, and that the measurement should be carried out on a substrate similar in its chemical and physical properties to the material to be analysed and covered by only a thin, uniform contamination layer, that is, of the order of a monolayer [26]. Both charge-referencing guides list important conditions upon which the specified BE range is valid. As mentioned before, it is assumed that the carbon is in the form of a hydrocarbon or graphite, and it is taken into account that the carbon binding energy may also shift as a consequence of ion sputtering [40]. Limitations regarding the accuracy of the use of C 1s for BE referencing

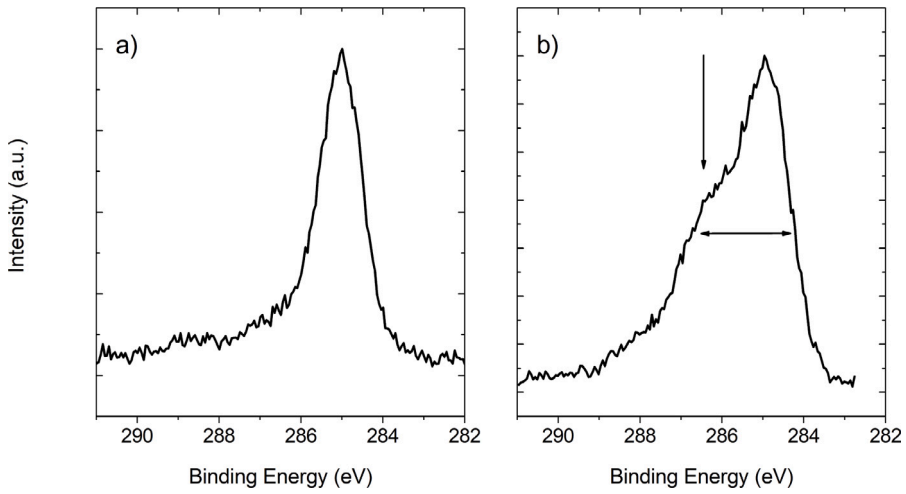

Fig. 10. C 1s narrow-range spectrum acquired with different charge neutralizer conditions. (a) After charge neutralizer conditions had been optimized, and (b) when sample is not properly neutralized: the two arrows indicate the broadening and the shoulder of the peak.

have been pointed out in several papers over the years (for an historical perspective, see Ref. [50]). The main criticism of this technique includes:

(a) The unclear chemical nature of AdC, [53,54]. The monitoring of the FWHM [26] is crucial to distinguishing the presence of more than one type of carbon. As an example, Barr et al. [55] explicitly addresses the nature of AdC, offering very relevant and original comments. The authors pointed out that AdC species are typically not chemically reacting with the underlying substrates, hence the process of AdC deposition can be classified as physisorption.

(b) The lack of a well-defined single energy value associated with the C 1s peak of AdC (Ref. [50] and references).

(c) Differences in the methodology of the BE scale correction. This discrepancy contradicts the notion of a BE reference, originally intended to be represented by one single value of 285.0 eV [3], and adds to the large spread of reported BE values for the same chemical species. The extent and popularity of this method contrasts with the documented examples of associated problems reported over the years where C 1s referencing leads to inconsistent results [48,56,57]. Swift [56] conducted an interesting study on a wide range of conducting material, demonstrating that the chemical nature of an AdC layer varies with the substrate type, and that it is not an inherent property of the AdC layer alone: thus the substrate influence is decisive, as well as the environment it has been exposed to, and the exposure time [15,58]. For this reason the author concluded with an explicit warning, inviting to take special care with the interpretation of binding energy data.

(d) The lack of understanding when other correction methods could make a correction employing AdC unnecessary.

To address these issues, authors are encouraged to indicate more information that would help to understand the type of AdC species present at the surface of their samples and how this information was used for BE referencing. Such convention would also facilitate inter-laboratory comparisons of chemical-state information.

3.3. Auger parameter analysis

Auger parameter analysis is a useful method to analyse the chemical state in X-ray photoelectron spectroscopy because it is not necessary to take the charging effect into account for the analysis of nonconductive materials, especially for the simple material systems of a single chemical state. Auger spectra have unique peak shapes and positions and are particularly useful for both elemental identification and chemical state analyses.

The Auger parameter, α, first described by Wagner [59] can be measured for any element as long as one photoelectron signal and one Auger electron signal for that element can be observed. This parameter can be used without interference of surface charging. It is defined as:

$$\alpha = KE(A) - KE(P), \tag{11}$$

where $KE(A)$ is the kinetic energy of the Auger transition and $KE(P)$ is the kinetic energy of the photoelectron from core level for the same element. This form of the equation allowed for negative values of α. Rewriting Eq. (11) in terms of binding energy, and adding the photon energy, hν, in order to keep the Auger parameter positive and independent of the photon energy used to collect the spectrum, one arrives at the modified Auger parameter α' [60]:

$$\alpha' = \alpha + h\nu = KE(A) + BE(P), \tag{12}$$

where $BE(P)$ is the binding energy of the photoelectron core level. Since any surface charging shifts will be of the same magnitude, but of opposite direction in each of these two components, they will be automatically cancelled out in α'. The use of the modified Auger parameter α' is particularly useful in case of nonconducting samples, overcoming most of the troubles related to the surface charging.

Arranging the photoelectron binding energies (abscissa, oriented in the negative direction) and Auger kinetic energies (ordinate) on a two-dimensional plot, known as a Wagner plot or chemical state plot, allows more accurate delineation of the characteristics of a chemical state, specifically since the chemical shift of the Auger lines in these elements are different from, and often greater than, those of photoelectron lines. Eq. (12) shows that the Auger parameters are the intercepts of the linear relationship $KE(A)$ vs. $BE(P)$ to be read directly on the straight lines with slope −1. This value is independent of the charge referencing operation, and therefore is found with higher accuracy than the determination of either line energy alone. Hence, the modified Auger parameter can be used in addition to the binding energy to give additional insight into the shift in electronic state.

Castle and West [61] have shown that it is possible with conventional instruments (i.e., equipped with non-monochromatic source) to use the bremsstrahlung component of the X-ray radiation to generate the KLL Auger lines of aluminium and silicon. With a beryllium X-ray window these $KL_{23}L_{23}\left(^1D_2\right)$ Auger lines are ~20% as intense as the 2p photoelectron line, and of the same width, within ~0.2 eV. Otherwise, the more energetic Ag L_α X-ray source offers a wide range of new electron signals, especially in the extension of the accessible 1s core levels from Al to Cl [62]. Furthermore, Ag L_α X-rays can be monochromatized by the same monochromator geometry as Al K_α X-rays.

For silicate glasses, the Si Auger parameter depends on the structure and the concentrations of other cations in the matrix. Consequently,

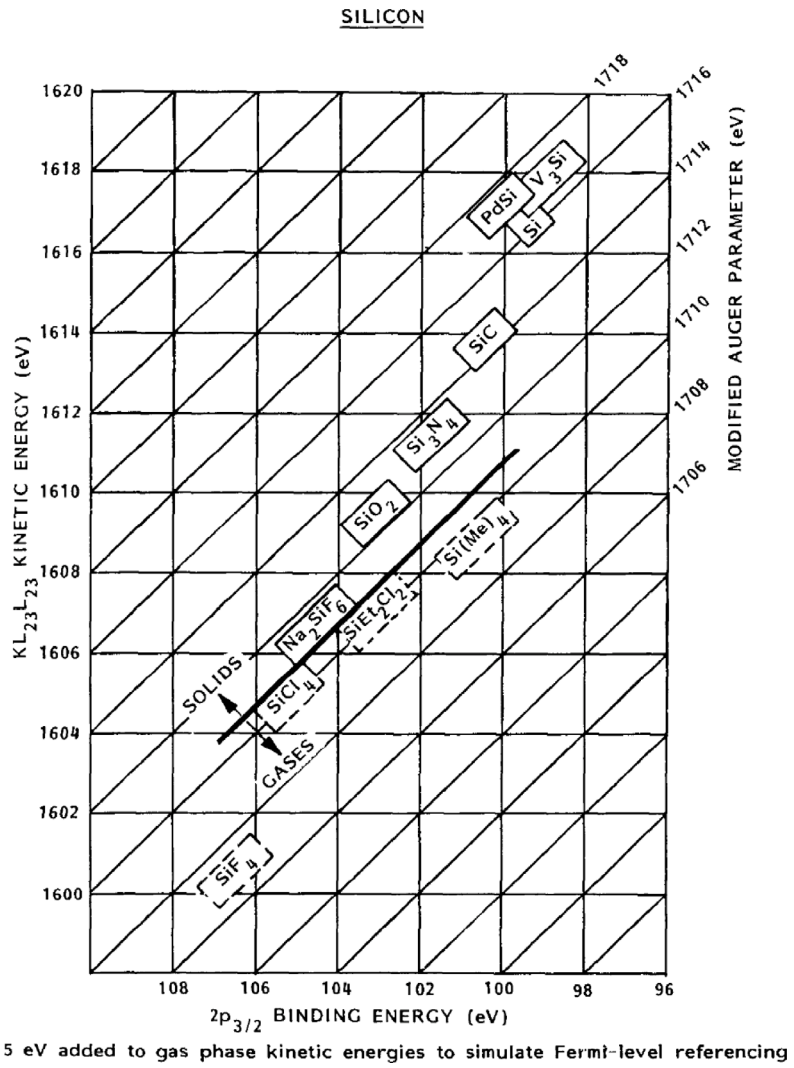

Fig. 11. Chemical state plot of silicon compounds [63].

the Si Auger parameter is an excellent indicator of the chemical nature of the surface structure associated with Si. The basic Wagner plot for silicon is shown in Fig. 11. The data points are usually arranged in rectangular boxes parallel to the grid lines to indicate that the greater error resulting from charge referencing introduces uncertainty in the direction of the grid lines and not across them. The different values of the Auger parameter depend on the chemical species. This parameter allows to discriminate among chemical compounds that could give rise to the same BE in the photoelectronic peak.

4. Depth-profiling strategies

XPS can provide compositional information about the outermost monolayers of solid materials with a surface sensitivity of the order 0.5–5.0 nm. Using angle-resolved X-ray photoelectron spectroscopy (ARXPS) it is possible to probe subsurface chemical states, thus decreasing the sampling depth simply by using a suitable sample geometry. For compositions which vary on the order of several tens of nm, it is common to use the ion sputtering technique [64], which removes in a controlled way the first layers of the sample surface providing reliable results with depth resolutions as good as 1–2 nm in some cases. For depths less than about 3 nm, the changes that occur during the establishment of the steady state in the sputtering process make that approach increasingly inaccurate [65]. Additional details on the depth profiles strategies are given in the next subsections.

4.1. Angle-resolved XPS

Angle-resolved XPS can achieve greater surface sensitivity on relatively flat samples by simply changing the orientation of the detector to the sample surface normal (ψ), referred to as the angle of emission. The technique relies upon the fact that spectra recorded at n emission angles $\psi_1, \psi_2, \psi_3, \ldots, \psi_n$ will therefore contain information on the concentration depth profile of each element present. When the sample is untilted, as in Fig. 12 (a) ($\theta = 90°$), the escape depth and the sampling depth are the same. When the sample is tilted, as in Fig. 12 (b) ($\theta = 30°$), the escape depth does not change since this is a physical parameter defined by the electron energies and the material they are travelling through. However, the path to reach the detector does change, and consequently, the sampling depth is reduced. Thereby, a larger angle of emission enhances the signal from the surface. Thus, analysis at several angles can provide a non-destructive "depth profile" [66,67]. By combining the ARXPS data set with suitable software it is possible to use this method to produce shallow concentration depth profiles in the range 0–5 nm, down to a depth limit of perhaps a few times the attenuation length. The models typically used in the treatment of ARXPS data apply the Beer–Lambert law for the measurement of layer thickness, assuming a flat sample surface, and flat layered samples that are homogeneous within each layer. Samples exhibiting surface roughness will exhibit different electron angles of emission and shadowing effects. These latter can be accounted for and modelled, but they complicate the analysis

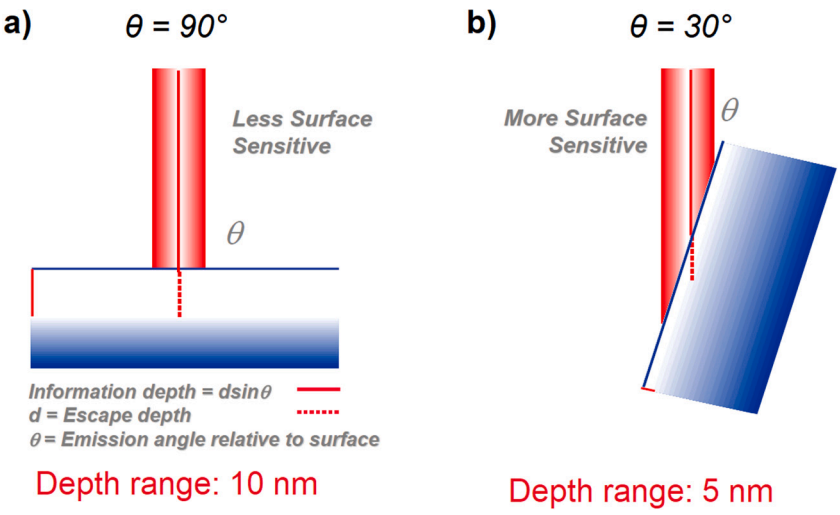

Fig. 12. Tilting the sample is an easy way to change the depth of analysis in XPS. While the escape depth is constant in both (a) and (b), tilting the sample increases the angle of emission, θ, and results in a smaller information depth.

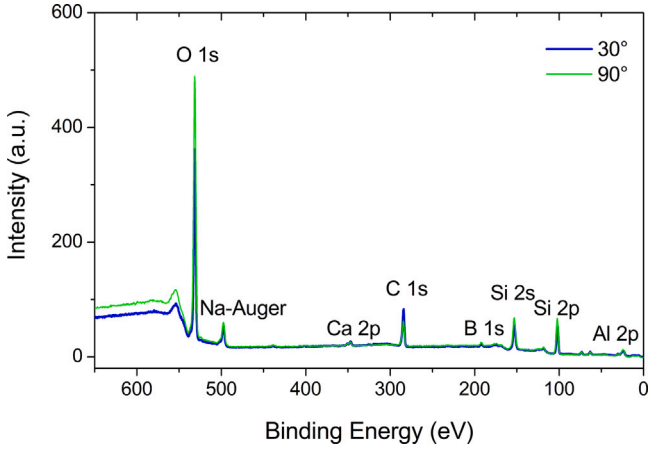

Fig. 13. Survey spectra of borosilicate glass taken at photoelectron take-off angles of 30° (blue line) and 90° (green line), respectively. (For interpretation of the references to colour in this figure legend, the reader is referred to the web version of this article.)

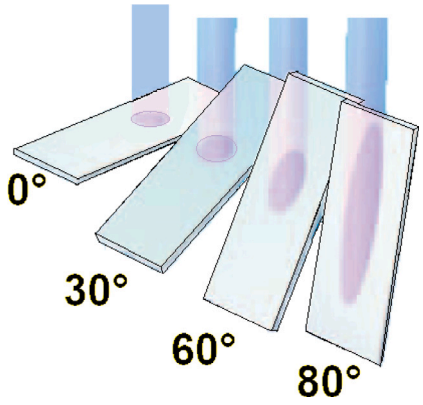

Fig. 14. The analysis area changes as a function of angle, especially when using lens-defined small area analysis [9].

and often require software programs to extract reliable information (Ref. [5] and references).

Fig. 13 shows an example of the information this approach can provide. The original data, taken at 90°, do not indicate if carbon contamination is a homogeneous layer. Comparison of the data at 90° with that at 30° shows a difference in the relative intensity of C 1s and Si 2p. When a thinner layer of the surface is probed during the experiment at 30°, the carbon component is higher in intensity, indicating that AdC is indeed a surface layer on top of glass surface. If it was a homogeneous mixture, the relative ratio of the two components should not change upon tilting the sample.

Modern spectrometers can provide angle-resolved data collected over a 60° range of angles in parallel, without the need to tilt the sample. This is accomplished using the angle resolving lens and a 2D detector [9,68]. Using parallel acquisition of angular data without tilting the sample has a number of advantages:

(1) ARXPS can be applied to large samples. It would be difficult to tilt a large sample in a conventional XPS system, especially if data is required from a region near the edge of the sample.

(2) The analysis area changes as a function of angle, as can be seen in Fig. 14. A worst case occurs when the transfer lens is used to define the analysis area. Using parallel angle acquisition, the analysis area and position is completely independent of the emission angle.

(3) If an insulating sample is tilted, the required charge compensation conditions also change, thus efficiency. Using parallel acquisition of angular data, the compensation conditions are the same for all angles and any changes in the spectra as a function of angle must reflect real chemical differences.

4.2. Sputtering

XPS systems are commonly equipped with some type of sputtering gun to physically remove material from the sample, thus allowing to probe deeper into the sample. During a depth profiling, repetitive cycles of sputtering, followed by XPS analysis, provide a composition depth profile analysis. This procedure is repeated until the sputtering has probed to the depth of interest. Some sputtering experiments will probe hundreds of nanometres to micrometres into a sample and may take many hours to perform. Depending on the structure and composition of the analysed materials (original surface roughness, crystalline structure and defects, alloys, compounds, etc.), several factors affecting depth profile may come into play, from instrumental factors to ion-induced effects: among them, the impurity in ion beam, the time-dependent intensity of the ion beam, the redeposition of sputtered species, atomic mixing. However, the most important factor influencing the XPS analysis is the so-called “preferential sputtering” and the consequent decomposition of compounds. The preferential sputtering of the light elements is a normal ballistic (kinetic) effect taking place

during sputtering: in the frame of an XPS analysis, it can induce an undesirable change in the composition of the sample under analysis (and then in the chemical bonds among their atoms), thus inducing artificially the formation of new compounds do not present in origin in the sample itself. In general, a great care must be done with the procedure of depth profile by using ion beam.

As far as the depth profile analysis of glass surface is concerned, it has been carried out to investigate the diffusivities of mobile ions and the chemical durability of glass [69,70]. For this reason, information about depth profiles is helpful to investigate the mechanism of leaching process and to estimate the leaching behaviour [71]. More in details, the interaction between conventional, i.e., monoatomic ion beams and solid glass surfaces is a rather complex process [72]. It involves the formation of a rearranged surface layer with a modified composition and modified bonding, structural damage, and high gradients of mechanical stresses [73]. The composition variation stem mainly from preferential sputtering, radiation enhanced diffusion, internal electric field formation and ion implantation of primary ion beam species. After the ion bombardment, an enrichment or a depletion of the network modifier elements on the glass surface can be observed [74,75]. Therefore, the real surface-related properties of the glasses under investigation, particularly their natural surface composition and bonding, can be masked by the sputter-induced artefacts.

Successful profiling, without significant sputter-induced spurious results, depends on the combination of the ion beam used and the type of sample material (Ref. [8] and references). For example, sputtering samples without damaging them is almost impossible with an Ar^+ sputter ion gun. Historically, Ar^+ has been the most commonly available sputtering source [5]. Unfortunately, such sputter treatment is not completely "inert" [75]: the ion bombardment causes the loss of material but at the same time can also change composition and structure of the analysed region. The effect of Ar^+ ion sputtering on the surface composition has been known for some glasses [74,75]. If account is not taken of these changes, misleading conclusions of the surface spectra can result. Many efforts have been devoted to contain the formation of altered surface layers. More gentle ion sources including C_{60}^+ (buckminsterfullerene) and argon clusters have been developed: these sources are able to more successfully sputter many types of samples without changing the characteristics of the sample under investigation.

The following subsections describe the impact of monoatomic Ar^+ ion and Ar/C_{60} cluster sputtering, respectively, on a wide family of silicate glasses.

4.2.1. Monoatomic ion beam

Certain care needs to be used when sputtering samples with Ar^+ ions, since they physically damage the sample in a partly uncontrolled manner. Some atoms are more likely to be ejected than others, a process known as differential sputtering, and this can cause a difference between the measured atomic ratios compared to the actual atomic ratios in the original sample. Furthermore, the interaction between the ions and the sample can change the chemical state of the latter. For example, Smets and Lommen [74] reported an XPS study of the changes in the surface compositions and structures on silicate glasses. They showed that a rather gentle (4 keV, 5 μA cm^{-2}, 5–10 min) Ar^+ bombardment produced significant changes in the sodium concentration and non-bridging to bridging oxygen ratio at the surface of a binary sodium-silicate glass. They also showed that preferential sputtering of constituent oxides could occur, affecting the surface compositions of bombarded multicomponent glasses.

Brow [75] conducted an XPS study on phosphate glasses, outlining that sputtering of silicate glasses resulted in a depletion of the sodium concentration to a depth of 9 nm. Here, the loss of sodium is attributed to electric field-induced migration. In contrast to silicate glasses, phosphate glasses showed a depletion of phosphorous accompanied by an enrichment of sodium in the surface region. This observation is ascribed to the difference in surface binding energy of the two species. From a thermodynamic point of view, the P–O bond is weaker than the Na–O bond and hence P is expected to be removed at a greater rate than sodium. After sputtering the surface can be enriched by sodium.

Ar^+ ion sputtering is known to be inadequate for quantitative analysis of glass containing mobile ions such as soda–lime–silica glass. Yamamoto et al. [76] conducted an interesting XPS study aimed to elucidate the limits encountered during depth profile analysis employing Ar^+ ion gun. In their study, the profile mutation in soda–lime silica glass was investigated on the dependence of the accelerating voltage at 2 and 4 kV for Ar^+ ion sputtering. They found that the higher accelerating voltage induced the more migration of mobile ions due to the further implantation of Ar^+ ion into the glass surface. Furthermore, the authors utilize C_{60} ion sputtering for the detailed examination of the surface states after Ar^+ ion sputtering carried out at both conditions mentioned before. As a result, it was firstly confirmed using C_{60} ion sputtering that the higher accelerating voltage caused the deeper implantation of the Ar ion and the larger migration of mobile ions. Despite these evident limits, the authors recognize to the Ar^+ ion sputtering the merit that it is still a convenient method because of the small beam size, the wide range of the sputtering rate, and the low running cost.

4.2.2. Gas cluster ion beams

More gentle gas cluster ion sources have recently been developed and used, these sources are able to more successfully sputter many types of samples without damage [77]. Gas cluster ion beams (GCIBs) are generated by an adiabatic expansion of the working gas in a nozzle, moving from the high-pressure side to a vacuum chamber [78,79]. Here, after cooling, the atoms or molecules are merged to clusters of various dimensions [80]. They are then ionized, separated, accelerated and formed by ion optics into a well-defined ion beam. When multiatomic or molecular ion clusters collide with solid surfaces produce impact effects differing from those induced by conventional ion beams. For example, the dependence of cluster stopping on momentum was found to be totally different than for monoatomic projectiles, where the dependence is linearly scaled with energy [81].

For a large number of atoms in clusters the energy per atom may be rather low, even in the range of a few eV. Since the constituent atoms in clusters are mutually weakly bonded, the clusters disintegrate during impact upon a solid target and do not penetrate deeply underneath the surface [82]: despite this, they can be still used for surface cleaning and for shallow concentration depth profiling. Considering that Ar does not react with atoms on solid surfaces and practically no argon atoms are left on the surface [79,80,82,83], Ar is one of the most frequently used working gases for generating cluster ion beams. With respect to conventional Ar^+ ion beams, Ar cluster ion beam results in a high sputtering yield per one cluster ion, enhanced lateral sputtering effects, low-level surface roughness, and by substantially reduced surface structure damage (Ref. [73] and references)

The principal gas cluster ion beam advantage is the ability of selecting the impact energy E, and the cluster size N. As mentioned above, the average kinetic energy per atom is much lower than for the monatomic ions used previously, leading to greatly reduced damage in sputter depth-profiling. In contrast to sputtering with monatomic ions, the average energy per atom in gas cluster sputtering is comparable to typical covalent bond energies, i.e., of the order of 1 eV. The GCIB sources produce ionized argon clusters having a size distribution ranging from around 500 to 5000 atoms. Thus, since gas cluster ions cause less damage to the near-surface layer, GCIB is efficiently applied also to XPS depth profiling of energy-sensitive organic materials [84]. Actually, recent studies have shown that argon cluster can be more useful than conventional monoatomic argon ions for surface diagnostics (Ref. [84] and references).

Korobeishchikov et al. [84] conducted an interesting study on the sputtering yields of silicon dioxide with the aim to elucidate the relation

of the normalized yield versus normalized primary ion energy in a cluster at 0° and 45° angles of ion beam incidence. These angles were chosen because the surface treatment is generally conducted with the primary cluster ions impacts at normal incidence, whilst the surface analysis is typically performed with the oblique beam incidence. In addition, according to Refs. [84–86], the sputtering yields differ maximally at normal incidence and the incidence angle of 45°. Korobeishchikov et al. set the kinetic energy of the primary cluster ions in the range of E = 5–23.5 keV, while the mean cluster size was N_{mean} = 100–1000 atom/cluster. The authors found that, when the energy per cluster atom quantity E/N is comparable to the binding energy of the solid (few eV), the yields of atoms sputtered per primary atom Y/N, at the incident angle 45°, is 4 times greater than at normal incidence. Conversely, when energy E/N is significantly above the binding energy of the solid (~100 eV), the angle of incidence ceases to influence the sputtering yield value. For a given cluster size the sputtering yield Y increases as the primary energy increases: slowly at the normal incidence and more rapidly at the oblique incident angle.

In another significant study, Zemek and co-workers [73] investigate lead-silicate glass surfaces with the use of high-energy resolved X-ray induced photoelectron spectroscopy before and after argon cluster ion beam sputtering. Focus is placed on possible changes in surface composition and in chemical bonding. It was found that the results of XPS analysis are qualitatively influenced by the surface contamination present on air-exposed lead-silicate glass surfaces. Specifically, in contrast to the sputter-cleaned surfaces, X-ray irradiated air-exposed lead-silicate glass surfaces reveal different dependences of the surface composition and oxygen bonding on irradiation time. This effect is related to carbon-bearing species lying on the top surface, in particular with C–O and C=O functional groups.

Furthermore, Ar cluster ion beam sputter-cleaning with mean energy per Ar atom in clusters of a few eV was successfully used to remove surface contamination from air-exposed lead-silicate glass with no substantial modification of the glass surface structure. The bridging oxygen (BO) fraction measured in this work for Ar cluster ion beam sputtered surfaces is in good agreement with the BO fraction for the lead-silicate glass surfaces, having approximately the same composition, created by fracturing in UHV conditions [87]. The present results clearly show that surface cleanliness of lead-silicate glass is the critical point in surface-related research.

Unlike Ar ions, C_{60} ions do not knock with but stick atoms away from the surface [88]. Considering that one C_{60} molecule has 60 carbon atoms and collapses when it encounters the surface, the energy in one molecule is shared among the 60 carbon atoms. Each carbon atom possesses much lower energy than an Ar ion under normal sputtering condition. For example, a 5 kV C_{60} ion means less than 0.1 kV for each carbon ion. This value is much lower than a 0.5 kV Ar ion which is the threshold for sputtering effect. Yamamoto and Yamamoto [89] propose a comparison between the concentration depth profiles acquired from photoelectron core level spectra of soda–lime–silica glass using monoatomic Ar and C_{60} ion beam sputtering. Probably, it is the first time that C_{60} ion beam has been applied to analyse the distribution of sodium ion in a soda–lime–silica glass. When the classical Ar ion beam was applied, the glass surface was found to be sodium depleted, but when the C_{60} ion beam was used the sodium concentration showed up to be constant, dose-independent, and close to the value expected for bulk glass composition. XPS depth analysis with C_{60} ion sputtering is confirmed as one of the most suitable techniques to analyse the surface of alkali glasses with the depth resolution of less than 2 nm. Unfortunately, the authors provided no information about chemical bonding at the analysed surfaces, which can be more sensitive than compositional changes to ion beam–glass surface interactions [89].

Yamamoto [90] reported a precise XPS depth analysis where C_{60} ion sputtering was utilized to clarify the variation of sodium depth profile at the near-surface region of soda–lime–silica glass after various treatments such as annealing, washing, polishing, and storage. The analysis reveals that the sodium profile changes differently within 30 nm depth depending on each treatment. As a result, it was found that the behaviour of sodium profile almost reflects the ion exchange reaction with proton (see Section 6.1.2). Furthermore, the difference of sodium profile is also confirmed because of the reaction with liquid (wash and polish) and vapour of water (storage). The latter results demonstrate the relevance of this technique in the leaching mechanism investigation.

4.2.3. Charge neutralization and charge referencing during sputter depth profiles

Since sample properties may vary during a depth profile, knowing that charge neutralization is working well for the whole profile becomes crucial. Differential charging can be introduced by the ion sputter beam, in addition: as described before, samples are often modified by reduction or alteration by the sputtering process, such as differential sputtering, sputter rates variation, ion beam-induced chemistry. Usually, XPS measurements are collected between increments of sputtering, but data can be acquired on a continuous basis while sputtering in some condition. The standard XPS charge neutralization mode, described above, could be successfully used again, and the consistency of peak shape and lack of peak shifting during the profile could be used as an evidence that sample charging does not vary during the depth profile.

Charge referencing of insulating materials is a continuous challenge [45], especially if argon sputtering is carried out to remove contaminations or a native oxide layer from the surface, removing at the same time adventitious carbon that could be used as an energy reference alternatively. Thus, the choice of a reliable charge reference in the XPS analysis of insulator materials after sputtering is indeed a delicate issue. One possible solution is to use core-level lines of implanted noble gas atoms [51,52]. This charge referencing method was recommended by Bertóti [52] for the referencing of spectra recorded after sputter cleaning or during depth profiling of nitride coatings. With an incident energy in the range 1–5 keV, the implantation depth coincides with the XPS probing depth making this approach particularly interesting.

In contrast to the technique based on noble metal deposition [45], there is no risk for attenuation of the specimen signals. This approach, however, has limitations, as demonstrated by Pélisson-Schecker et al. [45]. They used XPS to analyse a series of Al–Si–N samples deposited by magnetron sputtering. The authors found that the BE of the Ar $2p_{3/2}$ peak for implanted Ar atoms shifts with varying Si content with respect to that of Au $4f_{7/2}$ peaks from deposited Au clusters by as much as 1 eV, which is associated with a marked rise in the concentration of trapped Ar atoms. They showed that gold atoms redeposited onto the surface facilitate a reliable evaluation of the relative chemical alterations of elements in Al–Si–N samples. This kind of effect can be explained considering that conductivity in the phase where Ar is being implanted may be a function of the Ar concentration. The actual implantation of Ar can also give rise to forward sputtering and Frenkel pair formation [50], where the resulting lattice point defects may influence the bonding signatures of the studied material. In any case, this example shows that the noble character of implanted atoms does not guarantee constant binding energy of the associated core-level peaks, hence they cannot be used as a reliable reference for BE.

5. Structural, chemical and bonding analysis of network glasses

X-ray photoelectron spectroscopy has become a precious tool over the last 50 years for studying mainly the surface properties and reactivity of a wide range of materials. The recent enhancement in charge compensation methods for XPS has allowed for the collection of high-resolution spectra and chemical state information of insulators. Line widths for non-conductors, comparable to those of semi-conductors, can now be acquired regularly [91]. Therefore, XPS proved to be an

invaluable instrument for the study of non-conducting materials, such as glasses. In particular, a large number of XPS studies have been performed over the last few years, predominantly to characterize the glass composition and to obtain structural information.

After a brief introduction on the main structural properties of network glasses, the most significant XPS studies conducted on silicate and borosilicate glasses will be introduced.

5.1. Glass compositions and structures

A fundamental understanding of the atomic structure of glasses and their interactions with the environment plays a critical role in improving and optimizing many glass properties such as optical transmission, mechanical strength, electrical conductivity, corrosion and chemical durability.

Two main groups will be considered below, namely silicate and borate glasses. Silicate glasses have been used in a wide range of areas for hundreds of years. The study of the molecular structure of vitreous silica (SiO_2) has been fundamental to understand the structure of other silicates. For what concerns structure and properties of borate glasses, instead, these latter are quite different from the silicates. Boron trioxide glass (B_2O_3) is normally not useful for any application in the pure form because of its very low chemical durability and high affinity for water. However, borate glasses are getting increased attention because of their unique qualities, indeed, boric oxide is used extensively in borosilicate glasses. These glasses have higher chemical durability, thermal shock resistance, and electrical resistivities, thus allowing a broad range of industrial applications. Therefore, compositions and relative structural properties of some of the most commonly used silicate and borate glasses are briefly summarized below.

Silica glass. One of the simplest glass structure is probably that of silica glass. The latter consists of slightly distorted SiO_4 tetrahedra linked to each other at corners. The basic unit is shown in Fig. 15 (a). Each oxygen acts as a bridge between neighbouring tetrahedra, and hence is called bridging oxygen (BO) [92].

Boric oxide glass. The boron ion is a glass former. In B_2O_3 glass, the basic structural unit is a BO_3 triangle, since the oxygen coordination around each B is only 3. It is commonly believed that B is slightly above the plane of the three oxygens. All the oxygens are bridging between neighbouring triangles. Moreover, it is widely assumed that the basic building block on the boric oxide glass is the boroxol group shown in Fig. 15 (b).

Alkali silicate glasses. The alkali metals (e.g., M=Li, Na, K) are termed network modifiers, because these ions take up random positions in the network and thus "modify" or change the structure of the network. They enter the glass as singly charged cations and occupy interstitial sites. Network modifiers break the Si–O–Si bond by forming non-bridging oxygen (NBO) and attaching an oxygen provided by the alkali oxide, M_2O, to the broken bridge. The positive charge of the alkali unit is satisfied by an ionic bond to an oxygen, as shown by the reaction:

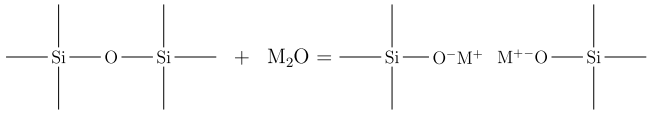

A schematic representation of an alkali silicate network is shown in Fig. 15 (c). In alkali silicate glasses, the fraction of differently bound Si species, Q_n (n = 0–4), depending on the number n of bridging oxygens bound to the quaternary silicon, is a function of stoichiometry and the M/Si ratio. Q_0 represents all NBOs (isolated SiO_4 tetrahedron), and Q_4 represents all BOs. When a NBO is created, the network reduces its connectivity, and hence mass-transport-related properties such as fluidity, diffusion, electrical conduction, and chemical corrosion increase [92].

Alkali–alkaline earth-silicate glasses. From a structural point of view, it has been proved that alkali and alkaline earth ions are often mixed randomly in the silicate network. In general, alkaline-earth ions (e.g., Mg, Ca, Ba) are bivalent, thus the addition of one alkaline earth creates two non-bridging oxygens. Alkaline-earth cations act as network modifiers just as alkali ions, but the structure of alkaline-earth glasses is more disordered than corresponding alkali glass. After the addition of alkaline earth to alkali silicates the connectivity is still maintained to a large extent, leading to a great stabilization of the glass network. As a results, the glass no longer readily dissolves in water (for more details see Section 6).

Alkali borate glasses. When an oxygen from a modifier oxide (M_2O) is introduced to boric oxide glass, two possibilities can be considered:

(a) Create a non-bridging oxygen, as in the silicate glasses, where the oxygen coordination around the boron remains three.

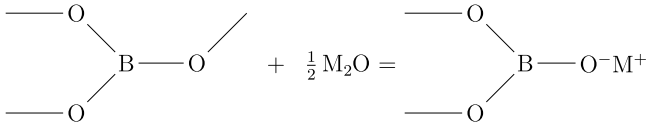

(b) Convert boron from a 3-coordination state (B_3) to a 4-coordination state (B_4).

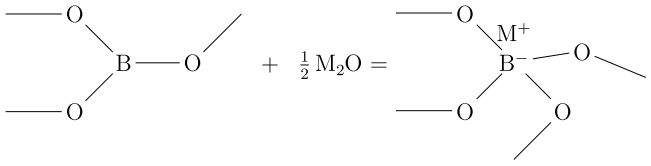

In the BO_3 group, all the oxygens are bridging, and hence one negative charge from each oxygen satisfies the three positive charges on the boron ion. After the conversion from B_3 to B_4, all the oxygens remain bridging; the extra negative charge on the $[BO_4]^-$ group is satisfied by an adjacent alkali M^+ ion. The electron transferred from the M atom is not localized between the M atom and any specific oxygen, instead it appears as a distributed charge density over a large-effective-diameter $[BO_4]$ group. Recognizing that this connection is somewhat loose, the alkali ion is expected to become more mobile. At the same time, the connectivity of the network increases, and hence flow-related properties decrease (i.e., viscosity increases) and thermal expansion decreases [92]. The conversion from the B_3 state to the B_4 state stops at around 20 mol% added alkali. No NBOs are created. Thereafter, further additions up to about 50 mol% cause the production of NBOs, thus the depolymerization of the glassy network.

Alkali borosilicate glasses. In alkali borosilicate glasses, $M_2O{\cdot}SiO_2{\cdot}B_2O_3$ there are two network formers: silicon and boron. The added alkali may link either with silicon, creating an NBO as SiO^-M^+, or with boron, presumably converting a B_3 to a B_4 and creating no NBOs in the process. Using ^{11}B NMR techniques, the concentrations of three and four-coordinated boron can be quantified.

For sodium borosilicate glasses the relative ratio between three and four coordinated borons has been predicted by a model proposed by Bray and co-workers [93,94]. They determined that the glasses were composed of the structural groupings present in the crystalline compounds associated with the glass-forming system and there are separate borate and silicate networks in the borosilicate glass.

In the structural model proposed by Dell et al. [95] for sodium borosilicate glasses, two molar ratios, R=Na_2O/B_2O_3 and K=SiO_2/B_2O_3 were introduced to characterize the glass system. According to their model, it has been shown that alkali prefers to associate with the boron as long as $R < 0.5$. The ternary system behaves just like the binary sodium borate system and all the sodium oxides goes into the borate

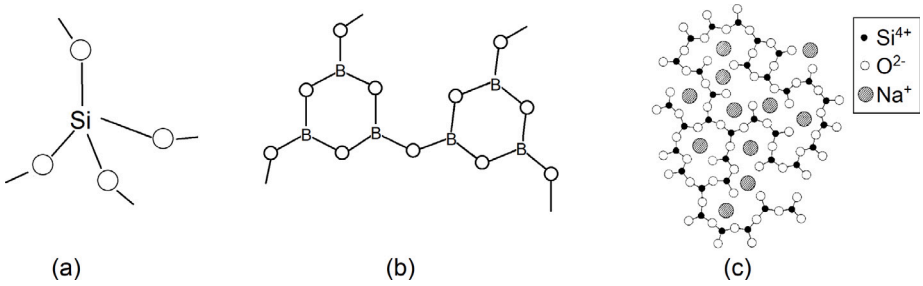

Fig. 15. (a) Basic building block for silica glass. SiO_4 tetrahedron with all four oxygens bridging between neighbouring tetrahedra. (b) Configuration of the boroxol ring in boric oxide. (c) Two-dimensional representation of the structure of sodium silicate glass. (The fourth oxygen with every Si is presumed to be out of the plane of the paper.) Note that some oxygens (bridging oxygens) are coordinated to two silicons, others to only one. In the latter case (non-bridging oxygen), a sodium ion will be found in the vicinity for charge compensation [92].

network regardless of the silica present (BO_3 units are transformed to BO_4). Thereafter, the alkali distribution is partitioned between boron and silicon, creating NBOs depending upon the *K* value. The fraction of the four coordinate boron group (N_4) increases with alkali oxide content up to $R^* = 1/2 + K/16$ [96]. For $R > R^*$ the additional alkali cations cause depolymerization of the glassy network, starting to form NBOs in the silica tetrahedrons. N_4 is almost constant in the region with $R^* < R < 1/2 + K/4 = R_1$ and then drops linearly as more alkali oxide is added. NBOs are then formed also in borate units at higher alkali contents (for $R \geq R_1$).

Although this model is still a useful starting reference for the structure evolution as alkali cations are added to the glass system, several authors have criticized it. In particular, Martens and Müller-Warmuth [97] examined sodium borosilicate glasses by ^{11}B, ^{23}Na and ^{29}Si MAS NMR and revealed that the borate and silicate networks as well as the cations were more randomly mixed to a great extent than had been assumed in the most models of borosilicate glasses [93,95,98]. For more details see Ref. [99] and references therein.

Alkali aluminosilicate glasses. In alkali-aluminosilicate glasses, the trivalent aluminium ion can act either as a network former or as a network modifier. The structural configurations depend upon the $[Al_2O_3/M_2O]$ ratio. When $[Al_2O_3/M_2O] < 1$, the Al^{3+} acts as a network former having tetrahedral coordination. Similarly to the case of the $[BO_4]$ group, the excess unit negative charge on the $[AlO_4]$ group is compensated by a nearby alkaline ion. Therefore, in this case the addition of an aluminium ion to an alkali silicate glass eliminates an NBO. At $[Al_2O_3/M_2O] = 1$, the structure contains no non-bridging oxygens. Increasing Al^{3+}, i.e., when $[Al_2O_3/M_2O] > 1$, the Al^{3+} ion acts as a network modifier in an octahedral coordination. Most likely, three of the oxygens are non-bridging and three bridging, as exemplified by Fig. 16. In order to calculate the structural configurations in the $M_2OAl_2O_3SiO_2$ glasses, first the alkali ions are associated with available Al ions. Hence, any residual alkalis create non-bridging oxygens on the silicons. If the number of Al ions exceeds that of the alkali ions, after all the available alkalis are associated with aluminium ions, each residual Al ion creates three NBO [92].

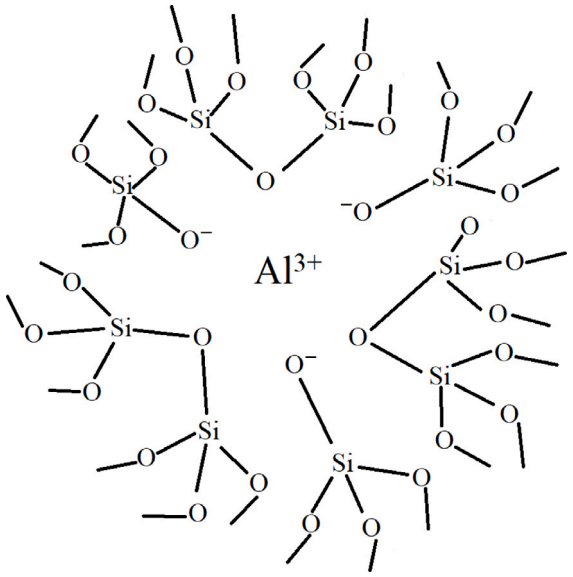

Fig. 16. Schematic representation of a glassy aluminosilicate network with Al^{3+} as a network modifier showing octahedrally coordinated Al^{3+} [92].

5.2. XPS studies of ion-implanted silica glass

Starting from the '80s, several research group investigated the surface of glasses doped by means of the ion implantation method (Refs. [100–107] and references therein). In the ion implantation, atoms of a determined chemical element are ionized and then accelerated towards the surface of a solid matrix by an electric field (as a consequence of a suitable potential difference). The accelerated ions enter the solid matrix and after loosing their kinetic energy by collisions with electrons and atoms of the bombarded matrix, they stop at a mean depth below the surface mainly depending on their mass, potential difference, host matrix composition, beam direction. Usually, the depth involved in the ion implantation are in the range from few nm to some hundreds of nm. Doping of glasses (in particular, pure silica) by ion implantation is mainly devoted to the preparation of nonlinear optical materials, as well as to new magnetic recording media, due to the formation of nanoparticles embedded in optical transparent matrix. XPS allowed to understand the chemical bonds formed between doping and host matrix atoms, clarifying the physical and chemical interactions among the different atoms involved in the ion implantation of glasses (Ref. [106] and references therein). Actually, depending on the pair "implanted atom-dielectric host", ion implantation of metals in glasses induces the formation of new compounds and/or metallic nanoparticles as a function of the reactivity of the atoms involved, even if the typical energies taking into play in the collisional kinetic processes during the implanted ion truck are much larger than the usual chemical bond energies [106,108]. With a careful XPS investigation, by using the silicon Auger parameter (see Fig. 11) and sputtering cycles, it was possible to ascertain the formation of Cr- or Ti-silicides after Cr (or Ti) high dose ion implantation in pure silica, distinguishing this compounds by metallic silicon [109]. Also in the case of implantation of nonmetal elements, XPS is able to give information about the different chemical bonds between the implanted and the host matrix atoms, for instance in the case of nitrogen implantation [110].

5.3. XPS studies of silicates

Until the last years, there has been limited use of XPS technique to study glass structure of silicates. NMR and Raman spectra, on

the contrary, have been much more widely used (Stebbins [111]; Zhang et al. [112]; Herzog and Zakaznova-Herzog [113]; Maekawa et al. [114]; Malfait et al. [115] and references). There are two main reasons why XPS has not been used to the extent that NMR has been. First, XPS is generally considered to be, and used mostly as, a surface technique rather than as a technique to obtain bulk structural properties. Second, the spectra resolution were relatively low. Indeed, the spectra were often too broad (FWHM ≥ 2 eV) to be interpreted properly. XPS studies of silicates generally have been centred on three surface application, as outlined by Hochella [116]:

(1) studies of the oxidation state of near surface atoms;
(2) studies of sorption reactions on mineral surfaces;
(3) studies of the alteration and weathering of mineral surfaces.

Only a few reports have focused his attention on the fourth application of Hochella, namely, the study of the bulk atomic structure and chemical state properties of minerals and glasses, proceeding to the analysis of a virgin surface, such as the cross section surface.

First studies conducted on silicate minerals showed that XPS was sensitive to certain structural details, but with limitations, i.e., the bridging oxygen and non-bridging oxygen signals were not resolved, and were incorrectly assigned. Unlike sulfides, which are mostly semiconductors, the predominant part of silicates are non-conductors, leading to charging and differential charging problems. These issues are mostly responsible for the large Si 2p and O 1s linewidths measured in silicate minerals. The significant advancement in charge neutralization methods, makes much more simple and accurate deal with this problem. A first demonstration of the improved resolution for crystalline silicate insulators was provided by Nesbitt et al. [91] in the early 2000s, where the narrowest possible Si 2p spectra (FWHM = 1.36 eV) were obtained using the charge compensation system adopted by Metson which utilizes the "magnetic confinement" illustrated in Section 3.1.

The bulk properties of some silicate glasses have been probed successfully by XPS by late seventies, (e.g., references R. Brückner et al. [117,118]; Veal et al. [119]; Jen and Kalinowski [120]; Matsumoto et al. [121]), demonstrating the feasibility of quantitative XPS bulk measurements. They used O 1s core level spectra to determine ratios of bridging to non-bridging oxygen, and other properties.

Preliminarily XPS spectra were broad, in addition, possible beam damage, which modifies the O 1s spectra [122,123] was apparently not recognized. The bridging and non-bridging oxygen signals remained only partially resolved in silicate glasses until the study of Matsumoto et al. [121]; followed by the studies of Dalby et al. [87] who presented well resolved spectra with consistent linewidths and line shapes for lead silicate glasses; as did Nesbitt et al. [123] and Sawyer et al. [124] for Na and K silicate glasses.

5.3.1. Bulk chemical analysis in silicates

Exploiting XPS, bulk chemical analyses are readily achieved, however, some important considerations are needed when selecting peaks to be used. Kinetic energies of photoelectrons should be similar to ensure that the depth of analysis is the same for all elements (Fig. 3). Unfortunately, it is not possible to fulfil this condition using conventional instrumentation since photo-peaks differ greatly in BE, and conventional XPS instruments with fixed source energies do not allow selection of the source energy (i.e., reconsidering Eq. (1), KE = hν - BE). Fortunately most elements produce several photo-peaks or Auger peaks, and in order to obtain bulk compositions any line may be used.

The Si 2p and Al 2p lines have close binding energies, 100 and 75 eV respectively, thereby by using a Al K_α X-ray source (hν=1486.6 eV) photoelectrons from these orbitals have the similar KEs (~1400 eV) and hence are derived from about the same sampling depth. The O 1s peak, on the other hand, is at about 530 eV (KE of ~950 eV), and reference to Fig. 3 demonstrates that O 1s photoelectrons are derived from a shallower depth than those from the Si 2p or Al 2p lines. As a consequence, Si atoms are "over-sampled" with respect to O, this means that the resulting analysis will over estimate the amount of Si in the sample. This difference can be revised taking into account that the escape depths vary from one compound to another. In some XPS spectrometer software it is possible to operate on their sensitivity factors, to achieve reliable results. If it is not possible, it can be useful to employ an appropriate standard to overcome this problem, thus bulk chemical analyses of glasses with errors of about 2% can be obtained. In the event that standards are not available, semiquantitative bulk chemical analyses of glasses can be obtained, but errors are considerable (5% to 10% absolute; e.g., Refs. [122–124]).

Unless otherwise stated, all XPS bulk chemical analyses mentioned in this review refer to fractured surfaces. Accordingly, it should be noted that the topmost atomic layer surface contributions to both the BO and NBO peaks of the O 1s spectrum are rather low. Nesbitt and Bancroft [10] estimate that the O 1s surface contribution would be less than 2% of the bulk peak, and within the error associated with fitting the spectra. Consequently, there is no good evidence for a strong surface contribution to O 1s (or other) spectra, thus the BO and NBO peaks of O 1s and other spectral lines reflect bulk properties [123].

Binding energies in silicate glasses. The addition of alkali metals to silicate glasses affects the network structure, and this reflects on the binding energies of all photo-peaks [121,123]. The Si 2p and O 1s BEs vary considerably depending on the chemical environment of Si or O. For example, referring to sodium silicate glass, the O 1s BE can be affected by the neighbouring atoms around the O as shown in Fig. 17. The bridging oxygen (Si–O–Si) has a higher BE than the non-bridging oxygen (Si–O–Na). The difference (close to 2 eV) in O 1s BE between the BO and NBO oxygen atoms is due to the replacement of Si in BO with the electropositive Na in NBO that leads to a more negative O in NBO and a smaller O 1s BE for NBO.

The relationship of the Na 1s, Si 2p, O 1s (BO) and O 1s (NBO) BEs to the Na_2O content of Na-silicate glasses is illustrated in Fig. 18 [10]. Increased Na_2O concentrations clearly cause the BE of each photopeak to shift to lower BE values. The same behaviour is observed in K-silicate glass as the K_2O content increases [124]. As the 3s valence electrons of Na are shared by the more electronegative atoms (i.e., O and Si) of the glass, the electron density over O and Si atoms increases, thus decreasing their BE [10]. It is interesting to note that the BO slope (Fig. 18 (c)) is larger than the NBO slope (Fig. 18 (d)), and also that the Na 1s slope is negative (Fig. 18 (a)). There is an increase in the electron density over all Na atoms and a decrease in the Na 1s BE with increasing Na_2O content. For each incremental increase in Na_2O, a progressively smaller portion of the Na 3s electronic charge is transferred to the O and Si resulting in an increase in Na 3s electron density with increasing Na content.

Si 2p linewidths. The width of the Si 2p and O 1s signals are also determined by final state vibrational contributions and phonon broadening [11], and are similar for all silicates glasses (see Section 2.1.6). There are other additional factors contributing to small increases in Si 2p linewidths of silicate glasses. Presumably, slightly broader peaks origin from the absence of long range order, since there are more energetically distinct Si sites in silicate glasses. A significant contributor to linewidth is given by the number of Si moieties (Q-species) in a silicate glass. Whereas the number of Q-species observed in the majority of crystalline silicates is limited, five Q-species may coexist in silicate glasses [111], and each Q-species will give rise to a separate, energetically distinct, Si 2p signal, with approximately the same FWHM [11]. If the energy separating each signal is small, a distinguishable signal for each will not be observed. Instead, one broad Si 2p peak will result [125].

In accordance with electronegativity arguments, the Si 2p peak for the Q_4 species should be located at the highest binding energy and that of the Q_0 species should be located at the lowest binding energy, with the Q_3, Q_2 and Q_1 species located sequentially, between the two extremes. Where one Q-species of a glass prevails, the Si 2p peaks should

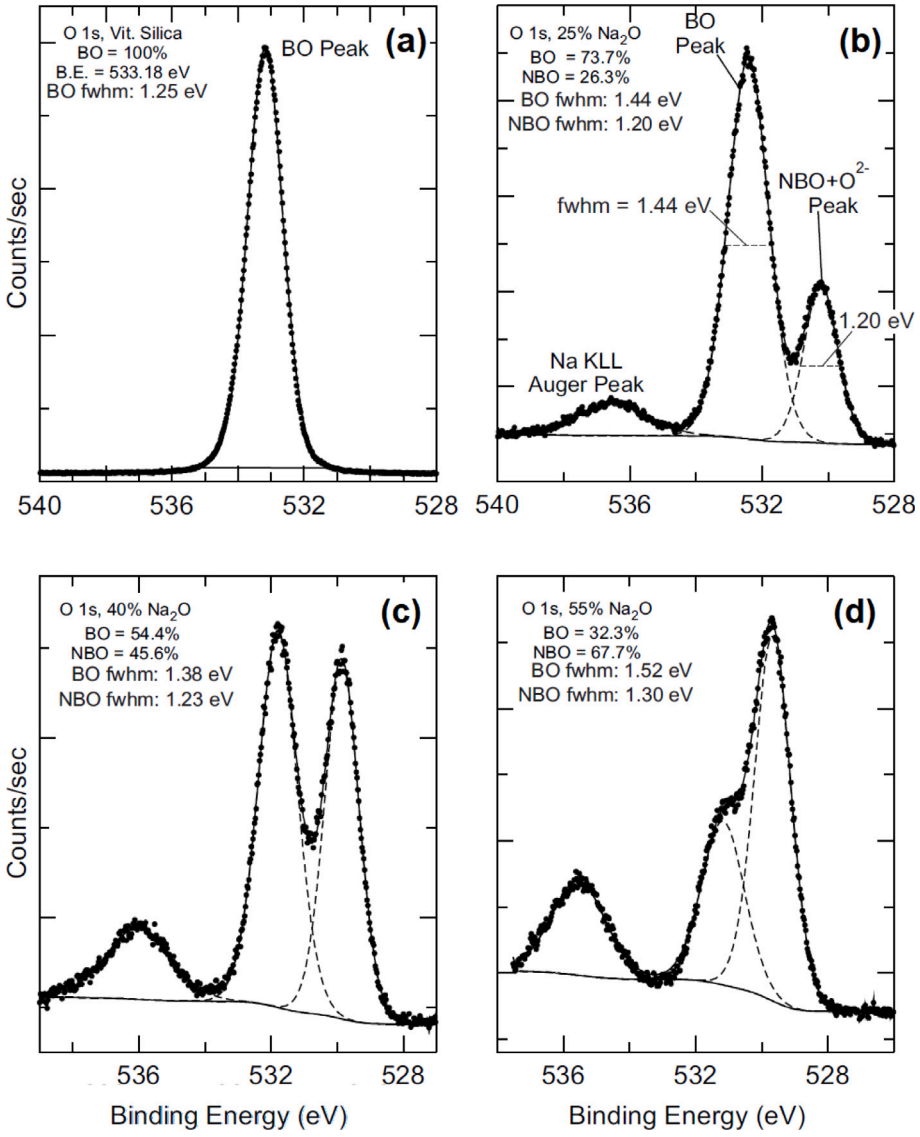

Fig. 17. O 1s spectra of: (a) vitreous silica; (b) to (d) Na-silicate glasses containing respectively, 25%, 40%, and 55% Na_2O. Each peak was fitted with a Voigt function, including the NBO, BO and Na Auger KLL peaks.
Source: Original data from Ref. [123].

be narrow (e.g., vitreous silica, Fig. 19 (a) and in a glass where two species are equally abundant, a much broader Si 2p peak should result (e.g., Fig. 19 (b)). Whether one species or two species are dominant in an alkali silicate glass depends on the M_2O content of the glass. Si 2p spectral widths varies with the alkali molar fraction [111,114], but the Si 2p linewidth does not increase or decrease monotonically with respect to the M_2O content (Fig. 19 (a) to (d)).

The effect of changed Q-species abundance is more evident in K-silicate glasses. A series of K-silicate glasses collected by Sawyer et al. [124] displayed unusual Si 2p peak shapes, some showing distinct shoulders and others displaying distinct asymmetry (Fig. 20). The latter features may result from the presence of various Q-species. The Q-species distributions derived from the XPS spectra are broadly consistent with abundances obtained from NMR studies [114,115], as emphasized by Sawyer et al. [124]. Confirming that Q-species abundances affect the shape and breadth of Si 2p XPS spectra of silicate glasses. Unfortunately, the XPS resolution is not sufficient to reliably quantify Q-species abundances.

5.3.2. O 1s spectra, NBO and BO linewidths

Two peaks constitute the O 1s spectra, indeed, the latter include contributions from all oxygen spectra in the glass. As mentioned before, the higher binding energy peak in alkali silicate glasses is attributed to oxygen bridging two Si atoms (BO peak) and the second, lower BE peak, is derived from other types of oxygen bridging the alkalis and Si atoms (e.g., NBO peak) (Ref. [123] and references therein).

For K-silicate glasses, the percentages of BO calculated from experimental NMR data [114,115,126] and from XPS are consistent between about $0.13 < x < 0.25$ (where x is the alkali molar fraction), demonstrating that the two techniques can yield similar results. The discrepancies of the data, outside of the latter compositions, may be due to different conditions of synthesis of the glasses for the XPS and NMR experiments [123,124].

The O 1s NBO and BO linewidths for silicate glasses (Fig. 17) are similar to linewidths of crystalline silicate minerals, as demonstrated by Bancroft et al. [11]. However, the linewidths of the BO signals for Na-silicate glasses are all broader than the vitreous silica linewidth (1.25

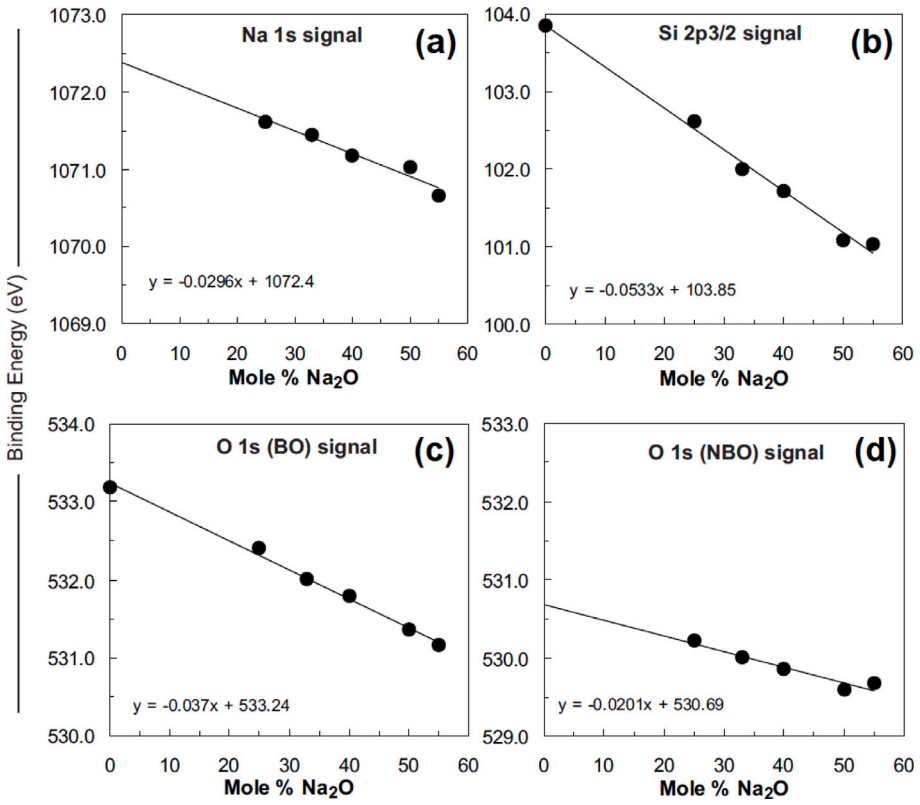

Fig. 18. Binding Energies of the (a) Na 1s, (b) Si 2p, (c) O 1s (BO) and (d) O 1s (NBO) core level as a function of the mol% of Na_2O in vitreous silica and Na-silicate glasses. The solid lines are linear fits performed on the data points.
Source: Original data from Ref. [123].

eV), in the range from 1.36 eV to 1.52 eV. NBO linewidths of Na-silicate glasses (Fig. 17, lowest BE peak in each spectrum) range from 1.18 to 1.30 eV and average 1.22 eV, a value similar to the NBO linewidth for olivine which contains only SiO_4^{4-} tetrahedra. A possible explanation is given by the fact that Na- and Li-disilicate crystalline phases (e.g., $Na_2Si_2O_5$) include two types of bridging oxygen atoms [127,128]. One type bridges two Si atoms (Si–O–Si), as in vitreous silica. The second type again bridges two Si atoms, but it is also bonded to a Na atom with the BO–Na bond length being similar to the NBO–Na bond lengths [129].

The two BO moieties likely exist in Na-silicate glasses. Nesbitt et al. [123] and Sawyer et al. (Ref. [124] and references therein) argued that each type of BO moiety (i.e., BO–Na and BO moieties) should give rise to a separate BO peak (each of 1.2 to 1.3 eV in FWHM) due to electron density differences over the O atom of each moiety. The BO-Na moiety should be located at slightly lower BE than the BO moiety, thus providing an explanation for the broadened BO peak in Na-silicate glasses (Fig. 17 (b) to (d)) over that of vitreous silica (Fig. 17 (a)).

A third type of oxygen, O^{2-}, is required in Na-silicate glass to explain the fractions of BO observed [123,130]. ^{17}O NMR experiments on $CaSiO_3$ glass [112] have demonstrated that BO and NBO alone could not provide charge balance to the system, suggesting the presence of small amounts of O^{2-} atoms. Other NMR experiments have indicated small amounts of O^{2-} in sodium and potassium silicate glasses containing lanthanum [131].

The O^{2-} signal itself cannot be resolved in the XPS spectra but its position can be inferred from electronegativity arguments. Briefly, the O^{2-} signal is located within the NBO peak. The BO peak has a high binding energy due to the low electron density on the oxygen atom bridging two silicon atoms. Since the NBO has a greater electron density due to the presence of the alkali metal M in the Si–O–M moiety, the NBO peak will be located at a lower binding energy. The O^{2-} contribution is bonded to two M atoms (M–O–M moiety) and it too will have a greater electron density than the BO contribution. To conclude, the O^{2-} peak is placed at a binding energy close to the NBO peak and it cannot be resolved due to the low abundance of O^{2-} and its close vicinity to the NBO contribution.

5.3.3. *X-ray beam damage effects on BO%*

With the exception of the complications of glass synthesis (homogeneity) and exposure of clean fracture surfaces for analysis, collection of high quality core level spectra of silicate glasses can be complicated by prolonged exposure to the X-ray beam [122,132].

Sharma et al. [122] demonstrated that the X-ray beam affected Na–Ca-silicate glass (the migration of Na and Ca to the surface was revealed) and X-ray beam damage, or damage from secondary electrons associated with photoemission [133] or after the exposure to an electron beam [134], was observed also in three binary glass systems: the Pb-silicate [87], Na-silicate [123] and K-silicate [124] glasses. Beam damage also affects analytical results [122], as shown in Fig. 21 (a), where changes in the O 1s spectrum (with the BO component kept constant) with increasing exposure times is illustrated. Fig. 21 shows that there is an increase in the atomic percentage of NBO (Fig. 21 (b)) and a decrease in that of BO (Fig. 21 (c)) with increasing time of the experiment, seeing that there is a decrease in the total oxygen content on the glass surface from the preferential depletion of the BO atoms on the glass surface [122].

The network modifiers such as Na and K are mobile [135,136] in the X-ray beam and mobility causes BO:NBO ratios to increase with time of exposure [87,123,124], thus increasing the polymerization of the glass. This damage has not been observed for crystalline silicates although additional studies are required. It seems that the structures of glasses are much more fragile than crystalline structures and are readily altered. This effect can be circumvented by an appropriate sampling strategy. The first spectrum collected should be a survey scan (from which compositions are derived) which generally takes 3 to 5 min,

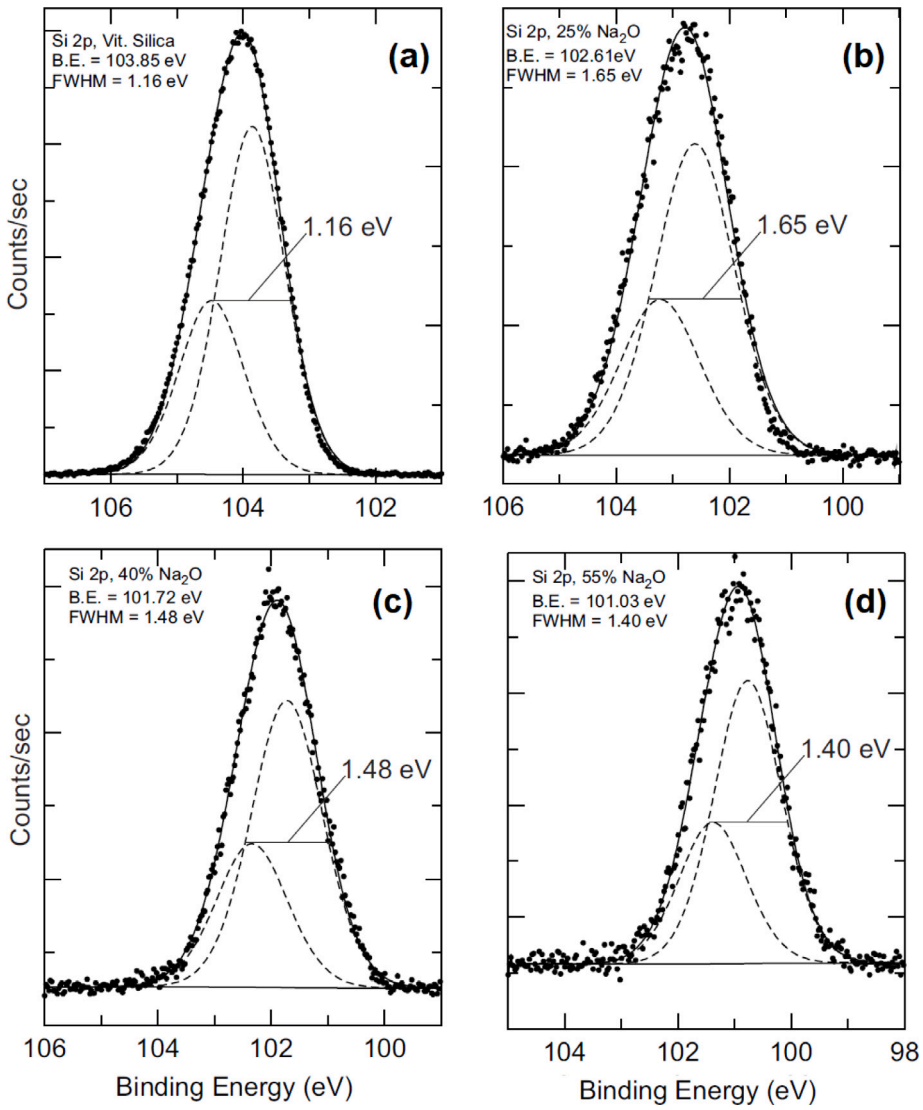

Fig. 19. Si 2p spectra of: (a) vitreous silica; (b) to (d) Na-silicate glasses containing respectively, 25%, 40%, and 55% Na_2O. Each spectrum has been fitted with an Si 2p spin–orbit doublet peak.
Source: Original data from Ref. [123].

thus minimizing the effects of beam damage. Narrow scans should be collected in cycles, where each narrow scan is collected a number of times so that changes in spectra over time are documented. Then another survey scan should be collected at the end of the analytical session to determine the extent of damage (with respect to composition). Alternatively, low source intensities would limit beam damage but would also diminish count rates. Regardless of the technique used to minimize beam damage, this effect should be monitored, for example by plotting BO mol% against exposure time, and by extrapolating to zero exposure time. In this way it will be possible to yield reliable BO:NBO ratios of the glasses [123,130].

5.3.4. XPS studies of borosilicate glasses

The structure of borosilicate glasses has been studied for a long time with different spectroscopic methods including NMR [93], Raman [137] and X-ray photoelectron spectroscopy [138,139]. As shown in the previous section, dedicated to silicate glasses, XPS has been extensively used to infer the structure and the chemical state of glasses by separating O 1s photoelectron spectra into BO and NBO components.

In the early 90 s, O 1s XPS spectra in sodium borosilicate glasses were examined. Hsieh et al. [138] separated the O 1s spectra into three peaks of one BO and two NBOs (Si–O–Na and B–O–Na) and confirmed that the structure of sodium borosilicate glasses agreed with the Dell model [95]. They also pointed out that Na 1s signal shifted chemically with composition. In their XPS measurements, binding energy of Si 2p was adopted as internal energy reference assuming that change in the Si 2p binding energy due to the substitution of B_2O_3 for SiO_2 should be small.

Afterwards, Miura et al. [139] conducted an XPS study on a series of $RNa_2O{\cdot}B_2O_3{\cdot}KSiO_2$ (R = 0.2 to 5.0, K = 0.5 to 6.0) glasses. The absolute value of binding energy and its chemical shift against the glass composition were determined with respect to the external energy reference of $Au4f_{7/2}$. In their work, the excess of surface charging was successfully neutralized by combining the use of a flood gun and a metallic mesh screen. The O 1s spectra were resolved into two components assigned to BO and NBO (Fig. 22). The width of the components was quite small, and the further separation into B–O–B, B–O–Si, and Si–O–Si seemed to be insignificant. The binding energies of O 1s, B 1s, Si 2p and Na 1s commonly shifted towards lower energy side with increasing R at constant K. The lower binding energy shift of O 1s is generally interpreted as an increase in the electronic density of oxide ions. The authors claim that a change in the O 1s shift can be recognized when the average O 1s binding energy become 531.0 eV, and they assign this variation to the formation of NBO in BO_3 unit.

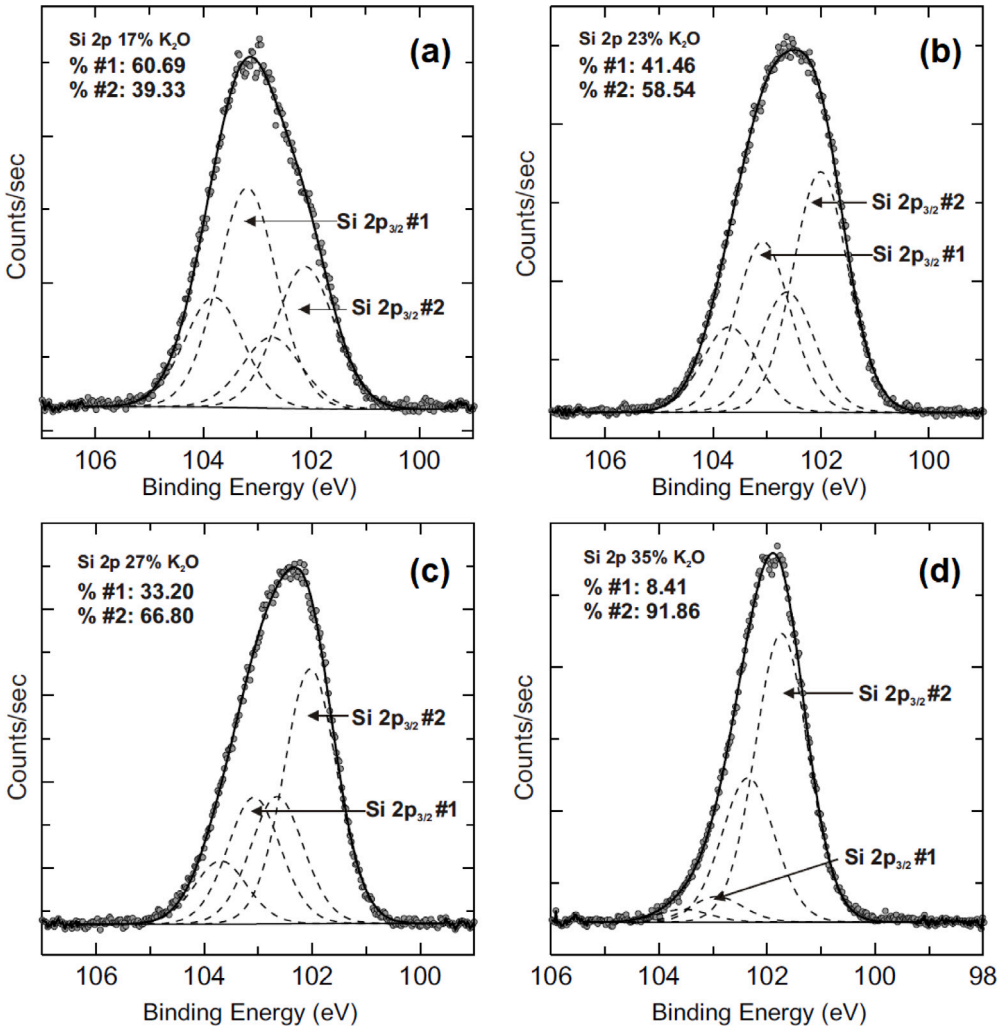

Fig. 20. Si 2p spectra of K-silicate glasses. (a) to (d) K-silicate glasses containing respectively 17%, 23%, 27% and 35% K_2O. The peak shapes vary dramatically and non-systematically with K_2O content of the glasses. Each spectrum has been fitted with an Si 2p spin–orbit doublet peak. The area for each doublet is provided in the upper left corner of each diagram.
Source: Original data from Ref. [124].

For the small K (=0.5 and 1.0) families, the NBO fractions determined by XPS agreed very well with the Dell model. According to this model no NBOs are formed at smaller R values than $R^*=1/2 + K/16$, however, the XPS experiments revealed that the NBO components have already appeared to be present in considerable amount at around $R = R^*$, and the discrepancy between the XPS results and the Dell model became more significant with increasing K. Except for the small K glasses, the discrepancy was commonly observed in the glasses where the average O 1s binding energy was higher than 531.0 eV. These results suggest that sodium oxides are competitively shared between silicate and borate networks even in the small R glasses and there is no need to assume any macroscopic building units such as reedmergnerite and diborate groups [93,95]. Hence, a new sharing model was proposed by Miura et al. [139,140], where a new coefficient α, together with two critical values R_c and K_c were introduced, for more details see Ref. [139].

Until R reaches R_c, namely, where the average O 1s binding energy is equal to 531.0 eV, sodium oxides are introduced into silicate units with the distribution coefficient α (where, $0 \leq \alpha \leq 1$ and α depends on K); and the residual $(1 - \alpha)R$ is consumed to form tetrahedral borate units (BO_4), no NBO bound to boron. Above R_c, it is assumed that the amount of BO_4 units maintains a constant value at $R = R_c$, namely, sodium oxides are used to form BO_4 units, and the additional sodium oxides (R-R_c) are proportionally distributed between silicate and borate networks. α is equivalent to the relative amount of Si–O–Si bonds with respect to total amount of bridging oxides. Below $K_c = 1.5$, Na_2O is preferentially consumed by borate units, since there should be no Si–O–Si bond in glasses.

5.3.5. Surface H_2O and OH

As declared at the beginning of the previous section, the O 1s spectra were acquired within minutes after fracturing the glass in high vacuum, nevertheless, small amounts of impurities were observed in the spectra [87,123,124]. Very small amounts of carbon were measured on the surface of almost all glass samples as indicated by development of a C 1s XPS peak at approximately 285 eV binding energy. This peak does not affect the analysis of O 1s peaks, actually it is advantageous for calibrating binding energies as indicated in previous sections. Conversely, after the H_2O adsorption the O 1s signal may be affected. Indeed, the highly reactive Si dangling bonds on fresh fracture surface may react with H_2O, the main components of the residual gas in UHV chamber, resulting in the dissociation of the water molecule. This leads to the formation of silanol groups (SiOH), giving a contribution of about 5 mol% to the total O 1s signal.

The detection of silanol groups is difficult for glasses, because the related peak (BE around 532.9 eV) overlaps the BO peak of vitreous silica (usually around 532.7 eV) and is likely to overlap BO signals of most glasses [141]. Furthermore, many studies have shown that

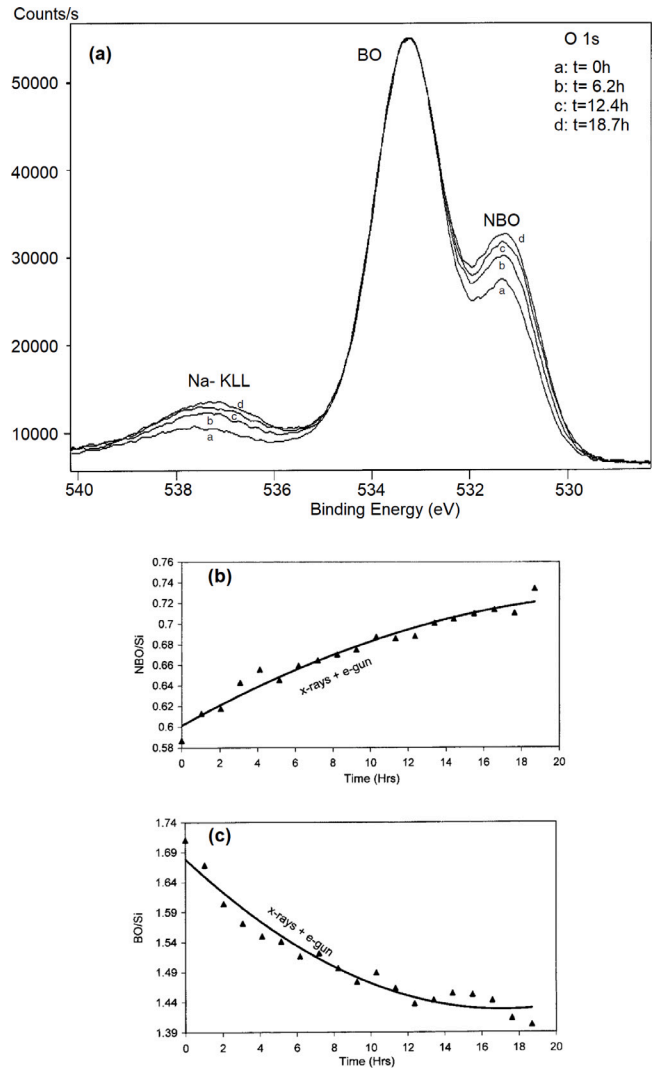

Fig. 21. (a) The XPS spectra of a soda–lime silicate glass showing an increase in the fraction of non-bridging oxygen with time of the experiment. Separate variation of non-bridging (b) and bridging oxygen (c) (normalized to Si concentration) with XPS experiment time under exposure to both X-rays and electron flood gun. The solid lines are least-square fits to the data, as a guide to the eye.
Source: Original data from Ref. [122].

O 1s peaks from surface, supposed to be affected by OH and H_2O, due to large vibrational broadening have linewidths wider than 1.5 eV (e.g., Knipe et al. [142]). The accumulation of surface OH should result in a wider BO, thus affecting the BO% evaluation.

To summarize, all of the above evidence indicates that, referring to a fractured glass surface, there are no systematic errors in the XPS BO% values. However, studies on alteration, corrosion and weathering of glass surface deserve a separate discussion, and it will be addressed in Section 6.

6. Chemical durability

Glass is generally a stable and resistant material, however, under certain conditions, can be "chemically attacked". For instance, when the glass is in contact with either liquid or vapour waters it is vulnerable to damage. The chemical composition and the structure of a glass are the key factors in the interaction of glass with the environment. Under certain stressful conditions its optical properties, chemistry and structure are modified, based on different deterioration processes that

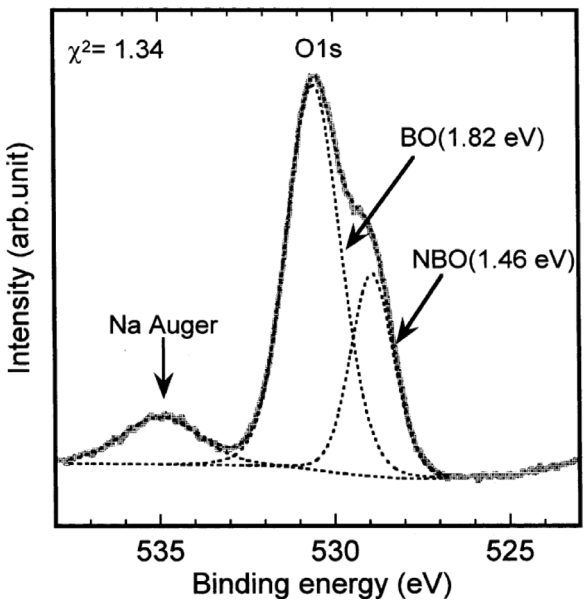

Fig. 22. O 1s spectrum for $2.0Na_2O\ B_2O_3\ 2.0SiO_2$. In the experimental spectrum (grey thick line) there is a well-resolved peak around 530 eV accompanied by a shoulder at lower binding energy. The small peak around 535 eV is an Auger electron signal of the Na^+ ions. (For interpretation of the references to colour in this figure legend, the reader is referred to the web version of this article.)
Source: Original data from Ref. [139].

may be involved. The interest in glass corrosion or glass weathering stems from the need to understand the stability of glass containers used for food or drugs as well other glass products exposed to extreme conditions (e.g., windows). A detailed understanding of the stability of glasses under liquid or atmospheric attack is thus of considerable importance.

6.1. Corrosion mechanisms

The chemical durability is usually considered to be related to the rate of attack of water and aqueous solutions on glass. Three types of reactions can take place between glass and aqueous solutions: (1) hydration, in which molecular water enters the glass as an intact solvent; (2) hydrolysis, in which water reacts with metal-oxygen bonds in the glass to form hydroxyl groups; and (3) ion exchange reactions, in which modifier cations such as sodium are replaced by protons (or other cations).

For complex glasses, all three reactions arise simultaneously, and each reaction influences the kinetics and mechanisms of the other reactions. After a brief description of the features governing each reaction type, the dissolution behaviour of different glass compositions are discussed.

6.1.1. Hydration and hydrolysis

Two distinct mechanisms can lead to water penetration in a glass surface. The water molecule can either diffuse as an intact molecular species into the glass through void space between oxygens in the structure or it can undergo hydrolysis and condensation reactions with metal-oxygen bonds:

$$H_2O + M{-}O{-}M \longrightarrow M{-}OH + HO{-}M \longrightarrow M{-}O{-}M + H_2O. \quad (13)$$

This mechanism is not fully reversible, resulting in the presence of both hydroxyl groups and molecular water in the glass, as demonstrated by NMR studies [4]. The ruling process for water penetration into the solid depends on the relative rates for the two mechanisms. The rate of the molecular diffusion pathway is primarily determined by size

of the voids present in the glass network, that are imposed by steric constraints. For silicates, the void size depends on the distribution of rings in the structure composed by interconnected silicate tetrahedra. For complex glasses, such voids can be filled or partially blocked by modifier cations such as Na^+. When the void contained in the structure are large (>0.7 nm) with reference to the kinetic diameter of the water molecule (0.28 nm), the molecule can diffuse through silicates as rapidly as possible through liquid water ($D = 3 \times 10^{-5}$ cm^2/s). The diffusion is much slower ($D = 2 \times 10^{-13}$ cm^2/s) when the ring opening is comparable in size with the water molecule. If the structure includes smaller rings, molecular water cannot penetrate. In the latter case, the only way for water to penetrate the voids is to force the rings via hydrolysis.

The dissolution behaviour of most glasses is ruled by reversible hydrolysis and condensation reactions (Eq. (13)): this is due to the fact that most glass structures do not contain openings which are large enough to allow the entrance of molecular water. The kinetics of network hydrolysis is determined by the distribution of local structural units present in the glass and on the chemistry of the solution.

The tetrahedral SiO_4 sites, that characterize all silicate glasses, are prone to nucleophilic attack [8] mainly by OH^- to form a reactive five-coordinated intermediate which can decompose leading to the rupture of the Si–O–Si bond.

$$\mathrm{Si{-}O{-}\underset{\mathrm{OH}}{\overset{\mathrm{OH}}{Si}}{-}OH} + OH^- \longrightarrow \mathrm{Si{-}O{-}\underset{\mathrm{OHOH}}{\overset{\mathrm{OH}}{Si}}{-}OH} \longrightarrow Si{-}O^- + Si(OH)_4. \quad (14)$$

The rate of the reaction (Eq. (14)) will increase if the pH (i.e., the OH^- concentration) increases.

When solution volumes are limited, glass dissolution reactions can modify both the pH and $Si(OH)_4$ concentrations with time, leading to time-dependent dissolution kinetics. Moreover, the kinetics can be influenced by environmental temperatures, not only because temperature can enable reactions such as the hydrolysis reaction, but because the temperature affects parameters such as the solubility of dissolved species such as $Si(OH)_4$.

6.1.2. Ion exchange

Ion exchange can be considered as a selective dissolution. In this type of reaction the mobile ions are leached but the parent material remains relatively untouched. The original matrix keeps its dominant ions ratio although its secondary and most mobile ions continue to leach through the matrix.

Leaching via ion exchange is described as an interdiffusion process, where cations are exchanged:

$$Si{-}O{-}Na^+ + H_3O^+ \longrightarrow Si{-}OH + Na^+ + H_2O, \quad (15)$$

$$Si{-}O{-}Na^+ + H_2O \longrightarrow Si{-}OH + Na^+ + OH^-. \quad (16)$$

Ion exchange, network hydrolysis, and hydration reactions in glass are strongly correlated. Hydrolysis reactions can open up rings to promote the penetration of the glass by both the water (Eq. (13)) and H_3O^+ involved in the exchange process (Eq. (15)). In addition, ion exchange reactions generate voids which water can permeate and create reactive species such as silanol groups which induce the network repolymerization. Polymerization of silanol groups reduces ion exchange sites from the leached glass surface, leading to an ion exchange reaction kinetically irreversible. Finally, the combination of hydrolysis and repolymerization can open up the structure of the surface, increasing the rates of diffusion of water and other species [143]. This amorphous, porous, hydrated layer is commonly referred to as a "gel layer". Its thickness varies significantly, from a few nanometres to macroscopic size, with the glass composition and with the leaching time and conditions. Its effect on the alteration kinetics is a debated question [144]. Some authors assert that it constitutes a barrier with respect to the diffusion of reactive species between the pristine material and solution (see Ref. [145] and references).

All of the above properties are also found in the case of alkali silicate and alkali alumino- or borosilicate glasses as described below.

6.2. Silica–water reactions

Modifier cations are not present in silica, hence, ion exchange reactions can be neglected. Silica structure, as well known, is characterized by bridging oxygens and Si tetrahedral sites Q_4, which are expected to be resistant to hydrolysis. Experimental results on both the dissolution and hydration of silica confirm that it is highly resistant to attack by water as supposed on the basis of glass structure.

In aqueous solutions, the silica dissolves via network hydrolysis before it can be hydrated. On the contrary, when silica is exposed to steam atmospheres the reaction products of network hydrolysis do not have a solution phase to dissolve into, thus hydrated layers can be created [143].

Although silica is not inclined to aqueous corrosion, except in strong base [146], silica glass can be subjected to environmentally assisted crack growth, or stress corrosion cracking [147]. The corrosion reaction between glass and water vapour is assumed to be enhanced by the applied stress, leading to the extension or the sharpening of the crack and eventual failure [148]. The mechanism for stress corrosion implicates the rapid hydrolysis of local Si–O bonds which are deformed via applied stress.

6.3. Leaching of alkali silicate glasses

As regards alkali silicate glasses, unlike silica, network hydrolysis is not the only factor playing an important role to the surface hydration. As alkali cations are removed from the surface via ion exchange, the alkali ions can be replaced by water, aiding diffusion of water into the surface.

The rate of attack on silicate glass by water is governed by solution pH, volume of solution in contact with the glass, solution concentrations, and glass composition. In contact with liquid water, the sodium hydroxide dissolves increasing the water alkalinity. Obviously, the water pH rapidly increases when the volume of solution is small compared to the surface area of glass. The rate of interdiffusion of the ions in the glass determines the rate of ion exchange reaction. Therefore, composition changes that decrease the rate of diffusion, e.g., the addition of calcium oxide to a sodium silicate glass, enhance durability.

Ion exchange reaction also takes place in contact with water vapour, and the sodium hydroxide remains on the glass surface. It quickly reacts with carbon dioxide from the atmosphere, forming sodium bicarbonate ($NaHCO_3$) crystals on the glass surface [149]. The hydrated surface of an alkali silicate glass is relatively durable when it can preserve the structure of the dry glass, otherwise it can transform into a less dense structure in which ionic transport is faster [149,150].

6.4. Composition dependence

In simple alkali silicate glasses, the total number of non-bridging oxygens increases with the modifier content. As a consequence the effective crosslink density of the glass is progressively reduced, Q_3 and Q_2 sites are thus created. These latter are more susceptible to network hydrolysis and enable the formation of silanol groups via ion exchange, hence, structural alterations within the leached layer are promoted. Typically, network hydrolysis is more rapid when non-bridging oxygens are present. Site reactivity follows the trend $Q_1 > Q_2 > Q_3 > Q_4$. Therefore, the alkali silicates are more prone to network hydrolysis than is silica [143].

For a given modifier, the reactivity of the alkali silicate glasses depends on the non-bridging oxygen content. On the other hand,

glasses containing the same modifier content but different modifier cations (e.g., Na^+ versus K^+) do not react with water at the same rate. In general, the lower the charge-to-ionic radius ratio of the modifier cation, the more reactive the glass will be [151]. Binary potassium silicate glasses have reduced durability than binary sodium silicate glasses of the same molar alkali composition. A plausible reason for this result is that the hydronium ions (H_3O^+) has a higher mobility in potassium than in sodium silicate glasses because potassium and hydronium ions have about the same effective radius (1.3 Å) [149].

If a second alkali oxide, such as potassium, is added to a sodium silicate glass, the durability of the glass is increased [149]. Furthermore, the increase is more significant when the molar ratio of alkali ions is roughly equivalent. This is named "mixed-alkali" effect [152], usually the mobility of an alkali ion is reduced when another alkali ion is added. The mechanism of this effect is being debated.

Addition of CaO to make a soda–lime glass greatly improves the corrosion resistance with respect to a simple sodium silicate glass. Even the most ancient of glass samples are not binary alkali silicates but contain some calcium and magnesium oxides. Probably, ancient glassmakers realized that the binary alkali silicates were easily attacked by water and that the addition of lime or magnesium improved durability. Thanks to diffusion measurements is it possible to establish why the addition of calcium oxide improves durability. As an example, in glasses containing 5%–10% CaO, the diffusion coefficient of sodium ions is up to a factor of 50 times lower than in a binary sodium silicate glass with the same soda concentration [149]. This behaviour can be explained as resulting from a blocking of alkali ion motion by the doubly charged calcium ions that are bound tightly in the silicate network.

6.5. Corrosion of alkali boro- and aluminosilicate glasses

All the considerations discussed above concerning the hydration, hydrolysis and ion exchange of alkali silicate glasses also apply to alkali boro- and aluminosilicate glasses. However, the knowledge of the structural differences between alkali silicates and glasses such as aluminosilicates becomes crucial to understand the relative rates at which the glass alteration reaction occurs.

In alkali boro- and aluminosilicate glasses, modifier cations can be charge compensated by BO_4^- and AlO_4^- sites in addition to non-bridging oxygens [143]. Such sites transform both the inherent reactivity and extended structure of the glass. Addition of a few percent Al_2O_3 has long been known to increase durability, since alumina reduces the tendency to form a transformed layer [153]. Moreover, anionic tetrahedral sites such as AlO_4^- are approximately five orders of magnitude more resistant to ion exchange by protons than are non-bridging oxygens. Selective leaching from such sites does not occur above pH 5 [143].

In order to better exemplify the role of network structure and chemistry in borosilicate leaching can be useful to consider glasses having a fixed silica content and systematically varying the Na_2O/B_2O_3 content [143,154]. In sodium-rich glasses, most Na^+ is compensated by non-bridging oxygens, and the dissolution of the glass reflects that of simple sodium silicate glass. As Na_2O decreases and B_2O_3 increases, all boron initially form tetrahedral borate groups, thus decreasing the mole fraction of sodium associated with non-bridging oxygens and reducing dissolution rates. All Na^+ is compensating network borate sites. Although the network is not quite as stable as fused silica, the glass exhibits uniform dissolution as long as the solution pH does not promote removal of borate groups via hydrolysis [143]. Borate-rich compositions phase separate into a sodium borate phase (which easily dissolves) and a silica-rich phase (which is resistant to attack). For this composition, sodium removal occurs via hydrolysis of the borate phase rather than via ion exchange, regardless of the solution pH.

For more details concerning the environmental dependences for both ion exchange and network hydrolysis, expected on the basis of the acid–base properties of the silanol group and the hydrolysis characteristics of Q units in silicate networks, see Ref. [143].

6.6. Restructuring of leached layers

Alkali leaching is not a reversible ion exchange reaction, because silanol groups thus created react with each other to form Si–O–Si bonds (see Eq. (13)) [143]. The network repolymerization results in the total restructuring of glass, from the initial random network into a material which resembles an aggregation of colloidal silica particles [155]. Raman and NMR studies of leached layers show that the molecular structure of particulates within the restructured surface resembles fused silica [143]. Regardless of the initial Q distribution in the glass, Q_4 units prevail in the leached layer, with Q_3 units primarily concentrated on the particles surface. Many ion exchange sites present in the pristine structure are eliminated. The other significant consequence of surface restructuring is that the leached layer is transformed from a diffusion barrier into a material containing interconnected voids large enough (>3 nm) allowing water and other species to diffuse through them.

6.7. Weathering

The degradation of a glass surface due to interaction with the atmosphere [156] is referred to as "weathering". Heat and humidity cycling or storing glass in a confined space as well as increased concentration of aggressive gasses such as SO_x, CO_2, and NO_x usually promote weathering. This mechanism involves the ion exchange but no dissolution of the glass takes place. In addition, the reaction products (usually sodium bicarbonate) crystallize on the surface of the glass [149]. Since these crystals are alkaline and absorb water from the air, they can attack the glass in the local areas where they have formed, resulting to a pitted surface.

The interdiffusion coefficients of hydronium and sodium ions determine the rate of weathering, so resistance to weathering and resistance to aqueous corrosion are closely related. When the glass surface reacts with furnace atmospheres containing sulphur improves its chemical durability. Oxygen and water are also present in the furnace gases, resulting in the following ion exchange process [149]:

$$2\,Na^+(glass) + SO_2 + \frac{1}{2}\,O_2 + 3\,H_2O = 2\,H_3O^+ + Na_2SO_4. \quad (17)$$

The sodium sulphate crystallizes on the glass surface, but is not as alkaline as sodium bicarbonate or hydroxide and so does not attack the glass; it can be washed away at lower temperatures. After the ion exchange reaction Eq. (17) a relatively thick layer containing H_3O^+ (or perhaps H^+) ions is formed on the glass surface, and since no dissolution is involved the glass is quite durable at lower temperature where diffusion is much slower.

The extensive weathering leads to the formation of an altered, alkali-depleted, silica-rich layer. The latter is characterized by an expansion coefficient that is rather different compared to the glass substrate underneath. As a consequence, when containers are filled with any kind of liquid, even water, the substrate and the altered layer are subject to strong rehydration to an extent that depends on their relative thickness and chemical durability. When the thickness and the flexibility of the altered layer become critical as compared to the substrate, the layer begins to crack [157].

6.8. Delamination propensity

Delamination refers to the mechanism for producing glass flakes (or lamellae) detaching from the inner surface of glass containers, different from precipitation mechanisms. This phenomenon is due to the interaction of glass with the solution in contact with it. Glass flakes are usually observed as floating shining particles. The term "delamination" specifically refers to the formation of glass flakes in vials obtained through tubular converting process [158]. During bottom forming of a container from a tube glass, the high temperatures necessary to form the bottom, cause volatilization of glass elements like B or Na [159]. These elements condense in colder regions of the inner side of

the tube, forming small, round sodium borate adsorbate dots. These surface layers are enriched in sodium and boron species and therefore have reduced chemical durability and corrode at higher rates than the surrounding glass. Since these dots are water-soluble can be washed away in a cleaning process. As soon as the altered layers are removed, a crater-like pit forms, as the final step of this process. However, those pits are not an indicator for delamination (Ref.[160] and references). The corrosion rate observed for these regions depends upon the degree of composition alteration during the forming process, the aqueous solution strength (pH, concentration, etc.) and accelerating conditions (autoclaving, storage temperature, etc.).

Since delamination may occur after a long incubation time, different accelerated tests have been proposed to predict the delamination propensity. A method based on the measurement of Si in autoclave extractions at 121 °C with a 0.9% KCl solution was suggested by Guadagnino and Zuccato [157] to highlight the propensity to delamination. If the silica concentration measured in solution after autoclaving increases, this growth can be related to a typical glass corrosion mechanism, inducing the dissolution of glass elements and/or leaching of glass elements via ion exchange processes. In some cases, it seems to also be related to a higher probability of delamination. Indeed, as concluded by Iacocca et al. [161], dissolution of silica occurs well in advance of the appearance of visible glass flakes, and should be considered a fingerprint indicator for the loss of glass chemical durability.

Currently, it is impossible to give an absolute indication of what should be the amount of leached elements in the wet solution below which delamination will not occur, as it depends on two main parameters: the glass composition and the formulation of the pharmaceutical product, which is the main driving force for the dissolution mechanism on the inner surface of the container. As better exemplified in previous sections, the interaction mechanisms vary between adsorption of components, exchange mechanisms with glass elements, and dissolution of the glassy network. To conclude, even if glass corrosion is visible or measurable by detection of leached elements in the wet solution, delamination is a very special case of corrosion and depends strongly on the interaction mechanisms of the aggressive pharmaceutical product.

Summarizing, silicate glasses exposed to water can undergo degradation as a result of the action of three mechanisms that can also occur cooperatively: hydration, network hydrolysis and ion exchange reactions. The structure of the glass plays a fundamental role in determining the relative rates of the three mechanisms indicated above. In fact, the observed rates and modalities of dissolution depend mainly on the distribution and reactivity of the various functional groups. The reactivity of each specific site is closely related to the environmental parameters such as solution pH. Depending on the type of bond involved in glass, the rate at which hydrolysation takes place changes considerably. Furthermore, the various reactive sites can be characterized by different charge distributions, such as non-bridging oxygens and tetrahedral borate, thus resulting in distinct ion exchange processes. For all these reasons, it becomes essential to acquire more and more detailed information concerning the local structure of glass and the variation of structure with composition and preparation conditions, in order to predict, and as a consequence to prevent, dissolution behaviours. A fundamental contribution in achieving this goal is given by the XPS technique, as shown in more detail in Section 7.

7. XPS investigation of glass corrosion processes

As shown in Section 6, the chemical composition of the glass surface is influenced by various interactions which occur on the topmost atomic layer. Mechanisms such as leaching, hydration, dissolution, and precipitation are primary factors in establishing long term stability, thus the goal of this Section is to show how XPS, in combination with other methods, can yield a comprehensive characterization of glass leaching and corrosion.

7.1. XPS study of leached glass surfaces

A milestone in the study of leaching behaviour on glass surface performed using XPS is the work of Sprenger and co-workers [141]. The aim of the authors was to show how the composition and the structure of hydrated and leached layers can be analysed quantitatively using XPS. In order to allow for a correct interpretation of XPS signals, a deconvolution procedure wad applied, allowing to resolve the XPS spectra [141,162].

Sprenger and co-workers were able to determine the influence of exposure to vacuo, environmental atmosphere, distilled water, and corrosive media on the surface of different glasses: fused silica (this material was melted from pure quartz Herasil), $Na_2O{\cdot}nSiO_2$ (n = 3, 8) glasses, a $BaO{\cdot}SiO_2$ and a $BaO–B_2O_3–SiO_2$ (Schott SK16) glass. In particular, the O 1s signals of virgin and hydrolysed surface layers of the two former glasses, and leached surface layers of the latter two glasses before and after an additional heating were analysed. To minimize charging effects the surface was flood with low energy electrons. The Au $4f_{7/2}$ peak of metallic gold was chosen as a reference, because leached glass samples may not exhibit a well-defined C 1s peak, hence, a direct calibration in this way may be not possible. In addition, the modified Auger parameter α' was used for accurate measurements of line shifts. The decomposition of the O 1s signal into several components reflects different oxygen bonds. The main results are summarized below.

Fused silica

As a reference, virgin surfaces of Herasil glass rods broken in ultrahigh vacuum were used. The comparison of freshly broken surface and surface broken in UHV and stored for a few hours at 5×10^{-7} Pa is shown in Fig. 23 (a) and (b). With increasing time of storage a carbon contamination on the glass surface could be observed. Increase of up to 1.95 eV in the linewidth and in asymmetry of the O 1s signal can be observed. The spectrum can be resolved in two peaks that can be ascribed to the possible bonds of oxygen to silicon, carbon and hydrogen. However, a reaction with CO or CO_2 can be neglected, since the main component with which the virgin surface can react is H_2O, leading to the formation of silanol groups (SiOH). Therefore, it is reasonable to assume that one of the two peaks in the O 1s signal is associated with the silanol groups. In order to establish which one corresponds to the silanol bond, a silica sample stored in air was studied. The O 1s peak (Fig. 23 (c)) shows an increase in the linewidth up to 2.25 eV and a strong change in the asymmetry at the low binding energy side, indicating an increased intensity of the component on the high BE side. The latter contribution can be ascribed to SiOH. Therefore, the chemical shift of the silanol peak with respect to bridging oxygen is found to be ~0.56 eV.

Sodium silicate glasses

Two sodium silicate glasses $Na_2O{\cdot}nSiO_2$ (n =3, 8) were broken in UHV. XPS spectra show two contributions for the O 1s signal, that can be ascribed to the NBO of the Si–O–Na bond at lower BE and to the BO of Si–O–Si at higher BE. The chemical shift of the BO with respect to the NBO depends on the sodium concentration, confirming the results reported in Section 5.3.

It is well know that corroded alkali silicate glass is characterized by the formation of carbonates on the surface. In these cases the O 1s signal exhibits a broadened linewidth, thus the assignment of components to different oxygen bond is not feasible. With the aim to discern the different bonds, the same sodium silicate glasses were studied after exposure to air for a few days. Due to the formation of new phases it is not possible to distinguish BO from NBO. After deconvolution, reported in Fig. 24, two most intense peaks can be attributed to NBO in silanol groups at higher BE, and to BO in Si–O–Si at lower BE. The small line that appears towards lower BE can be ascribed to the oxygen bond to sodium carbonate (Na_2CO_3). Finally,

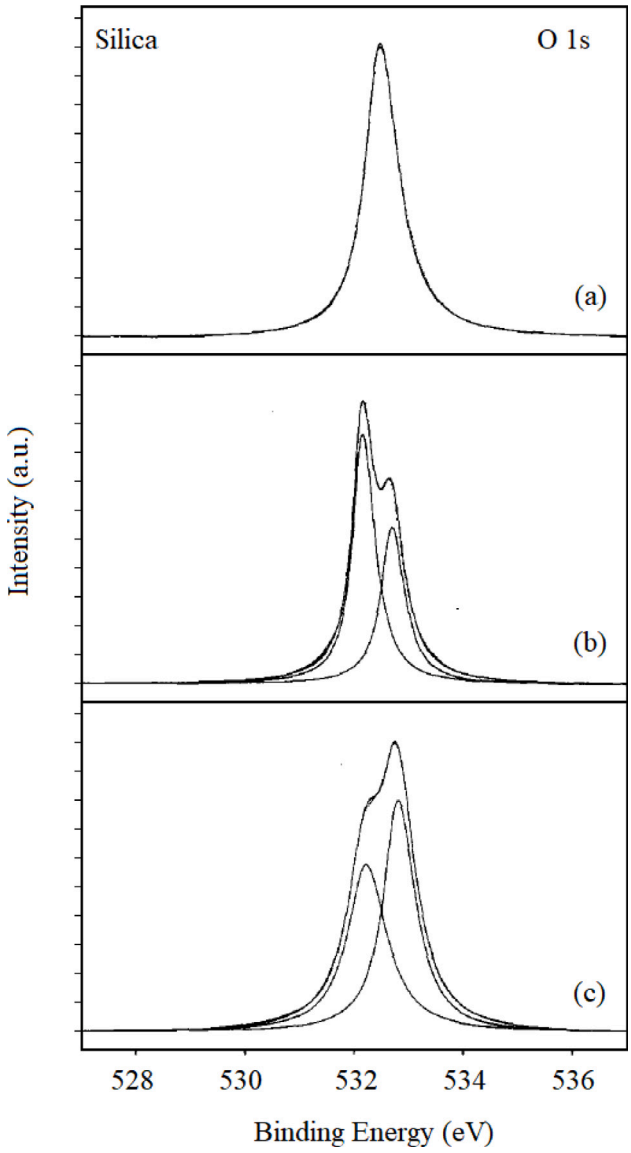

Fig. 23. XPS O 1s spectrum of (a) a freshly broken Herasil glass rod, (b) of a Herasil rod broken in UHV and stored at a pressure of 5×10^{-7} Pa for a few hours, (c) Herasil glass disc corroded at atmosphere. The spectra are shown with the fitted result after deconvolution.
Source: Original data from Ref. [141].

the smaller lines on the low energy side could be related to NBO or sodium hydroxide (NaOH).

$BaO{\cdot}SiO_2$

The surface of this binary silicate glass was leached in distilled water. The authors found that after 10 h of leaching, Ba concentration drops drastically. To establish charge neutralization in the leached layer, some hydrogen should be introduced into the leached layer inducing modified oxygen bonds. When this contribution becomes significant it can be observed in the O 1s signal. Ba ions are characterized by a large ionic radius, as a consequence, after the ion exchange process the network exhibits a porous structure. This porous structure makes possible an easy removal of water by heating the sample.

The deconvolution of O 1s peak after leaching (Fig. 25 (a)) shows several components. For its identification, the leached sample was heated 1 h at 550 °C. After heating, the width of O 1s signal decreased and the asymmetry changed, Fig. 25 (b). Assuming that during heating only oxygen bound to hydrogen (e.g., OH^-, OH_3^- groups and H_2O) could have escaped, both peak have to be ascribed to oxygen bonds which reflect the presence of hydrogen. Thus, the two most intense lines in Fig. 25 (b) correspond to BO (Si–O–Si) (left line) and to SiOH (right line). After heating the removal of silanol groups in not complete. In addition, other silanol groups may be formed again by a reaction with residual gas after the heat treatment. Therefore, it is possible to assign the rightmost line, that disappeared after the heating, to water molecules or hydronium ions. While the other two lines on the left can be ascribed to oxygen in barium carbonate ($BaCO_3$) and barium hydroxide ($Ba(OH)_2$).

$BaO{\cdot}B_2O_3{\cdot}SiO_2$ (SK16)

After leaching SK16 in polish solution (pH = 8.4) for 10 h a complete leaching of Ba and B was observed. The linewidth of the O 1s signal is 2.35 eV. The deconvolution (Fig. 25 (c)) results in two intense lines. Comparing SK16 and $BaO{\cdot}SiO_2$, one can follow the interpretation of Fig. 25 (a): (*i*) the most intense line corresponds to oxygen atoms in silanol groups; (*ii*) the second line represents the BO of the Si–O–Si bond; (*iii*) the line with the highest binding energy corresponds to the oxygen bound in water, which is much smaller than the corresponding line in the leached barium silicate glass. (*iv*) The first and second small lines ascribed to barium hydroxide and barium carbonate have a higher intensity than those from the leached barium silicate glass.

After heating, the O 1s spectrum shows a reduction of the width to 2.25 eV (Fig. 25 (d)). The same change in the asymmetry had been observed in the spectrum of the heated barium silicate glass. The deconvoluted O 1s peaks are also quite similar. The assignment of the lines to the oxygen bonds is the same as mentioned above and needs no additional explanation.

7.2. Data analysis protocol for oxygen speciation

Recently, a data analysis protocol to determine the oxygen speciation on glass surfaces by XPS has been proposed by Banerjee and co-workers [163]. In their work, the surface oxygen speciation was determined using a stoichiometry-based algorithm via elemental composition, instead of the typical O 1s peak-fitting approach. The authors point out that the effect of peak fitting parameters on the results of determining area fractions of Si–O–Si and Si–OH can be misleading. Indeed, they demonstrated that peak fitting with different constraints results in significantly different Si–O–Si and Si-OH fractions. The only prerequisites required by Banerjee et al. for their analysis are the determination of accurate elemental relative sensitivity factors and the correction of adventitious hydrocarbon contamination [18] to achieve the real glass surface composition. They applied this technique to study the effects of acid leaching on the surface sites of commercially available multicomponent E-glass (boron-free, fluorine-free calcium aluminosilicate glass). The leaching of the re-melt surfaces was carried out using a pH 1 solution with HCl at 90 °C for 24 h. The fracture surface was also analysed for comparison. Since surface contamination on multicomponent silicate glasses with alkali and alkaline-earth elements may consist of carbonates together with hydrocarbon species, the carbon and oxygen from the carbonate species were also included in the surface-contamination correction.

Exploiting basic knowledge of standard glass structure and assuming a silicate glass consisting of Q_4 and Q_3 units only (i.e., $Q_4 + Q_3 = 1$) the percentages of BO, NBO and OH were determined using the equations provided below (NF=network formers):

$$\mathrm{BO}\ (at.\%) = \left(\frac{4}{\mathrm{O/NF}} - 1\right) \times \mathrm{O}\ (at.\%), \tag{18}$$

$$(\mathrm{NBO} + \mathrm{OH})\ (at.\%) = \left(2 - \frac{4}{\mathrm{O/NF}}\right) \times \mathrm{O}\ (at.\%), \tag{19}$$

$$\mathrm{NBO}\ (at.\%) = 2\,[\mathrm{Ca}] + 2\,[\mathrm{Mg}] - [\mathrm{Al}] + [\mathrm{Na}] + [\mathrm{K}], \tag{20}$$

$$\mathrm{OH}\ (at.\%) = (\mathrm{OH} + \mathrm{NBO})\ (at.\%) - \mathrm{NBO}\ (at.\%). \tag{21}$$

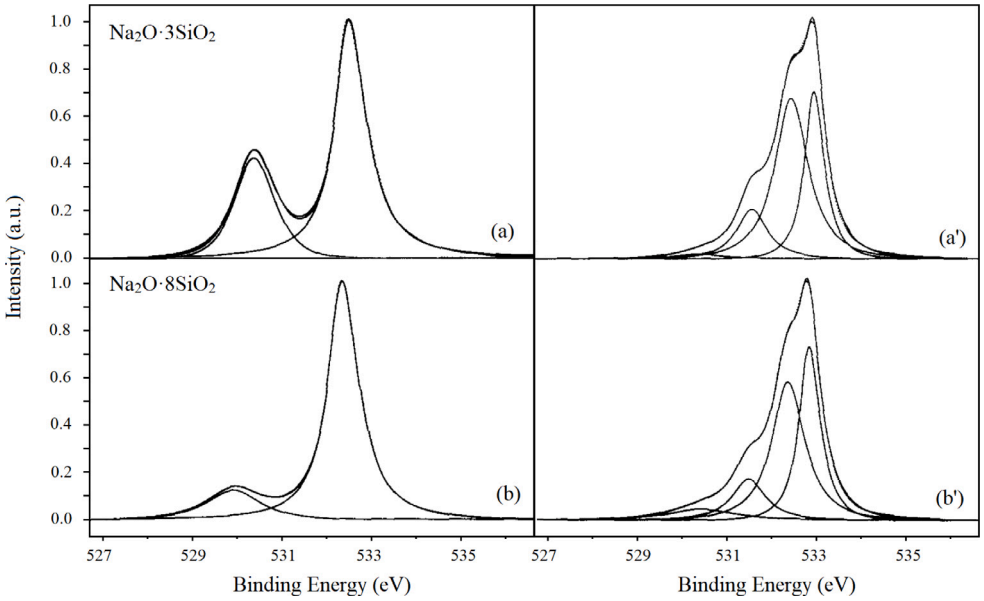

Fig. 24. (a) XPS O 1s spectrum of a $Na_2O{\cdot}3SiO_2$ glass with the fitted result after deconvolution; (b) XPS O 1s spectrum of a $Na_2O{\cdot}8SiO_2$ glass with the fitted result after deconvolution. Deconvoluted and fitted O 1s spectra of (a') $Na_2O{\cdot}3SiO_2$ and (b') $Na_2O{\cdot}8SiO_2$ glass after atmospheric corrosion.
Source: Original data from Ref. [141].

E-glass contains silicon and aluminium as network formers (NF = [Si] + [Al]), if $Al_2O_3M_2O < 1$ (M = Ca, Mg) aluminium is considered to be a network former in the tetrahedral form. While modifiers unassociated with aluminium tetrahedral units are attached to NBOs.

Fig. 26 shows the wide scan XPS spectra in addition to the hydrocarbon-corrected surface compositions of re-melt and leached E-glass. The leached E-glass surface is modifier- and aluminium-deficient, resulting in a silica gel-like surface without NBOs.

A comparison of the distribution of oxygen-based species for fractured, re-melt, and leached E-glass surfaces, is reported in Fig. 27. The oxygen speciation determined using Eqs. (18)-(21) was compared with that obtained by constrained peak fitting of the O 1s photoelectron spectrum. Where the binding energies of BO, NBO, and OH are known to be around 532.5 eV, 531.1 eV, and 533.1 eV, respectively [141] (Fig. 28). Although the components are very close to each other, proper peak fitting can be performed considering the instrumental contribution to the broadening of the peak and component constraints [141,163].

Employing the stoichiometry method it results that the number of NBOs created by modifiers for the fractured and re-melt surfaces are ~15 at.% and ~14 at.%, respectively. It is interesting to note that the fractured and re-melt E-glass surfaces mainly consist of NBO and BO, while the OH species is negligible as Eq. (21) results in <0.3 at.% OH content. The leached glass surface does not contain any NBOs as there are no modifiers left in the leached layer. While, the hydroxyl content is ~10 at.% based on Eq. (21). In addition, there is an increase in BO from ~50 at.% to ~60 at.% upon leaching.

The O 1s spectral peak fits for the fractured, re-melt and leached surfaces are shown in Fig. 28. Note that the O 1s peaks for fractured and re-melt surfaces are comparable. Both surfaces are characterized by two main components: NBO at 531.1 eV and BO at 532.5 eV. More precisely, the E-glass surfaces contain two types of bridging oxygen: BO_1 and BO_2 that are assigned to Si–O–Si and Si–O–Al, respectively. Decoupling of these two components is not feasible, but the broadness of the BO peak can be explained by the presence of the two types of BO components.

The exposure of E-glass to pH=1 acidic solution drastically alters the surface chemistry. After leaching of modifier ions, the NBOs are replaced by silanols. The survey spectrum analysis (Fig. 26) shows the reduction of aluminium in the surface. During the leaching process the complete extraction of aluminium from the glass surface occurs after the hydrolysis of all Al–O–Si linkages. The loss of Al–O–Si linkages on the glass surface results in the formation of silanols groups (Ref. [163] and references). Hence, the O 1s spectrum of the leached glass surface is fit with the BO_1 and SiOH components only [141]. By using as a reference the BO peak location (A), the SiOH component position was fixed at A + 0.55 eV. Moreover, the FWHM of SiOH and BO were kept to be the same [141]. The results reported by Banerjee et al. confirm restructuring of silanols created by ion exchange of cations and loss of aluminium structural units in the leached alkaline-earth aluminosilicate glass surface. Repolymerization within the silicate network is a consequence of condensation between newly created vicinal silanols, resulting in the formation of BO. The fractional oxygen speciation results from the O 1s peak fitting procedure are listed in table inset in Fig. 28.

Water is known to interact strongly with alkali and alkaline-earth multicomponent silicate glasses, as noted earlier in Section 6. For this reason, the authors make sure to highlight the importance of quantifying NBOs to the surface chemistry of the glass as it concerns to the interaction with water molecules and adsorption of other molecules. Furthermore, the quantification of NBO species may also be correlated with surface strength where NBO sites provide failure pathways for corrosion and glass fracture [92]. Additionally, Banerjee et al. point out that the areal density of silanols would affect the adhesion of the coatings because they are chemisorption sites for reactive species in polymeric and organosilane materials. Therefore, it will be critical to determine the number of surface reactive sites to understand surface chemistry as it concerns to adsorption, wetting, and adhesion of materials on glass surfaces.

In the subsequent study conducted by Banerjee and co-workers [164], the compositional changes in unleached and acid-leached commercial soda–lime silicate glass surfaces were tracked with in-vacuo heating and XPS. Since XPS analysis at room temperature alone cannot distinguish surface hydrous species between hydroxyls and water, the presence of surface water leads to an overestimation of hydroxyls and consequent underestimation of bridging oxygen. Banerjee et al. demonstrated that an accurate surface hydroxyl quantification require

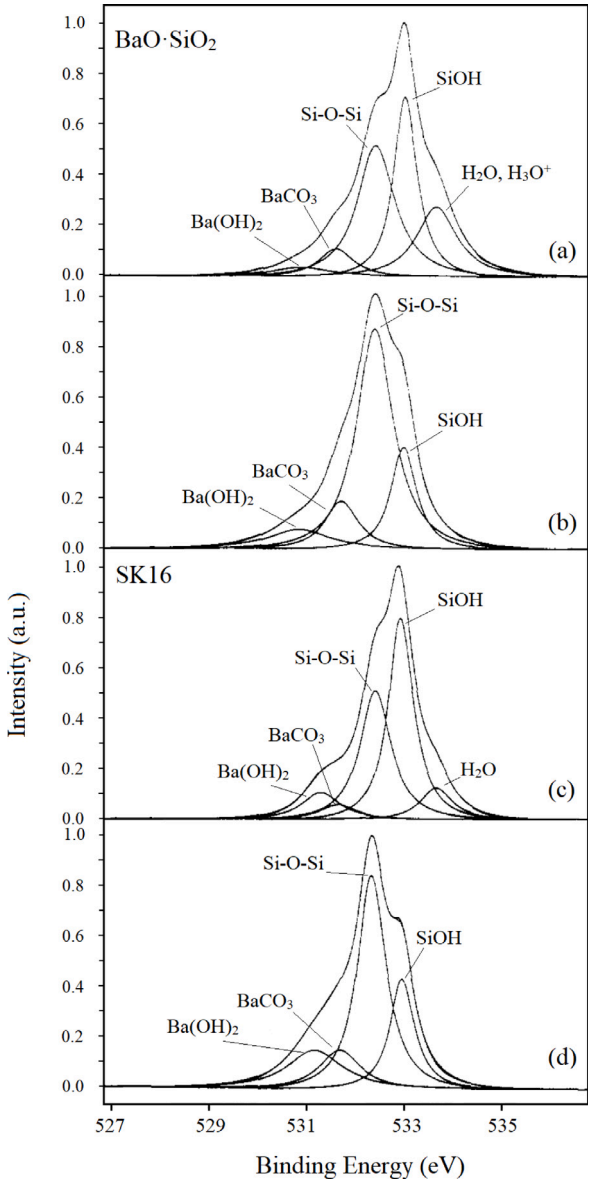

Fig. 25. Deconvoluted and fitted O 1s spectra of $BaO{\cdot}SiO_2$ glass (a) after leaching in distilled water and (b) after an additional heating at 550 °C for 1 h, and (c) the deconvoluted and fitted O 1s spectra of SK 16 glass leached in polish solution and (d) the same glass after an additional heating at 550 °C for 1 h.
Source: Original data from Ref. [141].

dehydration at temperatures near 200 °C. In this work the surface oxygen speciation was established using a stoichiometry-based algorithm where oxygen in hydroxyls (OH) and water molecules (H_2O) were considered to determine the concentration of hydrogen. Therefore, Eq. (21) was substituted by Eq. (22):

$$[OH + H_2O](at.\%) = (-2)\,[O] + [Na] + [K] + 2\,([Ca] + [Mg]) + 4\,[Si] + 3\,[Al]. \quad (22)$$

The concentration of bridging oxygen is then calculated from the mass balance, i.e., the difference between the total oxygen content and the sum of NBO (Eq. (20)) and [OH + H_2O]:

$$BO(at.\%) = [O] - [NBO] - [OH + H_2O]. \quad (23)$$

Fig. 29 shows a comparison between the area-normalized O 1s spectra for unleached and leached glass surfaces at 25 °C, 200 °C, and 500 °C. The authors were able to associate relative changes in the O 1s peak to modifications in oxygen speciation as a function of temperature without the need for curve fitting. The reduction in modifier content on the unleached surface is revealed in the small decrease in Na KLL at 500 °C compared to 25 °C, and in the lower shoulder in the region associated with NBO. Conversely, the change in peak shape in the regions of BO or OH/H_2O is not clear. The leached surface, on the contrary, has a shift in O 1s peak in the direction of the silica peak, indicating a greater concentration of BO. The shift in the spectra due to the increase of BO is accompanied by a consequent reduction in peak intensity at the binding energy range related to hydrous species ($SiOH/H_2O$), due to condensation of hydroxyls, as already suggested in the previous study [163]. The peak shape of O 1s for the unleached glass is broader than the leached glass due to the presence of additional components such as Na KLL, Si–O–Al, and NBO.

Through the oxygen speciation using Eqs. (20), (22) and (23) the temperature-induced changes in surface composition, chemistry and structure for a soda–lime silicate glass, before and after acid leaching can be revealed. The main results achieved by the authors are reported in Fig. 30, where the change in areal density of oxygen speciation as a function of temperature for unleached and leached glass surfaces is shown.

The plots are split into two regimes: dehydration and repolymerization. In the first regime (T < 200 °C), the change in NBO is insignificant while the $SiOH/nm^2$ decreases. Condensation of surface hydroxyls on silica is considered to occur at temperatures above 200 °C [165]. Thus, the decrease in $SiOH/nm^2$ at T < 200 °C is assumed to be due to the dehydration of physisorbed water. In the second regime (T > 200 °C), the increase in BO at temperatures higher than 200 °C suggests repolymerization.

The increase of BO can be observed on the unleached and leached surfaces, however, the mechanisms involved are distinct. On the leached surface, the increase in BO is due to the silanol condensation. This could be attributed to the dehydroxylation of vicinal (hydrogen-bonded) hydroxyls [166,167]. On the contrary, the silanol concentration on the unleached surface remains unchanged at elevated temperatures. More precisely, the second temperature regime of the unleached surface is split into two subregions for changes to the oxygen speciation: (*i*) in the region between 200 °C and 300 °C, no modification in oxygen speciation is observed; (*ii*) above 300 °C, the loss of NBO and the consequent increase in BO could be attributed to the condensation of NBOs to BO upon desorption of modifier ions. The formation of new NBO sites on the leached glass is due to out-diffusion of sodium from the bulk [168,169]. Since its quantity is rather small it is not explicitly evident in the O 1s spectrum of the leached glass at 500 °C in Fig. 29.

The results reported by Banerjee et al. prove the inability of sub-Tg heat treatment on the leached glass to restore the surface to the original condition or to a true silica structure. However, due to the consolidation of the leached surface structure, the authors state again that the structural flaws and pathways for water ingress are reduced, thereby potentially improving corrosion resistance and strength [170, 171]. Furthermore, this work clearly provided evidence that when surface-sensitive techniques such as XPS or SIMS are used to evaluate the areal density of oxygen speciation on the glass surface, a pre-dehydration step is needed to desorb the physisorbed water.

7.3. XPS study on surface wettability

The importance of glass coating has recently grown for a wide range of optical, photovoltaic, and pharmaceutical products. For example, referring to the latter case, coating of the glass prevents the diffusion of ions from the glass and also provides a homogeneous barrier between the glass surface and drug product. Therefore, a comprehensive XPS analysis will be valuable for understanding surface properties which

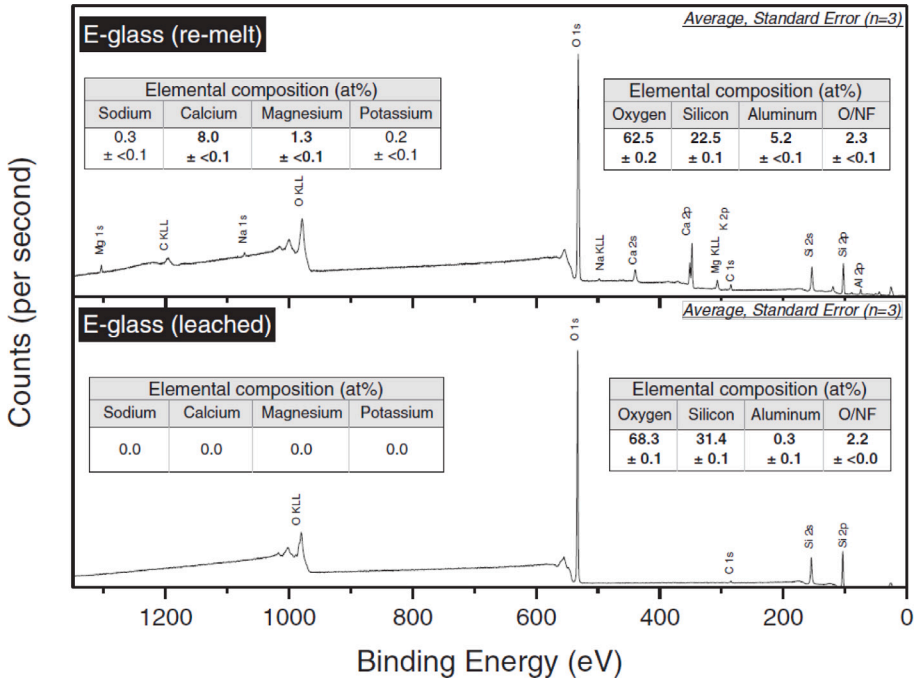

Fig. 26. XPS survey spectra of re-melt and leached E-glass surfaces. The inset table contains the atomic concentration of elements on the E-glass surfaces. The standard error of the mean (n=3) is also included.
Source: Original data from Ref. [163].

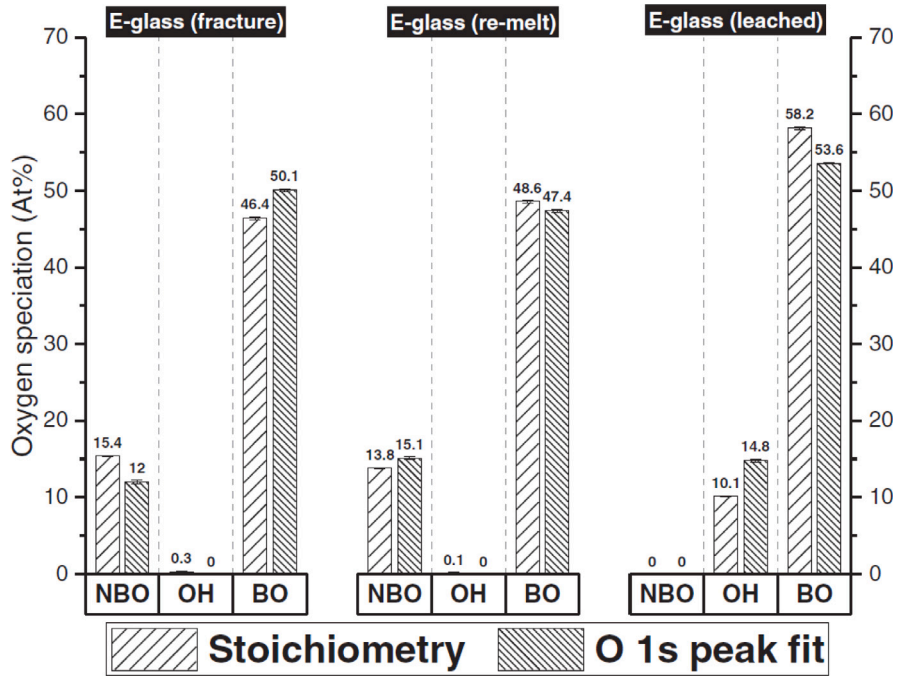

Fig. 27. Speciation of oxygen established by glass stoichiometry and determined using O 1s spectral peak fit for fractured, re-melt and leached E-glass surfaces. Error bars are determined from the standard error of the mean with n=3.
Source: Original data from Ref. [163].

are vital for coating adhesion. A useful example is given by the work of Takeda and co-workers.

Takeda et al. [172] measured the wettability of various commercial glasses to obtain information about the surface states of the glass. The main compositions of these glasses are reported in Table 2.

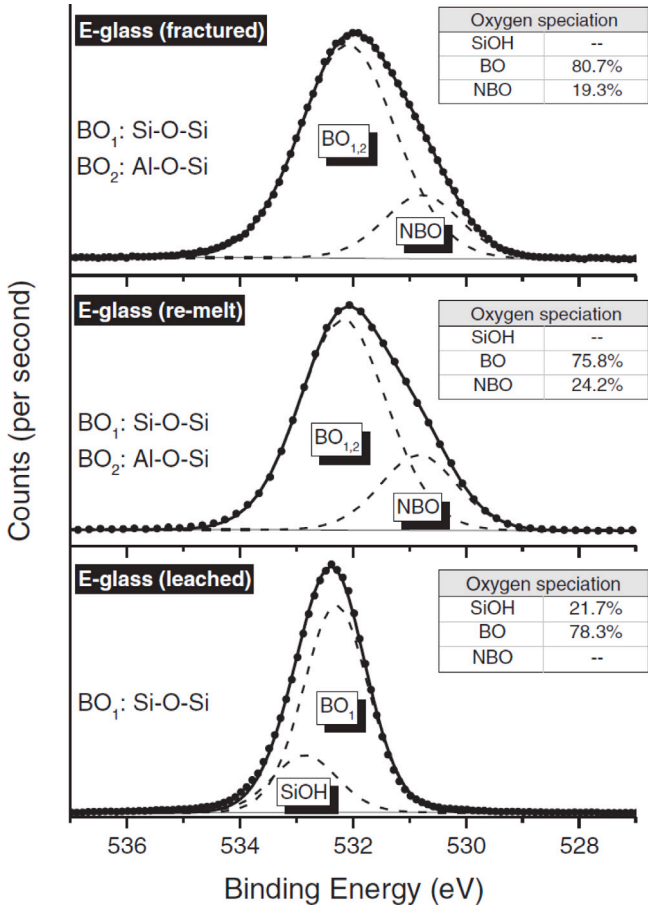

Fig. 28. O 1s spectral peak fit for fractured, re-melt and leached E-glass surfaces with inset tables containing fractional content of SiOH, BO and NBO species.
Source: Original data from Ref. [163].

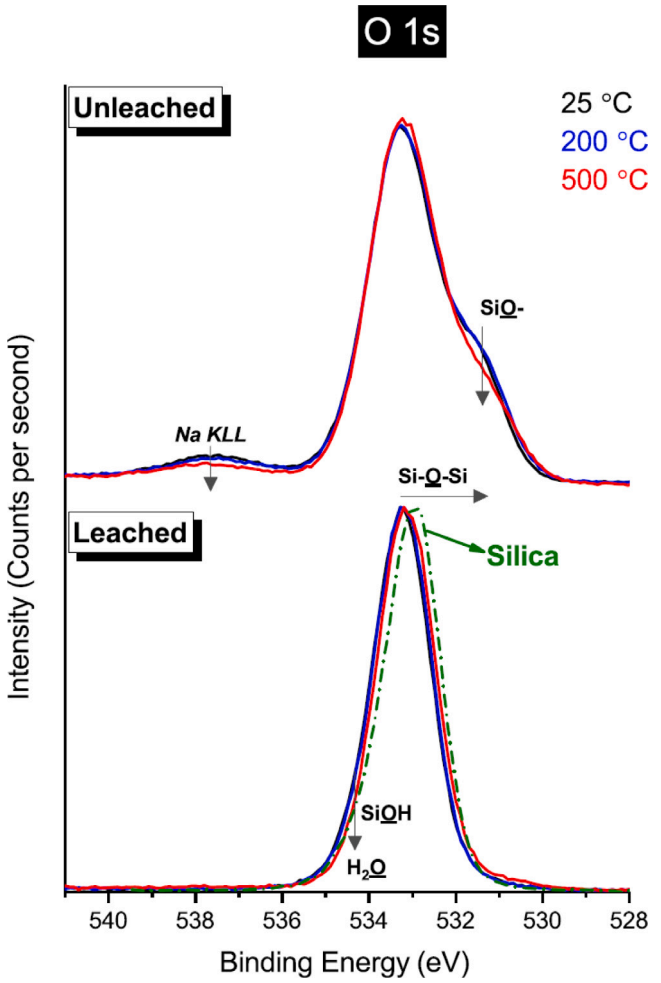

Fig. 29. Representative O 1s spectra for unleached and leached glass at 25 °C, 200 °C and 500 °C. O 1s spectrum of silica is shown in green as a Ref. [164]. (For interpretation of the references to colour in this figure legend, the reader is referred to the web version of this article.)
Source: Original data from Ref. [164].

Table 2
The main compositions of the glasses from Ref. [172].

Sample	SiO_2 (wt.%)	Na_2O (wt.%)	Al_2O_3 (wt.%)	B_2O_3 (wt.%)	Others (wt.%)
soda–lime float	71	13	1.7	–	14.3
Vitreous silica	100	–	–	–	–
Boroaluminosilicate — Type A	49	–	11	15	25
Boroaluminosilicate — Type B	58	–	17	9	16
Boroaluminosilicate — Type C	56	–	11	6	27

The authors examined the relationship between the wettability and the surface OH group density. For this purpose a combination of three complementary analytical techniques was applied, namely, X-ray photoelectron spectroscopy, atomic force microscopy (AFM) and contact angle measurements. The surface cleanliness or the surface state can easily evaluated by measuring the contact angle of water droplets, since this method is highly sensitive to the presence of organic substances. The XPS allows to evaluate the surface OH group density, and to investigate the formation mechanism of surface OH group.

Takeda et al. found that the hydrophobicity, as a consequence of the adsorption of organic substances in the atmosphere, is different among the glasses, and that the origin of the difference can be attributed to the OH group density of the surfaces. The surface OH group density was evaluated by XPS measurements with a chemical labelling technique. In the chemical labelling technique, a fluoroalkyl isocyanate silane was used as the reagent. This material reacts with the surface OH group at room temperature, thus preventing damage to the sample surface. The sample surfaces were cleaned prior to the chemical labelling to remove contaminants. The authors found out that the increase of the contact angle (θ) results from the adsorption of organic substances in the atmosphere, and the difference in the θs is caused by the difference in the amount of the adsorbed organic substances. The contact angle of water droplets is reported in Fig. 31 as a function of elapsed time for various glasses. After cleaning the surface, the contact angles are nearly 0° for all the glasses. Then the contact angles of all the glasses gradually increase with time, up to an asymptotic value that remains constant for a few days.

The authors excluded the possibility that there is a correlation between contact angles and average surface roughness obtained from AFM measurements, and they found that the hydrophobicity depends on the glass. To clarify the origin of this dependence, θ was plotted against the fluorine concentration which mirrors the surface OH group density of the glass, as shown in Fig. 32. The fluorine concentration, obtained from XPS measurements, is different among the glasses, indicating that the surface OH group density depends on the glass. The contact angle θ increases with the increase in the surface fluorine concentration. This fact implies that the surface OH group density is a leading factor that regulates the wettability of the glass surface. The

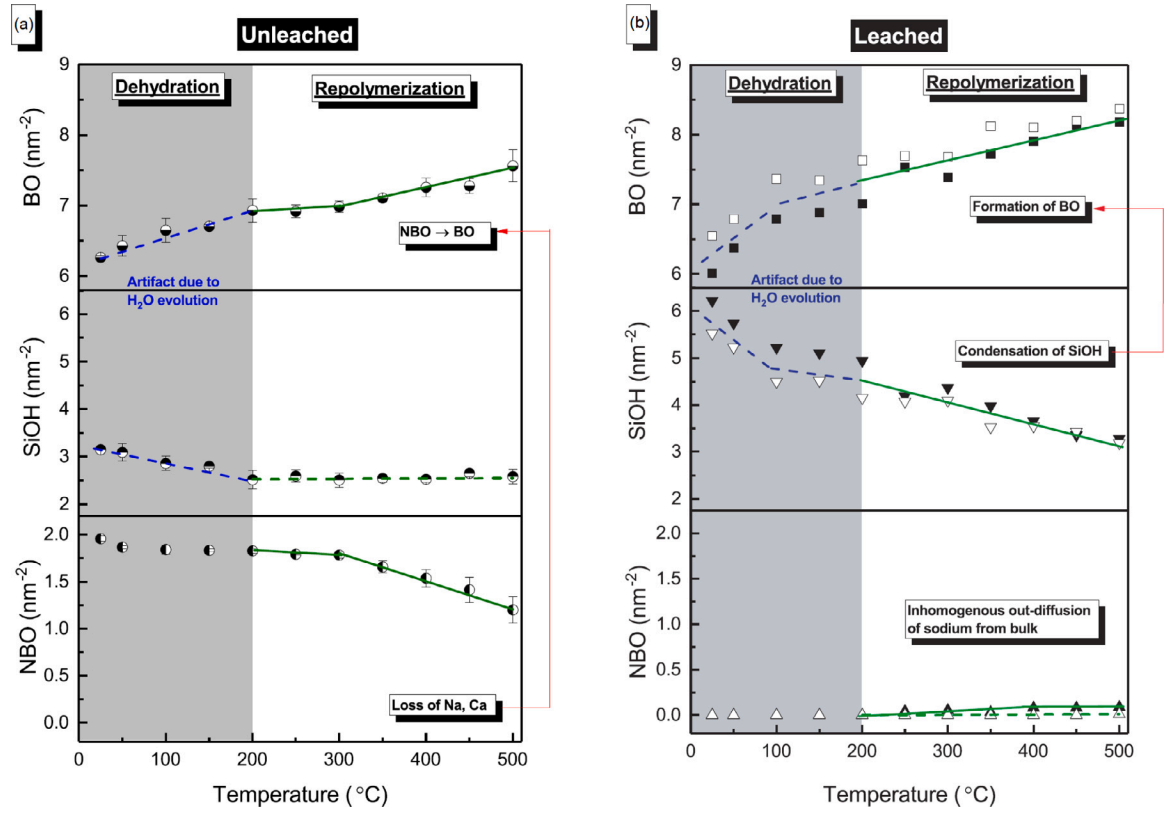

Fig. 30. The areal density of oxygen speciation for unleached (a) and leached (b) glass surfaces as a function of temperature. The results for unleached glass is based on an average/standard deviation of three-spot sampling, whereas results of leached glass are shown for two distinct spots.
Source: Original data from Ref. [164].

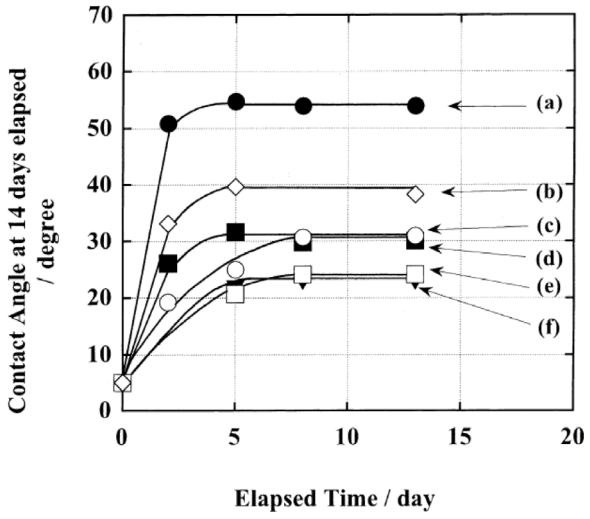

Fig. 31. Changes in contact angle of water droplets for commercial glasses; (a) the tin side of soda–lime float glass, (b) vitreous silica glass, (c) the air side of soda–lime float glass, (d) boroaluminosilicate glass type A, (e) boroaluminosilicate glass type B and (f) boroaluminosilicate glass type C as a function of elapsed time.
Source: Original data from Ref. [172].

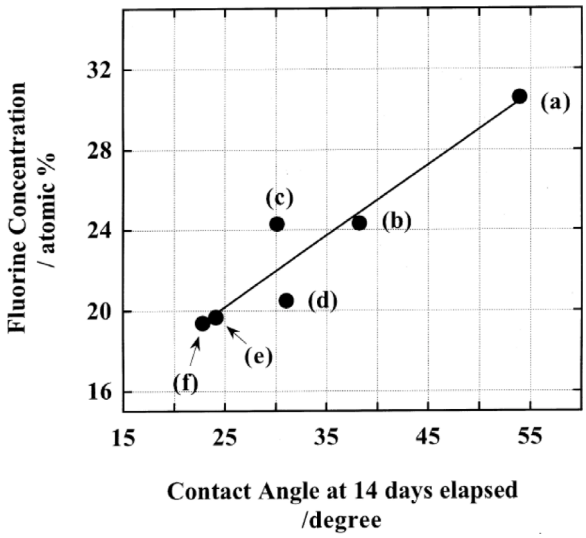

Fig. 32. The relationship between the fluorine concentration obtained from XPS measurements and the contact angle of water droplets at 14 days elapsed; (a) the tin side of soda–lime float glass, (b) vitreous silica glass, (c) the air side of soda–lime float glass, (d) boroaluminosilicate glass type A, (e) boroaluminosilicate glass type B and (f) boroaluminosilicate glass type C.
Source: Original data from Ref. [172].

surface OH group seems to be the key factor for determining the surface properties of glass since it can work as an effective adsorptive site for organic substances. Therefore, controlling the surface OH group density of glass surface is very important in order to manufacture high-quality glass products coated with thin films.

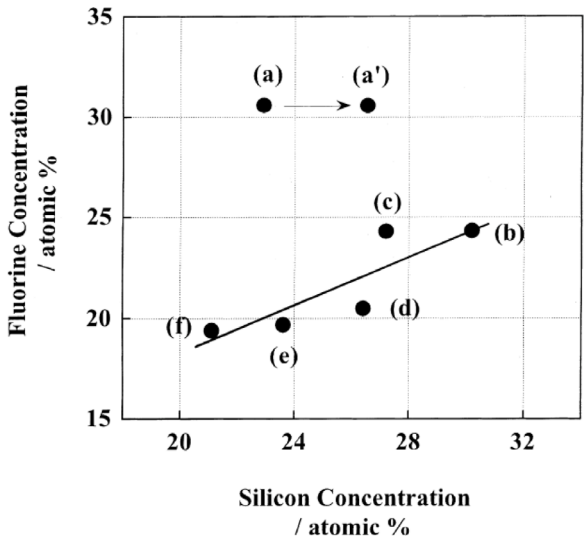

Fig. 33. The relationship between the fluorine and silicon concentration obtained from XPS measurements; (a) the tin side of soda–lime float glass, (b) vitreous silica glass, (c) the air side of soda–lime float glass, (d) boroaluminosilicate glass type A, (e) boroaluminosilicate glass type B, (f) boroaluminosilicate glass type C and (a') the value of (Si + Sn) atomic concentration of the tin side of soda–lime float glass.
Source: Original data from Ref. [172].

In Fig. 33, the silicon concentration of the surface obtained from XPS measurements is plotted against the fluorine concentration. It is interesting to note that there is a linear correlation between the silicon concentration and the fluorine concentration, except for the tin side of the soda–lime float glass. This result demonstrates that the surface OH group density depends on the surface silicon concentration, and the majority of the surface OH groups are silanol (SiOH) groups. The surface OH group density of the tin side of the soda–lime float glass is greater than the other glasses measured. In this case, the contribution of SnOH group has to be considered, since it works as an effective adsorptive or reactive site for substances. Note that SnOH group density is not simply dependent on the tin concentration.

Takeda's work highlights once again the valuable contribution provided by the XPS technique for understanding the properties of glass surfaces.

7.4. Depth profiling by XPS for corroded glass

The analysis of altered surface are important to evaluate the chemical durability of glass. In particular, information about depth profiles is helpful in the investigation of the mechanism of leaching process and to estimate the leaching behaviour for long periods.

One of the first works where XPS combined with Ar ion sputtering was employed for the evaluation of corroded glass surface is that of Yamanaka et al. [71]. To measure the etching rate of Ar ion sputtering, samples of commercial silicate glass and samples of float glass were used. In this study the authors compared a leached glass surface with untreated glass. For the silicate glass, the area of each peak was normalized by the correspondent value measured on the unsputtered glass surface. The changes in the relative area of each element peak are reported in Fig. 34 (a) as a function of sputtering time. It is interesting to note that the decrease of Na concentration is similar to that observed in the other silicate glasses (Ref. [71] and references).

The depth profiles measured for the tin side of float sheet glass before and after leaching treatment at 94 °C for 5 h are reported in Fig. 34 (b). Since this treatment was in the initial stage of leaching and the glass alteration was not significant enough to change the etching rate relative to the untreated specimen. In order to distinguish the leaching effect from the sputtering effect, both leached glass and untreated glass were sputtered and the peak areas for the same sputtering times were compared. Hence, Fig. 34 (b) shows the peak area ratio of the leached glass to untreated glass as a function of sputtering time. Note that Si is concentrated in the surface, while Na, Ca and Sn are decreased relative to an untreated sample. Sn has originally a depressed profile in float glass surface and this is reflected in the rapidly decrease of peak area in the leached surface. However, the ratio of treated to untreated glass increases, showing that the leaching effect on Sn extended to the depth achieved by 1 h sputtering, which is estimated at 50 nm. Although the changes of Si, Ca and Sn concentrations increase until a stable value within approximately 1 h of sputtering time, while depletion of Na continued to 2 h sputtering. These results are consistent with the selective leaching, and this supports the assumption that the intensity ratio of leached glass to untreated glass could represent the relative composition change. Yamanaka et al. thus demonstrated the efficacy of Ar sputtering to obtain depth profiles even for alkali containing glasses.

In a more recent study of Reiß and co-workers [173], Ar sputtering was used to investigate the initial mechanisms of glass degradation of toughened and not toughened soda–lime–silica float glasses, and the influence of post-production glass toughening. A set of samples of float glass before and after thermal and chemical strengthening were analysed. In addition, the samples were exposed to artificial weathering in a climate chamber, its parameters were set at 80 °C and 80% relative humidity. The glasses were stored under these conditions for one, three and seven days, respectively. Then all the sample sets were investigated by optical microscopy, atomic force microscopy and X-ray photoelectron spectroscopy. All tests and characterizations were performed on the air side of samples. The comparison between XPS depth profiles measured before and after simulated weathering in untreated glasses and chemically strengthened glasses are of particular interest. The following nomenclature for the samples is used: the names indicate the pretreatment together with the duration of artificial weathering, e.g. Ref7 is the untoughened reference sample that was artificially weathered for seven days, while Chem1 is a chemical toughened glass that was stored for one day in the climate chamber.

XPS was used for a detailed chemical analysis of the glass surfaces and depth profiling. Depth profiles were generated by repeated sputtering and measuring cycles. The spectra were calibrated to the C 1s peak at 284.6 eV caused by carbon adsorbates. The removed material thickness was estimated from the number of sputter cycles. However, due to differences in their structure and chemical composition the sputter rates of the outermost surface layers may be different from the bulk. Effects of preferential sputtering may also occur, nevertheless, the authors assumed that the sputtering rate for comparable layer compositions of different samples should not differ significantly.

Depth profiles of untreated float glass

The depth profiles of the reference sample set are shown in Fig. 35 (left). In case of the untreated reference sample Ref0, the Na concentration drops from initially 9.1 to 3.6 at.% and then re-increases until a stable value of 7.6 at.% after 60 sputter cycles. The Mg and Ca concentration are about 1 and 2 at.% at the glass surface and increase while sputtering almost linearly until they stabilize at concentration of 7.1 and 5.6 at.%, respectively. Because of the low concentration of Na, Mg and Ca in the surface region the relative amount of Si and O are slightly higher in this zone than in the deeper layers. The C found on the surface vanishes already after the first sputter process.

As a result of the artificial weathering, the depth profiles show strong variation compared to Ref0, and these changes become more and more evident as the days in the climate chamber increase. C and Na concentration are increased in the surface region, and progressively enhance with the duration of simulated weathering. After the initial increase, the Na profile shows a depletion zone, then the Na concentration increases again, while the C signal continues to decline until it is no longer detected. The Mg concentration increases in the surface

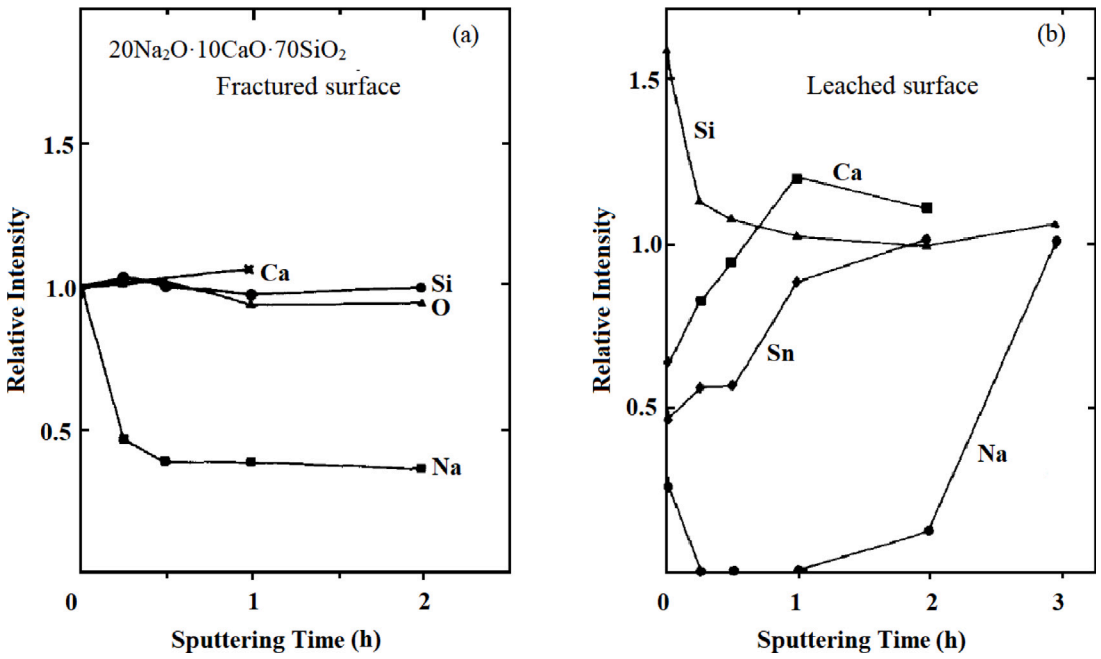

Fig. 34. (a) Peak area normalized by unsputtered surface of soda–lime silicate glass versus sputtering time. (b) Peak area ratio of the tin side of the float glass surface treated at 94 °C for 5 h to untreated glass as a function of sputtering time.
Source: Original data from Ref. [71].

region as well, and the development of a pronounced Mg enrichment can be observed in Ref7. Afterwards, the concentration declines and increases slightly after 100 sputter cycles. Significant changes of the Ca-profile in comparison to Ref0 cannot be seen in Ref1. While in Ref3 (not shown) and Ref7, Ca in the surface region is drastically enhanced, then its concentration declines slowly.

Depth profiles of chemical toughened glass

The depth profiles of the chemical toughened glass are reported in Fig. 35 (right). In consequence of the toughening process the glass underwent when it was produced, K can be found in the depth profiles. Its concentration at the surface of the unweathered air side is about 3.8 at.% and in a depth of 27.6 nm (120 sputter cycles) ~5 at.%.

The depth profiles of sample Chem0 are rather similar to the corresponding depth profiles of the reference glass sample Ref0. A slightly higher concentration of C of the unsputtered surface of sample Chem0 can be observed. Its concentration drops immediately after the first sputter process and after 10 sputter cycles C is not detectable. Mg increases from initially 2.6 to constant 6.4 at.% during the first 50 sputter cycles. Na drops from 1.7 at.% at the surface to 0.8 at.% after eight sputter cycles and subsequently re-increases to ~3 at.% after a further 90 cycles. The Ca-profile increases from initially 3.5 to 8.7 at.%. After 35 sputter cycles it starts to drop slowly until a stable concentration of about 6 at.% is reached (after 85 sputter cycles) and its profile becomes parallel to the Mg one.

For all weathered samples an increase in the concentrations of all elements, except Si and O, in the outermost surface region is observed. The amount of accumulated C, Na and Mg in the surface region increases with the days of artificial weathering. C concentration decreases during the first 25 sputter cycle; Mg in Chem1 drops afterwards to a minimum (after 20 sputter processes) and then re-increases to a stable value after 45 sputter cycles. While in Chem3 (not shown), the local minimum in the propagation of the Mg concentration profile is found deeper in the glass. Similar to Mg, K in sample Chem7 develops a slight intermediate maximum (15 sputter cycles) and minimum (45 sputter cycles). The depth profile of sample Chem7 is nearly identical to the one of Chem3 (not shown). Only the Ca and Na concentration in the surface region are slightly higher.

The implications of these findings are thus discussed below.

Untreated glass

Na exhibits a pronounced tendency to diffuse towards the glass surface due to its high mobility (Ref. [173] and references). The high temperature of 80 °C in the climate chamber further increases this diffusion resulting in an increasing Na accumulation on the surface of the air side over a period of seven days. In the literature it is assumed that these accumulated Na species react with C and hence form carbonate phases. The Na:C ratio is 1 in Ref7, thus suggesting the presence of a sodium bicarbonate ($NaHCO_3$) layer which is several nm thick [174].

Another peculiarity that the depth profiles of the untreated reference glass exhibit is the concentration progression of Mg. Its concentration increases significantly in the surface region during the artificial weathering. Mg enrichment is followed by a significant depletion layer before to increase again. The depth profiles presented here denote a certain mobility for Mg in the outer glass layers, despite Mg is generally assumed to be resistant to diffusion (Ref. [173] and references). The depletion zone that follows the Mg enrichment suggests that only a few Mg species from the deeper glass layers can be provided. Therefore, the lack of further mobile Mg species from the lower layers leads to an increase in the relative concentration of Na, giving rise to the intermediate maximum of sodium observed in Ref3 (not shown) and Ref7 (Fig. 35). The Na enrichment ends at the same point where the Mg depletion also ends. Afterwards, both element concentrations and those of the other glass components are stable. The diffusion behaviour of Mg might be related to the strong Na enrichment in the surface region of the glass. Indeed, when the amount of network modifiers, such as Na^+ and Ca^{2+}, is high then Mg has the coordination number of 4 and acts as a network former (Ref. [173] and references). If the proportion of Ca and Na decreases, these ions are not available for the charge compensation that guarantees the stabilization of Mg^{2+} ions. Hence, Mg can no longer act as a network former, and it becomes a network modifier with the coordination number 6. Furthermore, the more network modifiers are present in a glass, the more the glass network is loosened up (Ref. [173] and references).

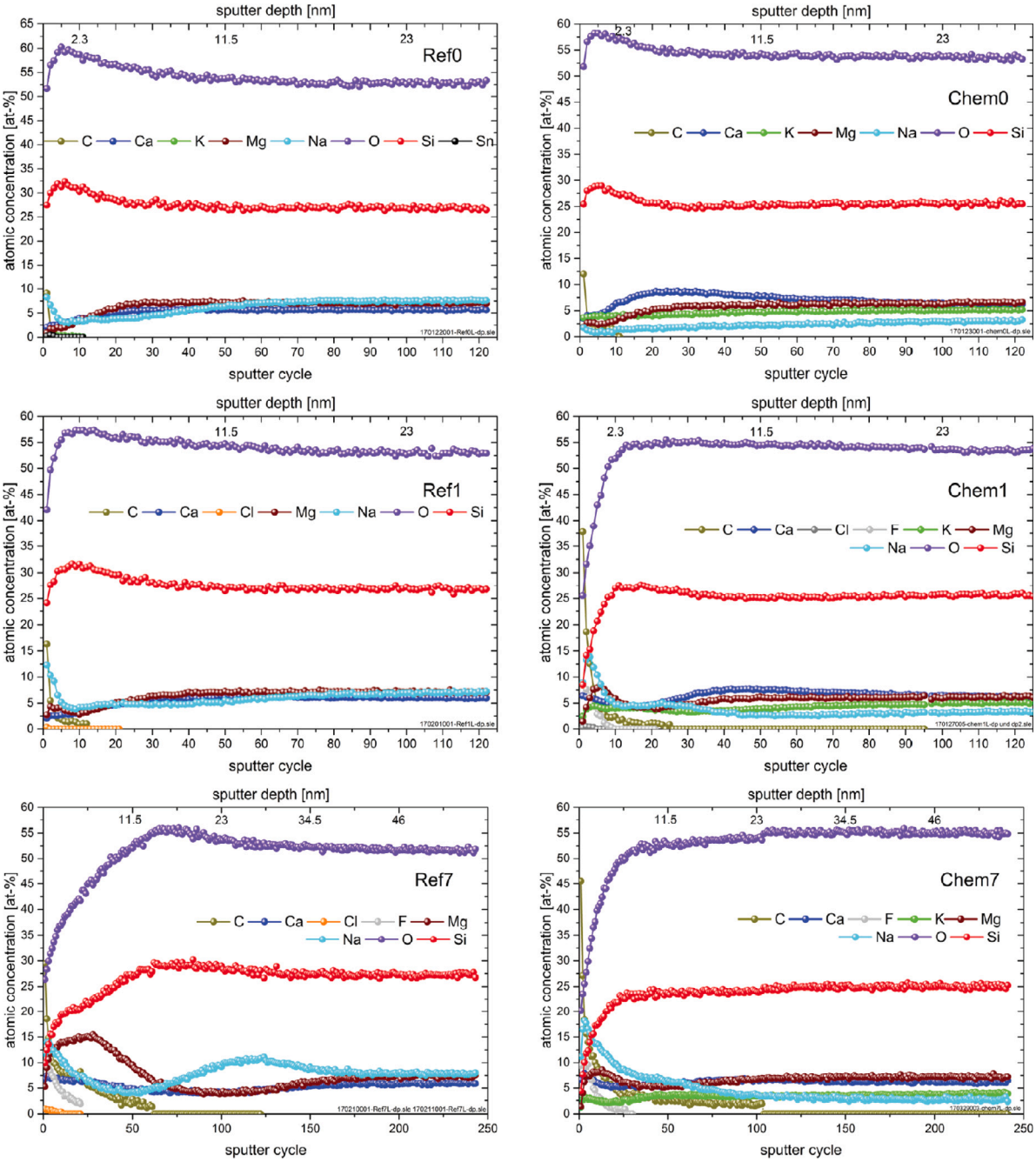

Fig. 35. Depth profiles of the air sides of normal (left) and chemical toughened (right) float glass. The samples were sputtered until stable element concentrations were reached. 10 sputter cycles equal a depth of 2.3 nm. The duration of artificial weathering is given by the sample names.
Source: Original data from Ref. [173].

The weather induced accumulation of Na ions in the glass surface should therefore result in a less connective glass network in this area. This allows the less mobile and larger Ca ions to diffuse towards the surface, explaining why in the recorded depth profiles the Na enrichment starts earlier than the Ca accumulation. When Ca begins to diffuse towards the glass surface as well, Na and Ca species begin to lack and Mg becomes a network modifier, as mentioned above. Consequently, its mobility increases, resulting in its accumulation near the glass surface. Because a high amount of Mg^{2+} can lead to a contraction of the glass network due to its high binding strength [173], the further diffusion of Ca and Mg from deeper glass layers into the surface zone is inhibited, and the proportion of Na and Ca in the deeper glass layers remains almost unchanged, leaving Mg a fixed network former. This leads to the formation of a Ca and Mg depletion zone in the depth profile, where the Mg curve runs almost identically with that of the Ca into the glass bulk. The maximum Mg concentration is not located in the outermost surface layers, unlike Na and Ca, but up to 4 nm below. This might be explained by the concentration of network modifiers on the glass surface which is so high that Mg gets the coordination number 4 and thus it is immobile again so it cannot reach the outermost surface layers.

The model proposed by Reiß et al. to explain the ions diffusion process can be applied on unweathered and weathered samples, since

the degradation in the latter case is at an early stage, therefore an adequate explanation for the first subsurface changes is given by the authors.

Chemically toughened glasses

Thanks to the optical microscope and AFM images the authors were able to notice the evident differences between the weathered air sides of the chemically toughened glasses, from those of the reference sample set, which gives an initial indication of a different water attack.

The depth profiles of the unweathered chemically toughened glasses are very similar to those of the reference glasses. Conversely, the depth profiles of the weathered chemically toughened glasses differ significantly from the others. Due to the high temperature in the climate chamber, the Na concentration shows a maximum in the surface region, while the fluctuation in Mg profile is less pronounced compared to the reference samples. While after seven days of artificial weathering all elements of the untreated glasses stabilize after a depth of ~40 nm, the chemically strengthened glass exhibits constant element concentrations from a shallower depth.

The chemically toughened glass proved to be more resistant to chemical changes in the vertical direction. This leads to the conclusion that the attack on chemically toughened glass is different. A reasonable explanation given by the authors is that during ion exchange process a change of the glass structure occurred. Since the K ions entering into the glass are about 30% larger than the exchanged Na ions, the integration of K into the glass network reduces the interstitial spaces within the glass network, which may make it more difficult for water species to penetrate the glass network and hence mitigates the corrosive attack in deeper glass layers. While no meaningful change in the depth was detected in chemical toughened glasses over a weathering time of seven days, the lateral changes in the surface are actually more severe compared to the other sample set. A much higher precipitation rate as well as a significant more inhomogeneous distribution of forming crystals was observed. Hence, its lateral corrosion resistance seems to be less than for untreated glasses. A possible explanation lies in the different radius of K^+ ions. It is well known that K^+ can be detached easily than Na^+ because of its lower bonding energy originating from the higher ionic radii. Thus, leaching rate of the K^+ is reported to be faster than Na^+ [175].

Due to the varying degrees of lateral and vertical chemical changes of a glass surface during weathering, Reißet al. raise the question of what criteria should be used to judge the corrosion resistance of a glass. Moreover, depending on the glass application one can be more concerned with lateral than vertical degradation.

8. Conclusions

The main purpose of this review was to highlight the importance, in the study of glass surfaces, of using analysis techniques able to give information about both the concentration and the chemical bonds of the different elements present in the first few nanometres of the surface, where the physical–chemical effects of the interaction with the surrounding environment are particularly marked. In this frame the XPS technique (also called ESCA) is able to provide interesting possibilities, even more marked with the recent improvements of the needed accessories of laboratory instruments, such as ion guns for controlled sputtering and surface charging control systems. Although the information needed to best characterize a surface (glassy or not) still requires a multi-technical approach, we wanted to underline the great potential of the XPS technique, in particular in the field of glassy materials, in which its application has always been rather limited compared to the information attainable. Our hope is that the brief description we have reported of the technique as well as some recent interesting applications described will help researchers interested to approach the study of glass surfaces.

Declaration of competing interest

The authors declare that they have no known competing financial interests or personal relationships that could have appeared to influence the work reported in this paper.

Acknowledgements

I (E.C.) want to warmly thank prof. Renzo Bertoncello (University of Padua, Italy), now retired, for teaching me a lot about the XPS technique and the related scientific experimental approach since the 90 s, during my degree and doctoral theses: I want to dedicate this review to him.

References

[1] H. Hertz, Über einen Einfluss des ultravioletten Lichtes auf die elektrische Entladung, Ann. Physik 31 (1887) 983–1000.
[2] A. Einstein, Über einen die Erzeugung und Verwandlung des Lichtes Betreffenden Heuristischen Gesichtspunkt, Ann. Physik 17 (1905) 132–148.
[3] K. Siegbahn, C. Nordling, R. Fahlman, K. Hamrin, J. Hedman, T. Johansson, S.-E. Karlsson, I. Lindgren., B. Lindberg, ESCA, atomic, molecular and solid state structure studied by means of electron spectroscopy, in: Almqvist, Wiksell (Eds.), in: Ser. IV, vol. 20, Nova Acta Regiae Soc. Sci. Upsaliensis, 1967.
[4] M. Burrell, Chemical analysis, electron spectroscopy, in: Encyclopedia of Materials: Science and Technology, Elsevier, 2001, pp. 1142–1149, http://dx.doi.org/10.1016/B0-08-043152-6/00214-X.
[5] F.A. Stevie, C.L. Donley, Introduction to X-ray photoelectron spectroscopy, J. Vac. Sci. Technol. A. 38 (2020) 063204, http://dx.doi.org/10.1116/6.0000412.
[6] C.D. Wagner, A.V. Naumkin, A. Kraut-Vass, J.W. Allison, C.J. Powell, J.J. Rumble, NIST X-ray Photoelectron spectroscopy database, 2012, URL http://srdata.nist.gov/xps/.
[7] M.P. Seah, W.A. Dench, Quantitative electron spectroscopy of surfaces: A standard data base for electron inelastic mean free paths in solids, Surf. Interface Anal. 1 (1979) 2–11, http://dx.doi.org/10.1002/sia.740010103.
[8] C.J. Powell, Practical guide for inelastic mean free paths, effective attenuation lengths, mean escape depths, and information depths in x-ray photoelectron spectroscopy, J. Vac. Sci. Technol. A. 38 (2020) 023209, http://dx.doi.org/10.1116/1.5141079.
[9] Application note: 31014 - angle resolved XPS, Thermo Sci. (2008).
[10] H.W. Nesbitt, G.M. Bancroft, High resolution core- and valence-level XPS studies of the properties (structural, chemical and bonding) of silicate minerals and glasses, Rev. Mineral. Geochem. 78 (2014) 271–329, http://dx.doi.org/10.2138/rmg.2014.78.7.
[11] G.M. Bancroft, H.W. Nesbitt, R. Ho, D.M. Shaw, J.S. Tse, M.C. Biesinger, Toward a comprehensive understanding of solid-state core-level xps linewidths: Experimental and theoretical studies on the Si2p and O1s linewidths in silicates, Phys. Rev. B. 80 (2009) 1–13, http://dx.doi.org/10.1103/PhysRevB.80.075405.
[12] M.C. Biesinger, Advanced analysis of copper X-ray photoelectron spectra, Surf. Interface Anal. 49 (2017) 1325–1334, http://dx.doi.org/10.1002/sia.6239.
[13] D.R. Baer, K. Artyushkova, C. Richard Brundle, J.E. Castle, M.H. Engelhard, K.J. Gaskell, J.T. Grant, R.T. Haasch, M.R. Linford, C.J. Powell, A.G. Shard, P.M.A. Sherwood, V.S. Smentkowski, Practical guides for x-ray photoelectron spectroscopy: First steps in planning, conducting, and reporting XPS measurements, J. Vac. Sci. Technol. A. 37 (2019) 031401, http://dx.doi.org/10.1116/1.5065501.
[14] C. Wagner, Sensitivity factors for XPS analysis of surface atoms, J. Electron Spectros. Relat. Phenomena 32 (1983) 99–102, http://dx.doi.org/10.1016/0368-2048(83)85087-7.
[15] G. Greczynski, L. Hultman, Reliable determination of chemical state in x-ray photoelectron spectroscopy based on sample-work-function referencing to adventitious carbon: Resolving the myth of apparent constant binding energy of the C 1s peak, Appl. Surf. Sci. 451 (2018) 99–103, http://dx.doi.org/10.1016/j.apsusc.2018.04.226.
[16] D.A. Shirley, High-resolution X-Ray photoemission spectrum of the valence bands of gold, Phys. Rev. B 5 (1972) 4709–4714, http://dx.doi.org/10.1103/PhysRevB.5.4709.
[17] S. Tougaard, Practical algorithm for background subtraction, Surf. Sci. 216 (1989) 343–360, http://dx.doi.org/10.1016/0039-6028(89)90380-4.
[18] G.C. Smith, Evaluation of a simple correction for the hydrocarbon contamination layer in quantitative surface analysis by XPS, J. Electron Spectros. Relat. Phenomena 148 (2005) 21–28, http://dx.doi.org/10.1016/j.elspec.2005.02.004.
[19] J.F. Watts, J. Wolstenholme, an Introduction To Surface Analysis By XPS and AES, John Wiley & Sons, Ltd, Chichester, UK, 2003, http://dx.doi.org/10.1002/0470867930.

[20] W.P. Dianis, J.E. Lester, External standards in X-Ray photoelectron spectroscopy a comparison of gold, carbon, and molybdenum trioxide, Anal. Chem. 45 (1973) 1416–1420, http://dx.doi.org/10.1021/ac60330a037.

[21] C.E. Bryson, Surface potential control in XPS, Sur. Sci. 189–190 (1987) 50–58, http://dx.doi.org/10.1016/S0039-6028(87)80414-4.

[22] J.B. Metson, Charge compensation and binding energy referencing in XPS analysis, Surf. Interface Anal. 27 (1999) 1069–1072, http://dx.doi.org/10.1002/(SICI)1096-9918(199912)27:12<1069::AID-SIA677>3.0.CO;2-A.

[23] D.R. Baer, M.H. Engelhard, D.J. Gaspar, A.S. Lea, C.F.J. Windisch, Use and limitations of electron flood gun control of surface potential during XPS: two non-homogeneous sample types, Surf. Interface Anal. 33 (2002) 781–790, http://dx.doi.org/10.1002/sia.1454.

[24] G. Vereecke, P.G. Rouxhet, Surface charging of insulating samples in x-ray photoelectron spectroscopy, Surf. Interface Anal. 26 (1998) 490–497, http://dx.doi.org/10.1002/(SICI)1096-9918(199806)26:7<490::AID-SIA392>3.0.CO;2-U.

[25] D.R. Baer, K. Artyushkova, H. Cohen, C.D. Easton, M. Engelhard, T.R. Gengenbach, G. Greczynski, P. Mack, D.J. Morgan, A. Roberts, XPS Guide: Charge neutralization and binding energy referencing for insulating samples, J. Vac. Sci. Techn. 38 (2020) 031204, http://dx.doi.org/10.1116/6.0000057.

[26] ASTM E1523-15, Standard guide to charge control and charge referencing techniques in X-Ray photoelectron spectroscopy, 2015, URL https://www.astm.org/Standards/E1523.htm.

[27] J. Cazaux, Mechanisms of charging in electron spectroscopy, J. Electron Spectros. Relat. Phenomena 105 (1999) 155–185, http://dx.doi.org/10.1016/S0368-2048(99)00068-7.

[28] J. Cazaux, About the charge compensation of insulating samples in XPS, J. Electron Spectros. Relat. Phenomena 113 (2000) 15–33, http://dx.doi.org/10.1016/S0368-2048(00)00190-0.

[29] A.J. Pertsin, Y.M. Pashunin, Differential charging in XPS studies of polymer/metal interfaces, Appl. Surf. Sci. 44 (1990) 171–178, http://dx.doi.org/10.1016/0169-4332(90)90047-4.

[30] I. Doron-Mor, A. Hatzor, A. Vaskevich, T. van der Boom-Moav, A. Shanzer, I. Rubinstein, H. Cohen, Controlled surface charging as a depth-profiling probe for mesoscopic layers, Nature 406 (2000) 382–385, http://dx.doi.org/10.1038/35019025.

[31] S. Suzer, Differential charging in X-ray photoelectron spectroscopy: A nuisance or a useful tool? Anal. Chem. 75 (2003) 7026–7029, http://dx.doi.org/10.1021/ac034823t.

[32] P.M.A. Sherwood, Exploiting differential sample charging in X-ray photoelectron spectroscopy, Surf. Sci. 600 (2006) 771–772, http://dx.doi.org/10.1016/j.susc.2005.11.025.

[33] X. Yu, H. Hantsche, Some aspects of the charging effect in monochromatized focused XPS, Fresenius. J. Anal. Chem. 346 (1993) 233–236, http://dx.doi.org/10.1007/BF00321421.

[34] T.L. Barr, Studies in differential charging, J. Vac. Sci. Technol. A Vacuum Surfaces Film. 7 (1989) 1677–1683, http://dx.doi.org/10.1116/1.576069.

[35] G. Beamson, A. Bunn, D. Briggs, High-resolution monochromated XPS of poly(methyl methacrylate) thin films on a conducting substrate, Surf. Interface Anal. 17 (1991) 105–115, http://dx.doi.org/10.1002/sia.740170206.

[36] B.J. Tielsch, J.E. Fulghum, Differential charging in xps. Part I: Demonstration of lateral charging in a bulk insulator using imaging XPS, Surf. Interface Anal. 24 (1996) 28–33, http://dx.doi.org/10.1002/(SICI)1096-9918(199601)24:1<28::AID-SIA66>3.0.CO;2-G.

[37] W.M. Lau, Use of surface charging in xray photoelectron spectroscopic studies of ultrathin dielectric films on semiconductors use of surface charging in x-ray photoelectron spectroscopic studies of ultrathin dielectric films on semiconductors, Appl. Phys. Lett. 54 (1989) 338–340, http://dx.doi.org/10.1063/1.101450.

[38] J.M. Gorham, W.A. Osborn, J.W. Woodcock, K.C.K. Scott, J.M. Heddleston, A.R. Hight, J.W. Gilman, Detecting carbon in carbon : Exploiting differential charging to obtain information on the chemical identity and spatial location of carbon nanotube aggregates in composites by imaging X-ray photoelectron spectroscopy, Carbon 96 (2016) 1–9, http://dx.doi.org/10.1016/j.carbon.2015.10.073.

[39] C.G. Pantano, J.F. Kelso, M.J. Suscavage, Surface studies of multicomponent silicate glasses: Quantitative analysis, sputtering effects and the atomic arrangement, Mater. Sci. Res. 15 (1983) 1–38, http://dx.doi.org/10.1007/978-1-4615-8339-4_1.

[40] ISO 19318:2004, Surface chemical analysis — X-ray photoelectron spectroscopy - Reporting of methods used for charge control and charge correction, URL https://www.iso.org/standard/33783.html.

[41] P.E. Larson, M.A. Kelly, Surface charge neutralization of insulating samples in x-ray photoemission spectroscopy, J. Vac. Sci. Technol. A Vacuum Surfaces Film. 16 (1998) 3483–3489, http://dx.doi.org/10.1116/1.581507.

[42] C.P. Hunt, C.T. Stoddart, M.P. Seah, The surface analysis of insulators by SIMS: Charge neutralization and stabilization of the surface potential, Surf. Interface Anal. 3 (1981) 157–160, http://dx.doi.org/10.1002/sia.740030404.

[43] J. Wolstenholme, Auger Electron Spectroscopy: Practical Application To Materials Analysis and Characterization of Surfaces, Interfaces, and Thin Films, Momentum Press, New York, 2015.

[44] L. Edwards, P. Mack, D.J. Morgan, Recent advances in dual mode charge compensation for XPS analysis, Surf. Interface Anal. 51 (2019) 925–933, http://dx.doi.org/10.1002/sia.6680.

[45] A. Pélisson-Schecker, H.J. Hug, J. Patscheider, Charge referencing issues in XPS of insulators as evidenced in the case of al-si-n thin films, Surf. Interface Anal. 44 (2012) 29–36, http://dx.doi.org/10.1002/sia.3765.

[46] S.B. DiCenzo, S.D. Berry, E.H. Hartford, Photoelectron spectroscopy of single-size Au clusters collected on a substrate, Phys. Rev. B 38 (1988) 8465–8468, http://dx.doi.org/10.1103/PhysRevB.38.8465.

[47] G.K. Wertheim, S.B. DiCenzo, S.E. Youngquist, Unit charge on supported gold clusters in photoemission final state, Phys. Rev. Lett. 51 (1983) 2310–2313, http://dx.doi.org/10.1103/PhysRevLett.51.2310.

[48] S. Kohiki, K. Oki, Problems of adventitious carbon as an energy reference, J. Electron Spectros. Relat. Phenomena 33 (1984) 375–380, http://dx.doi.org/10.1016/0368-2048(84)80032-8.

[49] S. Kohiki, Problem of evaporated gold as an energy reference in X-ray photoelectron spectroscopy, Appl. Surf. Sci. 17 (1984) 497–503, http://dx.doi.org/10.1016/0378-5963(84)90009-6.

[50] G. Greczynski, L. Hultman, X-ray Photoelectron spectroscopy: Towards reliable binding energy referencing, Prog. Mater. Sci. 107 (2020) 100591, http://dx.doi.org/10.1016/j.pmatsci.2019.100591.

[51] P.H. Citrin, D.R. Hamann, Measurement and calculation of polarization and potential-energy effects on core-electron binding energies in solids: X-ray photoemission of rare gases implanted in noble metals, Phys. Rev. B 10 (1974) 4948–4963, http://dx.doi.org/10.1103/PhysRevB.10.4948.

[52] I. Bertóti, Characterization of nitride coatings by XPS, Surf. Coatings Technol. 151–152 (2002) 194–203, http://dx.doi.org/10.1016/S0257-8972(01)01619-X.

[53] D.J. Hnatowich, J. Hudis, M.L. Perlman, R.C. Ragaini, Determination of charging effect in photoelectron spectroscopy of nonconducting solids, J. Appl. Phys. 42 (1971) 4883–4886, http://dx.doi.org/10.1063/1.1659869.

[54] G. Johansson, J. Hedman, A. Berndtsson, M. Klasson, R. Nilsson, Calibration of electron spectra, J. Electron Spectros. Relat. Phenomena 2 (1973) 295–317, http://dx.doi.org/10.1016/0368-2048(73)80022-2.

[55] T.L. Barr, S. Seal, Nature of the use of adventitious carbon as a binding energy standard, J. Vacuum Sci. Technol. A 13 (1995) 1239–1246, http://dx.doi.org/10.1116/1.579868.

[56] P. Swift, Adventitious carbon—the panacea for energy referencing? Surf. Interface Anal. 4 (1982) 47–51, http://dx.doi.org/10.1002/sia.740040204.

[57] S. Kinoshita, T. Ohta, H. Kuroda, Comments on the energy calibration in X-Ray photoelectron spectroscopy, Bull. Chem. Soc. Jpn. 49 (1976) 1149–1150, http://dx.doi.org/10.1246/bcsj.49.1149.

[58] G. Greczynski, L. Hultman, C 1s peak of adventitious carbon aligns to the vacuum level: Dire consequences for material's bonding assignment by photoelectron spectroscopy, ChemPhysChem 18 (2017) 1507–1512, http://dx.doi.org/10.1002/cphc.201700126.

[59] C.D. Wagner, Auger lines in X-Ray photoelectron spectrometry, Anal. Chem. 44 (1972) 967–973, http://dx.doi.org/10.1021/ac60314a015.

[60] S.W. Gaarenstroom, N. Winograd, Initial and final state effects in the ESCA spectra of cadmium and silver oxides, J. Chem. Phys. 67 (1977) 3500–3506, http://dx.doi.org/10.1063/1.435347.

[61] J. Castle, R. West, The utility of bremsstrahlung-induced auger peaks, J. Electron Spectros. Relat. Phenomena 16 (1979) 195–197, http://dx.doi.org/10.1016/0368-2048(79)85018-5.

[62] K. Yates, R.H. West, Monochromatized ag lα X-rays as a source for higher energy XPS, Surface and Interface Analysis 5 (1983) 133–138, http://dx.doi.org/10.1002/sia.740050402.

[63] C.D. Wagner, A. Joshi, The auger parameter, its utility and advantages: a review, J. Electron Spectros. Relat. Phenomena 47 (1988) 283–313, http://dx.doi.org/10.1016/0368-2048(88)85018-7.

[64] S. Hofmann, Practical Surface Analysis By Auger and X-Ray Photoelectron Spectroscopy, second ed., Wiley, Chichester, UK, 1990.

[65] P.J. Cumpson, Angle-resolved XPS and AES: Depth-resolution limits and a general comparison of properties of depth-profile reconstruction methods, J. Electron Spectros. Relat. Phenomena 73 (1995) 25–52, http://dx.doi.org/10.1016/0368-2048(94)02270-4.

[66] W.A. Fraser, J.V. Florio, W.N. Delgass, W.D. Robertson, An X-Ray photoelectron spectrometer designed for surface research, Rev. Sci. Instrum. 44 (1973) 1490–1496, http://dx.doi.org/10.1063/1.1685981.

[67] K.E. Smith, S.D. Kevan, The electronic structure of solids studied using angle resolved photoemission spectroscopy, Prog. Solid State Chem. 21 (1991) 49–131, http://dx.doi.org/10.1016/0079-6786(91)90001-G.

[68] M.S. Vinodh, L.P.H. Jeurgens, Quantitative analysis of angle-resolved XPS spectra recorded in parallel data acquisition mode, Surf. Interface Anal. 36 (2004) 1629–1636, http://dx.doi.org/10.1002/sia.2000.

[69] T. Richter, G. Frischat, G. Borchardt, S. Scherrer, A mathematical model of short time leaching at fracture surfaces, J. Non. Cryst. Solids 120 (1990) 117–125, http://dx.doi.org/10.1016/0022-3093(90)90197-T.

[70] G. Kojima, K. Matsumoto, O. Sakamoto, Y. Yamamoto, M. Kawamoto, Interaction of water with glass at very high temperature under dynamic condition and the properties of the obtained glass surface, J. Non. Cryst. Solids 292 (2001) 50–58, http://dx.doi.org/10.1016/S0022-3093(01)00861-4.

[71] H. Yamanaka, M. Yamashita, J. Matsuoka, H. Wakabayashi, R. Terai, Depth profiling by XPS for corroded glass, J. Non. Cryst. Solids 116 (1990) 286–288, http://dx.doi.org/10.1016/0022-3093(90)90704-P.

[72] A. Deshkovskaya, Ion beam-stimulated processes in glasses, Nucl. Instrum. Methods Phys. Res. B 166–167 (2000) 511–516, http://dx.doi.org/10.1016/S0168-583X(99)01031-9.

[73] J. Zemek, P. Jiricek, J. Houdkova, K. Jurek, O. Gedeon, Lead-silicate glass surface sputtered by an argon cluster ion beam investigated by XPS, J. Non. Cryst. Solids 469 (2017) 1–6, http://dx.doi.org/10.1016/j.jnoncrysol.2017.04.001.

[74] B.M. Smets, T.P. Lommen, Ion beam effects on glass surfaces, J. Am. Ceram. Soc. 65 (1982) c80–c81, http://dx.doi.org/10.1111/j.1151-2916.1982.tb10453.x.

[75] R.K. Brow, Glass surface modifications during ion beam sputtering, J. Non. Cryst. Solids 107 (1) (1988) 1–10, http://dx.doi.org/10.1016/0022-3093(88)90084-1.

[76] Y. Yamamoto, K. Yamamoto, Ar ion damage on the surface of soda-lime-silica glass, IOP Conf. Ser. Mater. Sci. Eng. 18 (2011) 16–20, http://dx.doi.org/10.1088/1757-899X/18/2/022005.

[77] I. Yamada, A short review of ionized cluster beam technology, Nucl. Inst. Methods Phys. Res. B. 99 (1995) 240–243, http://dx.doi.org/10.1016/0168-583X(94)00562-1.

[78] I. Yamada, Historical milestones and future prospects of cluster ion beam technology, Appl. Surf. Sci. 310 (2014) 77–88, http://dx.doi.org/10.1016/j.apsusc.2014.03.147.

[79] V.N. Popok, I. Barke, E.E. Campbell, K.-H. Meiwes-Broer, Cluster–surface interaction: From soft landing to implantation, Surf. Sci. Rep. 66 (2011) 347–377, http://dx.doi.org/10.1016/j.surfrep.2011.05.002.

[80] I. Yamada, J. Matsuo, N. Toyoda, T. Aoki, T. Seki, Progress and applications of cluster ion beam technology, Curr. Opin. Solid State Mater. Sci. 19 (2015) 12–18, http://dx.doi.org/10.1016/j.cossms.2014.11.002.

[81] V.N. Popok, Cluster ion implantation ingraphite and diamond: Radiation damage and stopping of cluster constituents, Rev. Adv. Mater. Sci. 38 (2014) 7–16, http://dx.doi.org/10.1016/j.surfrep.2011.05.002.

[82] T. Aoki, Molecular dynamics simulations of cluster impacts on solid targets: implantation, surface modification, and sputtering, J. Comput. Electron. 13 (2014) 108–121, http://dx.doi.org/10.1007/s10825-013-0504-5.

[83] J. Zemek, P. Jiricek, J. Houdkova, A. Artemenko, M. Jelinek, Diamond-like carbon and nanocrystalline diamond film surfaces sputtered by argon cluster ion beams, Diam. Relat. Mater. 68 (2016) 37–41, http://dx.doi.org/10.1016/j.diamond.2016.06.003.

[84] N.G. Korobeishchikov, I.V. Nikolaev, M.A. Roenko, V.V. Atuchin, Precise sputtering of silicon dioxide by argon cluster ion beams, Appl. Phys. A Mater. Sci. Process. 124 (2018) 1–6, http://dx.doi.org/10.1007/s00339-018-2256-3.

[85] M.P. Seah, Universal equation for argon gas cluster sputtering yields, J. Phys. Chem. C. 117 (2013) 12622–12632, http://dx.doi.org/10.1021/jp402684c.

[86] M.P. Seah, S.J. Spencer, A.G. Shard, Angle dependence of argon gas cluster sputtering yields for organic materials, J. Phys. Chem. B. 119 (2015) 3297–3303, http://dx.doi.org/10.1021/jp512379k.

[87] K.N. Dalby, H.W. Nesbitt, V.P. Zakaznova-Herzog, P.L. King, Resolution of bridging oxygen signals from o 1s spectra of silicate glasses using XPS: Implications for o and si speciation, Geochim. Cosmochim. Acta. 71 (2007) 4297–4313, http://dx.doi.org/10.1016/j.gca.2007.07.005.

[88] L.-S. Chang, Y.-C. Lin, C.-Y. Su, H.-C. Wu, J.-P. Pan, Effect of C60 ion sputtering on the compositional depth profiling in XPS for Li(Ni,Co,Mn)O2 electrodes, Appl. Surf. Sci. 258 (2011) 1279–1281, http://dx.doi.org/10.1016/j.apsusc.2011.08.087.

[89] Y. Yamamoto, K. Yamamoto, Precise XPS depth profile of soda-lime-silica glass using C60 ion beam, J. Non. Cryst. Solids 356 (2010) 14–18, http://dx.doi.org/10.1016/j.jnoncrysol.2009.09.027.

[90] Y. Yamamoto, K. Yamamoto, Precise XPS depth profile of soda-lime-silica float glass using C 60 ion beam, Opt. Mater. (Amst). 33 (2011) 1927–1930, http://dx.doi.org/10.1016/j.optmat.2011.03.026.

[91] H. Nesbitt, G. Bancroft, R. Davidson, N. Mcintyre, A. Pratt, Minimum XPS core-level line widths of insulators, including silicate minerals, Am. Mineral. 89 (2004) 878–882, http://dx.doi.org/10.2138/am-2004-5-623.

[92] A.K. Varshneya, J.C. Mauro, Fundamentals of Inorganic Glasses, 3rd Ed., Elsevier, 2019, http://dx.doi.org/10.1016/C2017-0-04281-7.

[93] Y. Yun, P. Bray, Nuclear magnetic resonance studies of the glasses in the system Na_2O-B_2O_3-SiO_2, J. Non. Cryst. Solids 27 (1978) 363–380, http://dx.doi.org/10.1016/0022-3093(78)90020-0.

[94] P. Bray, Structural models for borate glasses, J. Non. Cryst. Solids 75 (1985) 29–36, http://dx.doi.org/10.1016/0022-3093(85)90198-X.

[95] W.J. Dell, P.J. Bray, S.Z. Xiao, ^{11}B NMR studies and structural modeling of Na_2O-B_2O_3-SiO_2 glasses of high soda content, J. Non. Cryst. Solids 58 (1983) 1–16, http://dx.doi.org/10.1016/0022-3093(83)90097-2.

[96] J. Zhong, X. Wu, M. Liu, P. Bray, Structural modeling of lithium borosilicate glasses via NMR studies, J. Non. Cryst. Solids 107 (1988) 81–87, http://dx.doi.org/10.1016/0022-3093(88)90096-8.

[97] R. Martens, W. Müller-Warmuth, Structural groups and their mixing in borosilicate glasses of various compositions – an NMR study, J. Non. Cryst. Solids 265 (2000) 167–175, http://dx.doi.org/10.1016/S0022-3093(99)00693-6.

[98] Y. Yun, S. Feller, P. Bray, Correction and addendum to "nuclear magnetic resonance studies of the glasses in the system Na_2O-B_2O_3-SiO_2", J. Non. Cryst. Solids 33 (1979) 273–277, http://dx.doi.org/10.1016/0022-3093(79)90055-3.

[99] D. Manara, A. Grandjean, D.R. Neuville, Structure of borosilicate glasses and melts: A revision of the yun, bray and dell model, J. Non. Cryst. Solids 355 (2009) 2528–2531, http://dx.doi.org/10.1016/j.jnoncrysol.2009.08.033.

[100] P. Mazzoldi, Ion beam modification of glass surface properties, J. Non-Cryst. Solids 120 (1990) 223–233, http://dx.doi.org/10.1016/0022-3093(90)90206-2.

[101] H. Hosono, Simple criterion on colloid formation in SiO_2 glasses by ion implantation, Japan. J. Appl. Phys. 32 (1993) 3892–3894, http://dx.doi.org/10.1143/jjap.32.3892.

[102] H. Hosono, N. Matsunami, Structural defects and chemical interaction of implanted ions with substrate structure in amorphous SiO_2, Phys. Rev. B 48 (1993) 13469–13473, http://dx.doi.org/10.1103/PhysRevB.48.13469.

[103] P. Mazzoldi, G.W. Arnold, G. Battaglin, R. Bertoncello, F. Gonella, Peculiarities and application perspectives of metal-ion implants in glasses, Nucl. Instrum. Meth. B 91 (1994) 478–492, http://dx.doi.org/10.1016/0168-583x(94)96273-1.

[104] G.W. Arnold, Ion implantation in silicate glasses, J. Non-Cryst. Solids 179 179 (1994) 288–299, http://dx.doi.org/10.1016/0168-583x(94)96273-1.

[105] H. Hosono, H. Imagawa, Ion-solid chemistry in implanted amorphous SiO_2, Nucl. Instr. and Meth. B 91 (1994) 510–514, http://dx.doi.org/10.1016/0168-583x(94)96276-6.

[106] E. Cattaruzza, Quantum-dot composite silicate glasses obtained by ion implantation, Nucl. Instr. and Meth. B 169 (2000) 141–155, http://dx.doi.org/10.1016/s0168-583x(00)00031-8.

[107] V. Bandourko, N. Umeda, T. Suga, C.G. Lee, K. Kono, Y. Takeda, N. Kishimoto, Nanoparticles formation in insulators induced by Au^- and Au_2^- ion implantation, Nucl. Instr. and Meth. B 206 (2003) 606–609, http://dx.doi.org/10.1016/s0168-583x(00)00031-8.

[108] R. Kelly, Bombardment-induced compositional change with alloys, oxides, oxysalts and halides III. The role of chemical driving forces, Mater. Sci. Eng. A 115 (1989) 11–24, http://dx.doi.org/10.1016/0921-5093(89)90650-3.

[109] E. Cattaruzza, G. Mattei, P. Mazzoldi, R. Bertoncello, G. Battaglin, L. Mirenghi, Formation of amorphous silicide nanoclusters in chromium- and titanium-implanted silica, Appl. Phys. Lett. 67 (1995) 2884–2886, http://dx.doi.org/10.1063/1.114817.

[110] A. Carnera, P. Mazzoldi, A. Boscolo-Boscoletto, F. Caccavale, R. Bertoncello, G. Granozzi, I. Spagnol, G. Battaglin, On the formation of silicon oxynitride by ion implantation in fused silica, J. Non-Cryst. Solids 125 (1990) 293—301, http://dx.doi.org/10.1016/0022-3093(90)90861-f.

[111] J.F. Stebbins, Identification of multiple structural species in silicate glasses by 29si NMR, Nature 330 (1987) 465–467, http://dx.doi.org/10.1038/330465a0.

[112] P. Zhang, P.J. Grandinetti, J.F. Stebbins, Anionic species determination in CaSiO3 glass using two-dimensional 29Si NMR, J. Phys. Chem. B. 101 (1997) 4004–4008, http://dx.doi.org/10.1021/jp9700342.

[113] F. Herzog, V.P. Zakaznova-Herzog, Quantitative Raman spectroscopy: Challenges, shortfalls, and solutions–application to calcium silicate glasses, Am. Mineral. 96 (2011) 914–927, http://dx.doi.org/10.2138/am.2011.3508.

[114] H. Maekawa, T. Maekawa, K. Kawamura, T. Yokokawa, The structural groups of alkali silicate glasses determined from 29Si MAS-NMR, J. Non. Cryst. Solids 127 (1991) 53–64, http://dx.doi.org/10.1016/0022-3093(91)90400-Z.

[115] W.J. Malfait, W.E. Halter, Y. Morizet, B.H. Meier, R. Verel, Structural control on bulk melt properties: Single and double quantum 29Si NMR spectroscopy on alkali-silicate glasses, Geochim. Cosmochim. Acta. 71 (2007) 6002–6018, http://dx.doi.org/10.1016/j.gca.2007.09.011.

[116] M.F. Hochella, Chapter 13. Auger electron and X-ray photoelectron spectroscopies, in: F.C. Hawthorne (Ed.), Spectroscopic Methods in Mineralogy and Geology, De Gruyter, Berlin, Boston, 1988, pp. 573–638, http://dx.doi.org/10.1515/9781501508974-015.

[117] R. Brückner, H.U. Chun, H. Goretzki, XPS-Measurements on alkali silicate and soda aluminosilicate glasses, Japan. J. Appl. Phys. 17 (1978) 291–294, http://dx.doi.org/10.7567/JJAPS.17S2.291.

[118] R. Brückner, H.-U. Chun, H. Goretzki, M. Sammet, XPS Measurements and structural aspects of silicate and phosphate glasses, J. Non. Cryst. Solids 42 (1980) 49–60, http://dx.doi.org/10.1016/0022-3093(80)90007-1.

[119] B. Veal, D. Lam, A. Paulikas, W. Ching, XPS Study of CaO in sodium silicate glass, J. Non. Cryst. Solids 49 (1982) 309–320, http://dx.doi.org/10.1016/0022-3093(82)90127-2.

[120] J. Jen, M. Kalinowski, An ESCA study of the bridging to non-bridging oxygen ratio in sodium silicate glass and the correlations to glass density and refractive index, J. Non. Cryst. Solids 38–39 (1980) 21–26, http://dx.doi.org/10.1016/0022-3093(80)90388-9.

[121] S. Matsumoto, T. Nanba, Y. Miura, X-RAy photoelectron spectroscopy of alkali silicate glasses, J. Ceram. Soc. Japan 106 (1998) 415–421, http://dx.doi.org/10.2109/jcersj.106.415.

[122] A. Sharma, H. Jain, A.C. Miller, Surface modification of a silicate glass during XPS experiments, Surf. Interface Anal. 31 (2001) 369–374, http://dx.doi.org/10.1002/sia.983.

[123] H.W. Nesbitt, G.M. Bancroft, G.S. Henderson, R. Ho, K.N. Dalby, Y. Huang, Z. Yan, Bridging, non-bridging and free (O^{2-}) oxygen in Na_2O-SiO_2 glasses: An X-ray photoelectron spectroscopic (XPS) and nuclear magnetic resonance (NMR) study, J. Non. Cryst. Solids 357 (2011) 170–180, http://dx.doi.org/10.1016/j.jnoncrysol.2010.09.031.

[124] R. Sawyer, H.W. Nesbitt, R.A. Secco, High resolution X-ray photoelectron spectroscopy (XPS) study of K_2O-SiO_2 glasses: Evidence for three types of O and at least two types of si, J. Non. Cryst. Solids 358 (2012) 290–302, http://dx.doi.org/10.1016/j.jnoncrysol.2011.09.027.

[125] D. Sprenger, H. Bach, W. Meisel, P. Gütlich, Discrete bond model (DBM) of sodium silicate glasses derived from XPS, Raman and NMR measurements, J. Non. Cryst. Solids 159 (1993) 187–203, http://dx.doi.org/10.1016/0022-3093(93)90223-K.

[126] S. Sen, R. Youngman, NMR Study of Q-speciation and connectivity in K2O–SiO2 glasses with high silica content, J. Non-Crystalline Solids 331 (2003) 100–107, http://dx.doi.org/10.1016/j.jnoncrysol.2003.08.071.

[127] W.Y. Ching, R.A. Murray, D.J. Lam, B.W. Veal, Comparative studies of electronic structures of sodium metasilicate and α and β phases of sodium disilicate, Phys. Rev. B 28 (1983) 4724–4735, http://dx.doi.org/10.1103/PhysRevB.28.4724.

[128] W.Y. Ching, Y.P. Li, B.W. Veal, D.J. Lam, Electronic structures of lithium metasilicate and lithium disilicate, Phys. Rev. B 32 (1985) 1203–1207, http://dx.doi.org/10.1103/PhysRevB.32.1203.

[129] A.K. Pant, D.W.J. Cruickshank, The crystal structure of α-$Na_2Si_2O_5$, Acta Crystallogr. Sect. B 24 (1968) 13–19, http://dx.doi.org/10.1107/S0567740868001640.

[130] H. Nesbitt, G. Henderson, G. Bancroft, R. Ho, Experimental evidence for Na coordination to bridging oxygen in na-silicate glasses: Implications for spectroscopic studies and for the modified random network model, J. Non. Cryst. Solids 409 (2015) 139–148, http://dx.doi.org/10.1016/j.jnoncrysol.2014.11.024.

[131] T. Schaller, J.F. Stebbins, M.C. Wilding, Cation clustering and formation of free oxide ions in sodium and potassium lanthanum silicate glasses: Nuclear magnetic resonance and Raman spectroscopic findings, J. Non. Cryst. Solids 243 (1999) 146–157, http://dx.doi.org/10.1016/S0022-3093(98)00838-2.

[132] P.W. Wang, L.P. Zhang, L. Lu, D.V. LeMone, D.L. Kinser, Surface modification of lead silicate glass under X-ray irradiation, Appl. Surf. Sci. 84 (1995) 75–83, http://dx.doi.org/10.1016/0169-4332(94)00359-9.

[133] D.R. Baer, M.H. Engelhard, A.S. Lea, Introduction to surface science spectra data on electron and x-ray damage: Sample degradation during XPS and AES measurements, Surf. Sci. Spectra 10 (2003) 47–56, http://dx.doi.org/10.1116/11.20040199.

[134] O. Puglisi, G. Marletta, A. Torrisi, Oxygen depletion in electron beam bombarded glass surfaces studied by XPS, J. Non. Cryst. Solids 55 (1983) 433–442, http://dx.doi.org/10.1016/0022-3093(83)90047-9.

[135] O. Puglisi, G. Marletta, A. Torrisi, Radiation-enhanced diffusion of Na in alkaline glasses, J. Non-Crystalline Solids 83 (1986) 344–352, http://dx.doi.org/10.1016/0022-3093(86)90247-4.

[136] J. Akutagawa, D. Yamamoto, W. Pong, Soft x-ray induced darkening of glass surfaces, J. Electron Spectros. Relat. Phenomena 82 (1996) 75–77, http://dx.doi.org/10.1016/s0368-2048(96)03050-2.

[137] W.L. Konijnendijk, J.M. Stevels, The structure of borosilicate glasses studied by Raman scattering, J. Non. Cryst. Solids 20 (1976) 193–224, http://dx.doi.org/10.1016/0022-3093(76)90132-0.

[138] C. Hsieh, H. Jain, A. Miller, E. Kamitsos, X-ray Photoelectron spectroscopy of Al- and B-substituted sodium trisilicate glasses, J. Non. Cryst. Solids 168 (1994) 247–257, http://dx.doi.org/10.1016/0022-3093(94)90336-0.

[139] Y. Miura, H. Kusano, T. Nanba, S. Matsumoto, X-ray Photoelectron spectroscopy of sodium borosilicate glasses, J. Non. Cryst. Solids 290 (2001) 1–14, http://dx.doi.org/10.1016/S0022-3093(01)00720-7.

[140] T. Nanba, Y. Miura, Alkali distribution in borosilicate glasses, Phys. Chem. Glasses 44 (2003) 244–248.

[141] D. Sprenger, H. Bach, W. Meisel, P. Gütlich, XPS Study of leached glass surfaces, J. Non. Cryst. Solids 126 (1990) 111–129, http://dx.doi.org/10.1016/0022-3093(90)91029-Q.

[142] S.W. Knipe, J.R. Mycroft, A.R. Pratt, H.W. Nesbitt, G.M. Bancroff, X-ray Photoelectron spectroscopic study of water adsorption on iron sulphide minerals, Geochim. Cosmochim. Acta 59 (1995) 1079–1090, http://dx.doi.org/10.1016/0016-7037(95)00025-U.

[143] B. Bunker, Molecular mechanisms for corrosion of silica and silicate glasses, J. Non. Cryst. Solids 179 (1994) 300–308, http://dx.doi.org/10.1016/0022-3093(94)90708-0.

[144] B. Grambow, R. Müller, First-order dissolution rate law and the role of surface layers in glass performance assessment, J. Nucl. Mater. 298 (2001) 112–124, http://dx.doi.org/10.1016/S0022-3115(01)00619-5.

[145] C. Cailleteau, F. Angeli, F. Devreux, S. Gin, J. Jestin, P. Jollivet, O. Spalla, Insight into silicate-glass corrosion mechanisms, Nature Mater. 7 (2008) 978–983, http://dx.doi.org/10.1038/nmat2301.

[146] T. Hiemstra, W. van Riemsdijk, Multiple activated complex dissolution of metal (hydr) oxides: A thermodynamic approach applied to quartz, J. Colloid Interface Sci. 136 (1990) 132–150, http://dx.doi.org/10.1016/0021-9797(90)90084-2.

[147] T.A. Michalske, B. Bunker, The fracturing of glass, Sci. Am. 257 (1987) 122–129.

[148] M. Nogami, M. Tomozawa, Effect of stress on water diffusion in silica glass, J. Am. Ceram. Soc. 67 (1984) 151–154, http://dx.doi.org/10.1111/j.1151-2916.1984.tb09634.x.

[149] N.P. Bansal, R.H. Doremus, Handbook of Glass Properties, Orlando, 1986.

[150] R.H. Doremus, Y. Mehrotra, W.A. Lanford, C. Burman, Reaction of water with glass: influence of a transformed surface layer, J. Mater. Sci. 18 (1983) 612–622, http://dx.doi.org/10.1007/BF00560651.

[151] R.W. Douglas, T.M.M. El-Shamy, Reactions of glasses with aqueous solutions, J. Am. Ceram. Soc. 50 (1967) 1–8, http://dx.doi.org/10.1111/j.1151-2916.1967.tb14960.x.

[152] J.O. Isard, The mixed alkali effect in glasses, J. Non. Cryst. Solids 1 (1969) 235–261, http://dx.doi.org/10.1111/j.1151-2916.1965.tb14784.x.

[153] T. Wassick, R. Doremus, W. Lanford, C. Burman, Hydration of soda-lime silicate glass, effect of alumina, J. Non. Cryst. Solids 54 (1983) 139–151, http://dx.doi.org/10.1016/0022-3093(83)90088-1.

[154] B.C. Bunker, G.W. Arnold, D.E. Day, P.J. Bray, The effect of molecular structure on borosilicate glass leaching, J. Non. Cryst. Solids 87 (1986) 226–253, http://dx.doi.org/10.1016/S0022-3093(86)80080-1.

[155] B.C. Bunker, T.J. Headley, S.C. Douglas, Gel structures in leached alkali silicate glass, MRS Proc. 32 (1984) 41, http://dx.doi.org/10.1557/PROC-32-41.

[156] D.E. Clark, C.G. Pantano, L. Hench, Corrosion of Glass, New York, 1979.

[157] E. Guadagnino, D. Zuccato, Delamination propensity of pharmaceutical glass containers by accelerated testing with different extraction media, PDA J. Pharm. Sci. Technol. 66 (2012) 116–125, http://dx.doi.org/10.5731/pdajpst.2012.00853.

[158] R.A. Schaut, W.P. Weeks, Historical review of glasses used for parenteral packaging, PDA J. Pharm. Sci. Technol. 71 (2017) 279–296, http://dx.doi.org/10.5731/pdajpst.2016.007377.

[159] V. Rupertus, B. Hladik, U. Rothhaar, V. Scheumann, A quick test to monitor the delamination propensity of glass containers, PDA J. Pharm. Sci. Technol. 68 (2014) 373–380, http://dx.doi.org/10.5731/pdajpst.2014.00990.

[160] J. Cerdan-Diaz, K. Choju, C.R. Flynn, L. Gavioli, R. Iacocca, A. Meysner, J. Pfeifer, H. Roehl, V. Rupertus, M. Scarpa, H. Sun, J. Zhang, D. Zuccato, M. Guglielmi, Delamination propensity of glass containers for pharmaceutical use: A round robin activity looking for a predictive test, PDA J. Pharm. Sci. Technol. 72 (2018) 553–565, http://dx.doi.org/10.5731/pdajpst.2018.008599.

[161] R.G. Iacocca, N. Toltl, M. Allgeier, B. Bustard, X. Dong, M. Foubert, J. Hofer, S. Peoples, T. Shelbourn, Factors affecting the chemical durability of glass used in the pharmaceutical industry, AAPS Pharm. Sci. Tech. 11 (2010) 1340–1349, http://dx.doi.org/10.1208/s12249-010-9506-9.

[162] D. Sprenger, H. Bach, W. Meisel, P. Gütlich, Quantitative XPS analysis of leached layers on optical glasses, Surf. Interface Anal. 20 (1993) 796–802, http://dx.doi.org/10.1002/sia.740200908.

[163] J. Banerjee, S.H. Kim, C.G. Pantano, Elemental areal density calculation and oxygen speciation for flat glass surfaces using x-ray photoelectron spectroscopy, J. Non. Cryst. Solids 450 (2016) 185–193, http://dx.doi.org/10.1016/j.jnoncrysol.2016.07.029.

[164] J. Banerjee, V. Bojan, C.G. Pantano, S.H. Kim, Effect of heat treatment on the surface chemical structure of glass: Oxygen speciation from in situ XPS analysis, J. Am. Ceram. Soc. 101 (2018) 644–656, http://dx.doi.org/10.1111/jace.15245.

[165] G. Young, Interaction of water vapor with silica surfaces, J. Colloid Sci. 13 (1958) 67–85, http://dx.doi.org/10.1016/0095-8522(58)90010-2.

[166] A.S. D'Souza, C.G. Pantano, Hydroxylation and dehydroxylation behavior of silica glass fracture surfaces, J. Am. Ceram. Soc. 85 (2002) 1499–1504, http://dx.doi.org/10.1111/j.1151-2916.2002.tb00303.x.

[167] M.L. Hair, Hydroxyl groups on silica surface, J. Non. Cryst. Solids 19 (1975) 299–309, http://dx.doi.org/10.1016/0022-3093(75)90095-2.

[168] A. Tilocca, Sodium migration pathways in multicomponent silicate glasses: Car-parrinello molecular dynamics simulations, J. Chem. Phys. 133 (2010) 014701, http://dx.doi.org/10.1063/1.3456712.

[169] M. Rarivomanantsoa, P. Jund, R. Jullien, Sodium diffusion through amorphous silica surfaces: A molecular dynamics study, J. Chem. Phys. 120 (2004) 4915–4920, http://dx.doi.org/10.1063/1.1645511.

[170] E.L. Mochel, M.E. Nordberg, T.H. Elmer, Strengthening of glass surfaces by sulfur trioxide treatment, J. Am. Ceram. Soc. 49 (1966) 585–589, http://dx.doi.org/10.1111/j.1151-2916.1966.tb13173.x.

[171] B.C. Bunker, T.A. Michalske, Effect of surface corrosion on glass fracture, in: Fracture Mechanics of Ceramics, Springer US, Boston, MA, 1986, pp. 391–411, http://dx.doi.org/10.1007/978-1-4615-7026-4_30.

[172] S. Takeda, K. Yamamoto, Y. Hayasaka, K. Matsumoto, Surface OH group governing wettability of commercial glasses, J. Non. Cryst. Solids 249 (1999) 41–46, http://dx.doi.org/10.1016/S0022-3093(99)00297-5.

[173] S. Reiß, S. Krischok, E. Rädlein, Comparative study of weather induced corrosion mechanisms of toughened and normal float glasses, Glas. Technol. Eur. J. Glas. Sci. Technol. Part A 60 (2019) 33–44, http://dx.doi.org/10.13036/17533546.60.2.020.

[174] S. Reiß, R. Grieseler, S. Krischok, E. Rädlein, The influence of sahara sand on the degradation behavior of float glass surfaces, J. Non. Cryst. Solids 479 (2018) 16–28, http://dx.doi.org/10.1016/j.jnoncrysol.2017.09.055.

[175] T. Palomar, P. Redol, I. Cruz Almeida, E. Pereira da Silva, M. Vilarigues, The influence of environment in the alteration of the stained-glass windows in portuguese monuments, Heritage 1 (2018) 365–376, http://dx.doi.org/10.3390/heritage1020025.